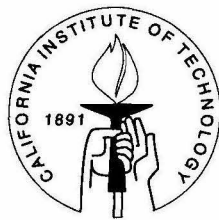


# Three-Dimensional Cohesive Modeling of Impact Damage of Composites

Thesis by  
Chengxiang Yu

In Partial Fulfillment of the Requirements  
for the Degree of  
Doctor of Philosophy



California Institute of Technology  
Pasadena, California

2001  
(Submitted May 22, 2001)

# Acknowledgements

My heartfelt acknowledgements and admiration for my advisor, Professor Michael Ortiz for his brilliancy and unique personality that guides me both academically and personally. His patience and constant enthusiasm, his belief and encouragement for his students always impress me and exert an uplifting influence upon me. Also, I am indebted to Professor Ares Rosakis for his patience, kindness for all the questions I had. My deep gratitude goes to Anna Pandolfi, a dear friend and a real mentor for several years. I also would like to thank Professor Yizhao Thomas Hou and Professor James L. Beck for reviewing my thesis. I am grateful for the financial support provided by the US Army Research Office under grant DAAH04-96-1-0056, and by the US Department of Energy through Caltech's Asci/ASAP Center for the Simulation of the Dynamic Behavior of Materials. I gratefully acknowledge Michael Falk for the cooperative exchange of the dynamic branching results, and Alan Needleman for valuable discussions on this subject.

I would like to thank all my colleagues in the Computational Mechanics laboratory for sharing these unforgettable years with me, to Demir Coker, for generously sharing his experimental expertise.

Finally, I would have never achieved anything without the deep love and unconditional support of my parents, my brothers and sister as well as my lovable nephews and nieces who always invigorate me throughout the time. And my whole heart to my new faith that puts everything in place and my dear friend Gonzalo Ruiz who has led me on this way and reshaped my life.

*For my beloved parents.*

# Abstract

The objective of this work is to establish the applicability of cohesive theories of fracture in situations involving material interface, material heterogeneity (e.g., layered composites), material anisotropy (e.g., fiber-reinforced composites), shear cracks, intersonic dynamic crack growth and dynamic crack branching. The widely used cohesive model is extended to orthotropic range. The so-developed computational tool, completed by a self-adaptive fracture procedure and a frictional contact algorithm, is capable of following the evolution of three-dimensional damage processes, modeling the progressive decohesion of interfaces and anisotropic materials. The material parameters required by cohesive laws are directly obtained from static experiments. The ability of the methodology to simulate diverse problems such as delamination between fibers of graphite/epoxy composites, as well as sandwich structures and branching within brittle bulk materials has been demonstrated.

# Contents

<b>Acknowledgements</b>	<b>i</b>
<b>Abstract</b>	<b>iii</b>
<b>1 Introduction</b>	<b>1</b>
1.1 Dynamic fracture mechanics . . . . .	1
1.2 Interfacial fracture mechanics . . . . .	3
1.3 Interfacial fracture criterion . . . . .	5
1.4 Numerical trends . . . . .	8
<b>2 Finite-element methodology</b>	<b>12</b>
2.1 Introduction . . . . .	12
2.2 Field and constitutive equations . . . . .	12
2.3 Finite element model . . . . .	14
2.4 Cohesive formulation . . . . .	16
2.5 Transversely isotropic cohesive law . . . . .	21
2.6 Small strain friction/contact algorithm . . . . .	22
2.7 Thermal effects . . . . .	27
2.8 Fragmentation algorithm . . . . .	27
<b>3 Intersonic Crack Growth in Asymmetrically Loaded Unidirectional Composite Plates</b>	<b>29</b>
3.1 Introduction . . . . .	29
3.2 Material properties and experimental set-up . . . . .	31
3.3 Numerical results . . . . .	38
3.4 Parametric studies . . . . .	43
3.5 Summary . . . . .	45

<b>4</b>	<b>Failure mode selection of sandwich structures</b>	<b>54</b>
4.1	Introduction . . . . .	54
4.2	Experimental set up . . . . .	55
4.3	Numerical simulations . . . . .	61
4.3.1	Mesh description . . . . .	61
4.3.2	Results and discussion . . . . .	63
4.4	Parametric studies . . . . .	68
4.5	Summary . . . . .	72
<b>5</b>	<b>Dynamic crack branching</b>	<b>73</b>
5.1	Introduction . . . . .	73
5.2	Model Description . . . . .	77
5.3	Results and Discussion . . . . .	80
<b>6</b>	<b>Conclusions and future work</b>	<b>94</b>
<b>A</b>	<b>Interpolation in 3D tetrahedra - field interpolation</b>	<b>96</b>
	<b>Bibliography</b>	<b>101</b>

# List of Figures

1.1	Geometry and conventions for an interface crack. . . . .	7
2.1	Linear loading and unloading behavior. . . . .	19
2.2	Geometry of a 3D cohesive element. The surfaces $S^+$ and $S^-$ coincide in the reference configuration of the solid [92]. . . . .	19
2.3	Cohesive surface traversing a 3D body. . . . .	20
2.4	Assembly of 12-node triangular cohesive element and two 10-node tetrahedral elements. . . . .	21
2.5	Transversely isotropic cohesive law: (a)a cohesive surface CS, the normal $N$ is inclined to the fiber direction at angle $\alpha$ ; (b)the cohesive strength for surface CS. . . . .	22
2.6	Frictional contact model: (a) decomposition of the jump $\delta$ as sum of the elastic normal displacement $\delta^e$ (negative) and irreversible tangential displacement $\delta^p$ ; (b) contact law for the direction $i$ , in the penetration case. . . . .	23
3.1	Single edge notch (SEN) specimen geometry and size for shear dominated dynamic fracture experiments. . . . .	31
3.2	Crosssection of fiber-reinforced unidirectional graphite/epoxy composite.	32
3.3	Schematic of the experimental set-up and optical technique of coherent gradient sensing (CGS). . . . .	36
3.4	A selected sequence of CGS interferograms for an intersonically propagating crack tip at time 2.8, 4.2, 5.6, 6.9, 8.3, 9.7 $\mu s$ . The field of view is a 50 mm diameter circle around the notch tip. . . . .	37
3.5	High-speed infrared images of hot spot formation due to contact behind an intersonically moving shear crack. . . . .	38

3.6	Computational model: (a) Impact velocity versus time; (b) 3-D mesh: $\bar{h}_{min} = 1$ mm, 44,593 nodes and 24,685 elements. . . . .	39
3.7	Alternative meshes: (a) mesh C1: $h_{min} = 3$ mm, 3,356 nodes, 1,573 elements; (b) mesh C2, $h_{min} = 1.43$ mm, 5,465 nodes, 2,666 elements.	40
3.8	Crack position and speed history computed from mesh with different mesh sizes, comparison with experimental data. . . . .	42
3.9	Contour levels of $\sigma_{22}$ at times: (a) 10.8; (b) 14.4; (c) 18.6; (d) 22.2 $\mu s$ .	46
3.10	Comparison between the experimental and the numerical shock wave structure. The color scale in the numerical contour plot refers to the legend in Fig. 3.9. . . . .	47
3.11	Contour levels of damage variable at time 9.6, 12, 13.2, 15.6, 18.6 and 22.2 $\mu s$ . . . . .	48
3.12	Comparison of experimental and numerical temperature values at time 40, 50, 60 and 70 $\mu s$ . See Fig. 3.13 for the temperature scale. . . . .	49
3.13	Temperature distribution across the crack surface at time 40, 50, 60 and 70 $\mu s$ . . . . .	49
3.14	Crack speed history as a function of (a) time and location (b) at dif- ferent impulse duration, the impact speed is 50 m/s. . . . .	50
3.15	Crack speed history as a function of (a) time and (b) location at differ- ent relative cohesive strength $R_s = \sigma_c / \sigma_{c0}$ , where $R_s=1$ is correspond- ing to real experimental data $\sigma_{c0} = 35.8$ MPa; impact speed $v = 30$ m/s; impulse duration = 31 $\mu s$ . . . . .	51
3.16	Crack tip position (a) and crack speed history (b) at different impact speeds; cohesive strength: $\sigma_c = 35.8$ MPa; impulse time = 31 $\mu s$ . . .	52
3.17	Minimum impact speed for the crack speed to achieve $v_c$ at different impulse duration at the same cohesive strength: $\sigma_c = 35.8$ MPa. . . .	53
4.1	Geometry for: (a) Specimen A; (b) Specimen B. . . . .	56
4.2	Schematic of the dynamic photo elasticity setup (Xu and Rosakis). . .	58

4.3	Computational mesh for specimen A, comprising 65365 nodes and 32482 10-node tetrahedra: (a) Upper view; (b) Side view. . . . .	59
4.4	Computational mesh for specimen B, comprising 113454 nodes and 56292 10-node tetrahedra: (a) Upper view; (b) Orthographic view. . .	60
4.5	Impact velocity profile with respect to time (a) and position (b) rising time and stepping down time $t_r$ and $t_d$ are 1.8 $\mu\text{s}$ ; the impulse time $t_p$ is 18.3 $\mu\text{s}$ . . . . .	61
4.6	Crack tip position (a) and crack speed (b) history of the lower interface. Comparison between experimental and numerical results. . . . .	62
4.7	Specimen A, time 55 $\mu\text{s}$ after the impact: (a) Damage pattern; (b) $\sigma_{12}$ and $\sigma_{22}$ stress components distribution. . . . .	64
4.8	Specimen B: branch pattern of the core material (Homalite-100) at (a) 60; and (b) 100 $\mu\text{s}$ after impact. . . . .	65
4.9	Specimen A: (a) the observing window and the experimental fringes at time 12.5 $\mu\text{s}$ after impact.(b) and (d) are contour levels of $\tau_{max}$ at times 41.7, 79.2 $\mu\text{s}$ ; (c) and (e) are experimental fringes at time 41.7 and 79.2 $\mu\text{s}$ . . . . .	67
4.10	Crack patterns at 300 $\mu\text{s}$ after impact, impact speed 32 m/s, for different contact area: (a) 15 mm <sup>2</sup> ; (b) 90 mm <sup>2</sup> . . . . .	69
4.11	Crack patterns for different Homalite fracture energy $G_c$ : (a) 359 N/m; (b) 176 N/m; (c) 88 N/m (impact speed 32 m/s, contact area 57 mm <sup>2</sup> , 300 $\mu\text{s}$ after impact). . . . .	70
4.12	Crack patterns for different cohesive weight coefficients of the interface (a) $\beta=10$ ; (b) $\beta=2.5$ ; (c) $\beta=0.32$ . (impact speed 32 m/s, contact area 57 mm <sup>2</sup> , 300 $\mu\text{s}$ after impact, $G_c = 88$ N/m) . . . . .	71
5.1	Geometry of the plate and initial velocity field $v_{y0}$ in $y$ direction. . . .	78
5.2	Computational mesh F, comprising 36769 nodes and 18162 10-nodes tetrahedra, minimum mesh size 20 $\mu\text{m}$ : (a) Upper view; (b) lateral view.	79
5.3	PMMA specimen at loading rate 500 $\text{s}^{-1}$ : single crack propagation. .	80

5.4	PMMA specimen at loading rate $1000 \text{ s}^{-1}$ . Branching patterns at successive times: (a) 3.2; (b) 3.4; (c) 3.6; (d) 3.8; (e) 4.0; (f) 4.6 $\mu\text{s}$ . . . . .	81
5.5	PMMA specimen at loading rate $1000 \text{ s}^{-1}$ ; main crack velocity history, $V_R = 926 \text{ m/s}$ is the Rayleigh wave velocity. The velocity is averaged over a distance of 0.2 mm along the horizontal direction. . . . .	82
5.6	PMMA specimen at loading rate $5000 \text{ s}^{-1}$ . Branching patterns at successive times: (a) 1.08 $\mu\text{s}$ ; (b) 1.28 $\mu\text{s}$ ; (c) 1.48 $\mu\text{s}$ ; (d) 1.68 $\mu\text{s}$ . The arrow of length 0.25 mm indicates the direction of main crack propagation and scales the branches extension. . . . .	83
5.7	PMMA specimen at loading rate $5000 \text{ s}^{-1}$ , time 1.72 $\mu\text{s}$ . The arrow shows a branching angle about 14 degrees. . . . .	84
5.8	PMMA specimen: branching pattern and branching angle at 1.2 $\mu\text{s}$ for the strain rate $10,000 \text{ s}^{-1}$ . The branching angle is between 19 to 24 degrees. . . . .	85
5.9	PMMA specimen: zoomed view of the hackled region at time 0.8 $\mu\text{s}$ and 1 $\mu\text{s}$ , loading rate $10,000 \text{ s}^{-1}$ . . . . .	86
5.10	PMMA specimen: branching pattern compared with experiments for loading rate $10,000 \text{ s}^{-1}$ . . . . .	87
5.11	The mean profile of micro branches obtained by Fineberg and Sharon [44, 43] (hollow symbols) for different propagation velocities compared with numerical simulation (filled diamonds). . . . .	89
5.12	PMMA specimen: loading rate $5000 \text{ s}^{-1}$ . Energy and fracture area evolution. . . . .	91
5.13	Homalite-100 specimen: branching pattern at loading rate $1000 \text{ s}^{-1}$ , at times: (a) 4.7; (b) 5.2; (c) 5.7; (d) 6.2 $\mu\text{s}$ . . . . .	92
5.14	Detailed view of branching pattern for Homalite-100 at 6.2 $\mu\text{s}$ , for loading rate $1000 \text{ s}^{-1}$ . Branching angle about 16.5 degrees. . . . .	93
A.1	Nodes and Gauss points location in a tetrahedra. . . . .	96
A.2	Nodes and gauss points location on a facet. . . . .	98

# List of Tables

3.1	3-D stiffness coefficients for the graphite/epoxy unidirectional composite.	33
3.2	Characteristic plane-strain and plane-stress wave speeds for the graphite/epoxy unidirectional composite. . . . .	34
3.3	Fracture parameters for graphite/epoxy composites. . . . .	35
4.1	Elastic material properties for 4340 Steel and Homalite 100. . . . .	57
4.2	Fracture and cohesive parameters for 4340 Steel, Homalite 100 and Weldon-10 interface. . . . .	57
5.1	Mechanical parameters for PMMA and Homalite-100. . . . .	79
5.2	Fracture parameters for PMMA and Homalite-100. . . . .	80

# Chapter 1 Introduction

## 1.1 Dynamic fracture mechanics

Cracks would cause no one any trouble if they never moved, so it is natural to investigate their dynamics in some detail [76]. Dynamic fracture has been stimulating interest not only because of its fundamental importance in understanding fracture processes and because of practical applications such as engineering and earthquake prediction, but also because of the challenges to mathematical analyses and experimental techniques [52]. As Meyers [82] pointed out, dynamic fracture has its own unique features: there exists a limiting speed of propagating cracks; cracks tend to branch out or bifurcate in order to decrease the overall energy of the system at a certain critical velocity; the fracture toughness of materials is often dependent on the rate of crack propagation. Another essential feature that distinguishes dynamic fracture from quasi-static behavior is the presence of stress waves, either due to externally applied loads or the stresses released from the crack tip at fracture.

There is a threshold time required to activate cracks. When the duration of the applied pulse is less than that amount, the crack does not grow. Furthermore, this threshold time decreases as the stress applied is raised, so the dynamic fracture toughness  $K_{I_d}$  depends on the time duration of the applied pulse, in contrast with the static stress intensity factor. These trends have been confirmed by Ravi-Chandar and Knauss [101], who, for example, showed that the threshold time for Homalite-100 is 50  $\mu\text{s}$ .

The considerable importance of dynamic fracture can be seen in numerous practical applications: crack arrest in engineering structures; prevention of damage in car structures as consequences of impacts as well as in space structures from meteorites; airplane fracture control in explosions; pressure impact failure of submarine ship shells; safety of nuclear-reactor vessels; mining military applications, as fragmen-

tation of bombs and shells and fracture of projectiles and armor. In particular, the design of armor and armor-defeating projectiles requires a deep knowledge of dynamic fracture response of a material.

One compelling need in the army is to understand the failure mechanism in order to minimize the damage to body armors. Recent advances in armor design, for the most part brought about under the leadership of scientists and engineers at the U. S. Army Research Laboratory, provide unprecedented levels of protection which render the currently field combat vehicles the most survivable in the world. For instance, ceramic composites have demonstrated excellent potential for defeating medium and heavy-class long-rod penetrators while minimizing armor weight. In addition, interface defeat mechanisms, such as graphite interlayers, greatly enhance the resistance capabilities of ceramic composites. While recognizing these advances, it is not entirely clear that radically different armor designs do not exist which are capable of vastly superior performance than afforded by the present technology. The identification of such radical armor designs is likely to involve the examination of myriad candidate designs—a process too expensive to be carried out entirely in the laboratory. Therefore advanced simulation, as the chief means of evaluating designs, coupled to optimization, as the vehicle for the systematic exploration of design space, immediately suggest themselves as the only viable option. A conventional armor design relies on a three-layer system: ceramic tile to first blunt and erode the tip of the projectile, an intermediate soft layer to deflect the flow of the incoming threat material, and a metallic backing to finally stop the threat. This design aims to combine the best properties of these three classes of materials, ceramics, binders or lubricants and metals, in a way which maximizes the penetration resistance of the plate. Evidently, the simple ceramic/interface/metal layering is not but the simplest possibility, and other more complex layerings, possibly involving many alternating ceramic and metallic layers, as well as various types of interfaces, may result in superior performance. This calls for detailed understanding for dynamic fracture for layered structures.

Since the progression of fracture is driven by the stress field in the local neighborhood of the crack front, it is necessary to know the relationship between the crack

speed and the local stress field for any type of dynamic analysis [82].

The understanding of how solid materials break apart when external loads are applied is a crucial safety issue that has attracted the attention of engineers and material scientists for a long time [47]. Recently, it has also attracted the attention of physicists, as the complex spatial-temporal dynamics of crack propagation has strong resemblances to other pattern-forming systems such as diffusion limited aggregation, dielectric breakdown or percolation [122, 58, 100, 99].

## 1.2 Interfacial fracture mechanics

Many modern materials and material systems (including protective coatings, multi-layer capacitors, thin film/substrate systems for electronic packages, reaction product layers and adhesive joints) are layered. Interfaces are intrinsic to such materials [64]. As fracture along or near an interface between phases plays a major role in limiting their toughness and ductility, this has motivated a substantial body of work on failure at interfaces [139]. Nevertheless, a fracture mechanics framework for interfacial crack initiation and growth has been developed only relatively recently, and the concept of steady-state cracking analysis provides a simplified solution relevant to design against fracture.

A wide experimental evidence has proved that for fatigue crack growth, stress corrosion cracking and crack advance under monotonic loading, pure mode-I conditions could be maintained at crack tip in brittle isotropic, homogeneous materials. Nevertheless, an unloaded crack subsequently subject to mixed mode loading will kink in a direction that is locally mode I. A crack in a material (for example, unidirectional composites) that has strongly orthotropic fracture properties, or a crack along an interface with a fracture toughness distinct from the materials joined across it, can kink or propagate straight ahead under mixed mode loading depending on a number of factors, including the relative toughness associated with the competing directions of propagation.

The elasticity solutions typically involving oscillatory singularities have been car-

ried out for a variety of interfacial cracks [40, 33, 34, 35, 134, 105, 41, 42, 71, 49, 50, 18]. Such oscillatory singularity is also encountered if a crack lies in one of the constituent, but its tip touches the interface [18]. The serious defect of the oscillatory singularity is that they lead to wrinkling of the faces of the crack and overlapping of the materials [40, 75]. Comninou pointed out that: the interface crack in a tension field has closed tips and the contact regions near the tips are extremely short in comparison to the size of the crack; the singular part of the stress field near the closed tips is quite different from that of the oscillatory singularity; the normal traction is tensile but finite ahead of the crack tip; and only the shear traction is singular there. These observations suggest that the growth of an interface crack is more intimately connected with failure in shear rather than tension. She also obtained a meaningful stress-intensity factor in shear which is connected with the change of free energy. But a singular integral equation must be solved with high precision to find that stress-intensity factor, and an approximate value for the closed tip can be found only if the strength of the oscillatory singularity is known. That might have impeded its further use.

Dundurs (1969) has observed that wide class of plane problems of elasticity for bimetals depend on only two non-dimensional combinations of the elastic moduli. With the conventions set in Fig. 1.1, the Dundurs' elastic mismatch parameters are

$$\alpha = \frac{\mu_1(\kappa_2 + 1) - \mu_2(\kappa_1 + 1)}{\mu_1(\kappa_2 + 1) + \mu_2(\kappa_1 + 1)} = \frac{\overline{E}_1 - \overline{E}_2}{\overline{E}_1 + \overline{E}_2} \quad (1.1)$$

$$\beta = \frac{\mu_1(\kappa_2 - 1) - \mu_2(\kappa_1 - 1)}{\mu_1(\kappa_2 + 1) + \mu_2(\kappa_1 + 1)} \quad (1.2)$$

where  $\overline{E}_i = E_i/(1-\nu_i^2)$ ,  $\kappa_i = 3-4\nu_i$  for plane strain and  $\overline{E}_i = E_i$ ,  $\kappa_i = (3-\nu_i)/(1+\nu_i)$  for plane stress. Thus  $\alpha$  measures the mismatch in the plane tensile modulus across the interface. It approaches 1 when material 1 is extremely stiff compared to material 2, and approaches -1 when material 1 is extremely compliant. Both  $\alpha$  and  $\beta$  vanish when there is no mismatch, and both change signs when the materials are switched.

He and Hutchinson showed that in-plane stress can have a major influence on the behavior of interface cracks. In particular, tensile in-plane stress acts in conjunction

with flaws nears the interface to destabilize interface cracks and causes them to depart from the interface. On the contrary, a compressive in-plane stress stabilizes interface cracks and essentially deactivates flaws around the interface [55].

A crack lying in the interface between two brittle elastic solids can advance either by continued growth in the interface or by kinking out of the interface into one of the adjoining materials. This competition can be assessed by comparing the ratio of the energy release rate for interface cracking and for kinking out of the interface to the ratio of interface toughness to substrate toughness. The stress parallel to the interface influences the energy release rate of the kinked crack and, if sufficiently large, can significantly alter the conditions for interface cracking over substrate cracking [55]. The energy release rate for crack advance along an interface, which is assumed to have zero thickness, is [75]

$$G = \frac{1 - \beta^2}{E_*} (K_I^2 + K_{II}^2) \quad (1.3)$$

where  $E_* = 2\overline{E_1 E_2} / (\overline{E_1} + \overline{E_2})$ . A simple, one parameter family of mixed mode fracture criterion is

$$E_*^{-1} (K_I^2 + \lambda K_{II}^2) = G_I^c \quad (1.4)$$

The parameter  $\lambda$  adjusts the influence of the mode II contribution in the criterion. The limit  $\lambda = 1$  is the “ideally brittle” interface with initiation occurring when  $G = G_I^c$  for all mode combinations, which coincides with the classical surface energy criterion. When  $\lambda = 0$ , crack advance only depends on the mode I component.

### 1.3 Interfacial fracture criterion

Various hypotheses have been made concerning the crack kinking under combined loading in homogeneous material and bimetals [53, 56, 119]. Noticeable are the maximum energy release rate [54] and the minimum strain energy density theories [119]. Several analytical works based on such criteria have been carried out [10, 11,

74, 54, 53, 57, 12, 64].

Banks-Sills *et al.* have examined different criteria for interface fracture and compared them to experimental results obtained from bimaterial Brazilian disk specimens composed of glass and epoxy [14, 13]. The first criterion considered (similar to empirical expressions), based on the energy release rate, is presented by Hutchinson and Suo [64]

$$G_{ic} = G_I(1 + \tan^2\psi) \quad (1.5)$$

where  $G_{ic}$  is the critical energy release rate for the interface;  $G_I \equiv \hat{K}_I^2/H$ ,  $\hat{K} = KL^{i\epsilon}$  is the complex intensity factor and  $L$  is an arbitrary length parameter;  $\psi$  is the phase angle defined by

$$\psi = \arctan\left[\frac{\text{Im}(KL^{i\epsilon})}{\text{Re}(KL^{i\epsilon})}\right] = \arctan\left[\frac{\sigma_{12}}{\sigma_{22}}\right]_{\theta=0, r=L} \quad (1.6)$$

The second criterion refers to Charalambide *et al.* [28] and assumes that fracture is caused by a mode-I energy release rate  $G_0$  which is composed of two parts:

$$G_0 = G_I + \sin^2\omega G_2 \quad (1.7)$$

The criterion could be written as

$$G_{ic} = G_I(1 + \tan^2(\psi - \psi_0)) \quad (1.8)$$

which is essentially the same as (1.5) except for the phase shift  $\psi_0$ , and same as choosing another value for the length parameter  $L$ . This criterion has three free parameters:  $L$ ,  $G_I$  and  $\psi_0$ , among which  $L$  may be arbitrarily chosen and the other two may be obtained from two  $G_{ic}$  tests at different phase angles.

The third criterion considered is the critical hoop stress employed by Thurston and Zehnder [126] for the tests of a specimen containing a nickel interface between

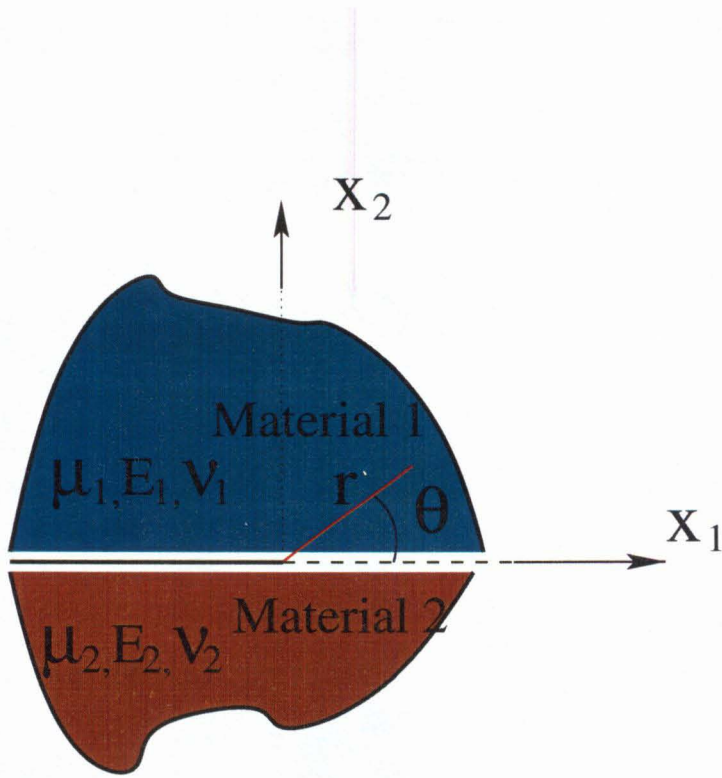


Figure 1.1: Geometry and conventions for an interface crack.

two alumina substrates. It is hypothesized that the crack will propagate when the hoop stress  $\sigma_{\theta\theta}$  reaches a critical value at a distance from the crack tip  $r = r_0$  along the interface, which is equivalent to (1.8).

The fourth one is the critical shear stress criterion, which is self-invalidated because the critical shear stress at a distance  $r_0$  ahead of the crack tip is a function of  $\sigma_{\theta\theta|crit}$  and the phase angle  $\psi$ .

For isotropic elastic solids, the parent straight-ahead quasi-static crack advance is Irwin's relation between the energy release rate and the stress intensity factors:

$$G = (K_I^2 + K_{II}^2)/\bar{E} \quad (1.9)$$

For the local kinked crack, it reads

$$G^t = (K_I^{t2} + K_{II}^{t2})/\bar{E} \quad (1.10)$$

The criteria for kinking based on maximizing  $G^t$  and propagating in local mode-I are almost the same [64].

For homogeneous, orthotropic elastic solids, it is common to consider plane cracks aligned with the principal axes of orthotropy and crack advance that is either straight-ahead or kinked at  $90^\circ$ . For simply connected domains with traction boundary conditions, Suo [123] has shown that the stress depends on only two nondimensional elastic parameters:

$$\lambda = \frac{b_{11}}{b_{22}}, \quad \rho = \frac{b_{11} + b_{66}/2}{\sqrt{b_{11}b_{22}}} \quad (1.11)$$

where  $b_{ij}$  indices are the components of the compliance matrix of the orthotropic material. The energy release rate for straight ahead crack advance is

$$G = b_{11}n(\lambda^{-3/4}K_I^2 + \lambda^{-1/4}K_{II}^2) \quad (1.12)$$

and that of the kinked crack tip is

$$G^t = b_{22}n(\lambda^{3/4}K_I^{t2} + \lambda^{-1/4}K_{II}^{t2}) \quad (1.13)$$

If

$$\frac{G}{G^t} > \frac{\Gamma_0}{\Gamma_{90}} \quad (1.14)$$

the crack will advance straight ahead, since the condition  $G = \Gamma_0$  will be reached before  $G^t = \Gamma_{90}$ . The crack will advance kinking at  $90^\circ$  if inequality (1.14) is reversed.

## 1.4 Numerical trends

The first calculations carried out for fracture were by Neville Mott who took on the response to the Liberty ship disasters during World War II. His work led to an amazingly successful scaling theory, which stood up well into the increasingly improved math-

ematics, except the agreement with experiments [76]. During the last few decades, many numerical methods such as finite-element methods with non-singular and singular elements [16], boundary element method, the boundary collocation method [88], the body force method, the integration method as well as dislocation method [29], and recently meshless methods (in particular, the element-free Galerkin method [45]) have been proposed to model crack problems. The extended finite-element method (X-FEM) by Daux *et al.* [37] uses the notion of partition of unity to allow crack growth without remeshing. The approach enriches the standard approximation with additional functions and allows the modeling of arbitrary geometric features independently of the finite element mesh.

Several avenues have been traditionally followed in order to model fracture. One avenue is to attempt to bury all dissipative mechanisms into the constitutive relations. However, in practice the effective behavior of systems with complex microstructures can only be characterized analytically, by recourse to sweeping simplifying assumptions. One particularly vexing difficulty inherent to constitutive descriptions concerns their inability to endow brittle materials with a well-defined fracture energy, i. e., a material-characteristic measure of energy dissipation per unit area of crack surface. Thus, the conventional thermodynamic route to the formulation of general constitutive relations regards dissipation as an extensive quantity possessing a well-defined density per unit volume. Attempts to build fracture into such formulations by means of a softening stress-strain law leads to pathologies such as a spurious scaling of the effective fracture energy with the discretization size. The formulation of appropriate functional forms of the energy of a solid which allow for both bulk-like and fracture-like behavior is a challenging mathematical problem which is presently the subject of active research [22, 46].

Classical fracture mechanics specifically addresses the issue of whether a body under load will remain intact or new free surface will form. However, the classical theory of fracture mechanics is predicated around the assumption of a *pre-existing* dominant crack. Under these and other restrictive assumptions, fracture mechanics successfully predicts when a crack will grow, in what direction and how fast, and how the results

of laboratory experiments can be scaled up to structural dimensions. However, the reliance on a pre-existing dominant crack entirely foregoes the issue of nucleation, which is for the most part foreign to classical fracture mechanics. Situations, such as those that arise in fragmentation or crushing, involving many intersecting cracks also fall outside the purview of classical fracture mechanics. Additionally, the conditions for crack growth are typically expressed in terms of parameters characterizing the amplitude of autonomous near-tip fields. The applicability of these criteria is therefore contingent upon the existence and establishment of such near-tip fields. This in turn severely restricts the scope of the theory, e. g., by requiring that the plastic or process zone be small relative to any limiting geometrical dimension of the solid such as the ligament size, conditions which are rarely realized in materials such as concrete. In addition, the structure of the autonomous near-tip fields depends sensitively on the constitutive behavior of the material, which inextricably ties the fracture criteria to the constitution of the material. In dynamic fracture, the fracture criterion is additionally responsible for accounting for the micro inertia which accompanies the motion of the crack tip. Another complicating factor is non-proportional and cyclic loading, such as arises in high-cycle fatigue, which renders important near-tip parameters, such as the  $J$ -integral, inapplicable.

An alternative approach to fracture is based on the use of cohesive models (see, e. g., [39, 15, 104, 59, 109, 27, 83, 90, 133, 84, 85, 136, 137, 130, 93, 98, 138, 91, 26, 132, 131, 139, 38, 92, 97, 96, 110, 111]) which regard fracture as a gradual process in which the separation of the incipient crack flanks is contrasted by cohesive tractions. A “cohesive law” governs the relation between the cohesive tractions and the opening displacements. Cohesive models furnish a complete theory of fracture which is not limited by any consideration of material behavior, finite kinematics, non-proportional loading, dynamics, or geometry of the specimen. In addition, cohesive theories fit naturally within the conventional framework of finite-element analysis, and have proved effective in the simulation of complex fracture processes. Noticeable examples include the fragmentation of brittle materials [26, 103]; dynamic fracture and fragmentation of ductile materials [96, 94]; and dynamic tests for concrete [110, 111]. As Camacho

and Ortiz [26] observed, the accurate description of fracture processes by means of cohesive elements requires the resolution of the characteristic cohesive length of the material. In some materials, such as ceramics and glass, this length may be exceedingly small. Thus calculations based on cohesive elements inevitably have a *multiscale* character, in as much as the numerical model must resolve two disparate length scales commensurate with the macroscopic dimensions of the solid and the cohesive length of the material.

# Chapter 2 Finite-element methodology

## 2.1 Introduction

This chapter introduces the main mechanical components of the finite element methodology. Within the context of the Lagrangian framework we begin by expressing in variational form the problem of an elastic-plastic solid undergoing dynamic large deformations. The field and constitutive equations, the time discretization and a minimum principle for the incremental problem are presented. Throughout the calculations, we will refer to 3D meshes triangulized by 10-node tetrahedra.

## 2.2 Field and constitutive equations

We take the initial configuration  $B_0 \subset \mathbb{R}^d$  of the body at time  $t_0$  as the reference configuration.

The motion of the body is described by a time-dependent deformation mapping  $\varphi : B_0 \times [t_0, \infty) \rightarrow \mathbb{R}^d$ . The local deformation of infinitesimal material neighborhoods is described by the deformation gradient

$$\mathbf{F} = \nabla_0 \varphi, \quad \text{in } B_0 \quad (2.1)$$

where  $\nabla_0$  denotes the material gradient over  $B_0$ . The motions of the body follow the equation of motion (*cf.* [79])

$$\nabla_0 \cdot \mathbf{P} + \rho_0 \mathbf{B} = \rho_0 \ddot{\varphi}, \quad \text{in } B_0 \quad (2.2)$$

where  $\rho_0$  is the mass density over  $B_0$ ,  $\mathbf{B}$  are the body forces per unit mass,  $\mathbf{P}$  is the first Piola-Kirchhoff stress tensor, and  $\ddot{\varphi}$  is the material acceleration field. For purposes of formulating boundary conditions, we partition the boundary  $\partial B_0$  of  $B_0$

into a Dirichlet or displacement boundary  $\partial B_{01}$  and a Neumann or traction boundary  $\partial B_{02}$ . The displacement boundary conditions then take the form:

$$\boldsymbol{\varphi} = \bar{\boldsymbol{\varphi}}, \quad \text{on } \partial B_{01} \quad (2.3)$$

where  $\bar{\boldsymbol{\varphi}}(\mathbf{X}, t)$  is the prescribed deformation mapping on  $\partial B_{01}$ . The traction boundary conditions then take the form:

$$\mathbf{P} \cdot \mathbf{N} = \bar{\mathbf{T}}, \quad \text{on } \partial B_{02} \quad (2.4)$$

where  $\mathbf{N}$  is the unit outward normal to  $\partial B_{02}$  and  $\bar{\mathbf{T}}(\mathbf{X}, t)$  are the prescribed tractions applied to  $\partial B_{02}$ . In addition, the formulation of the problem requires the initial deformation mapping and material velocity field,  $\boldsymbol{\varphi}$  and  $\dot{\boldsymbol{\varphi}}$ , respectively, to be supplied.

## Bulk material

Within a nonlinear kinematics framework, we adopt a multiplicative elastic-plastic kinematics of the form [70], [125], [106]:

$$\mathbf{F} = \mathbf{F}^e \cdot \mathbf{F}^p \quad (2.5)$$

where the deformation gradient  $\mathbf{F}$  is decomposed into an elastic part  $\mathbf{F}^e$  and into a plastic part  $\mathbf{F}^p$ . The free energy density  $A$  decomposes additively as

$$A = W^e(\mathbf{F}^e, T) + W^p(\mathbf{F}^p, \mathbf{Q}) \quad (2.6)$$

where  $T$  denotes the temperature and  $\mathbf{Q}$  a suitable collection of internal variables. In the present application, with good approximation we need only account for the elastic contribution. Thus  $A$  can be written as

$$A \equiv W^e(\mathbf{F}^e, T) = \frac{1}{2}(\boldsymbol{\varepsilon}^e - \boldsymbol{\alpha}T)^T \mathbf{c}(\boldsymbol{\varepsilon}^e - \boldsymbol{\alpha}T) = \frac{1}{2}c_{ijkl}(\varepsilon_{ij}^e - \alpha_{ij}T)(\varepsilon_{kl}^e - \alpha_{kl}T) \quad (2.7)$$

where  $\mathbf{c}$  is the elastic tensor and  $\boldsymbol{\alpha}$  is the thermal expansion tensor. The logarithmic strain  $\boldsymbol{\varepsilon}^e$  is given by

$$\boldsymbol{\varepsilon}^e = \log\sqrt{\mathbf{C}^e} = \frac{1}{2}\log(\mathbf{F}^{eT}\mathbf{F}^e) \quad (2.8)$$

where  $\mathbf{C}^e$  is the right Cauchy-Green deformation tensor, associated with the elastic part of the deformation.

## 2.3 Finite element model

We make recourse to the finite element method to discretize the continuum. Inserting the displacement interpolation into the virtual work expression leads to a system of semi-discrete equations of motion of the form:

$$\mathbf{M}\ddot{\mathbf{x}} + \mathbf{F}^{\text{int}}(\mathbf{x}) = \mathbf{F}^{\text{ext}}(t) \quad (2.9)$$

where  $\mathbf{x}$  is the array of nodal coordinates,  $\mathbf{M}$  is the mass matrix,  $\mathbf{F}^{\text{ext}}$  is the external force array, and  $\mathbf{F}^{\text{int}}$  is the internal force array. In calculations we use the second-order accurate central difference algorithm to discretize (2.9) in time [17, 62, 63]. Despite the fact that the time step is bounded by stability [62], explicit integration is particularly attractive in three-dimensional calculations, where implicit schemes lead to system matrices which often exceed the available in-core storage capacity. Yet another advantage of explicit algorithms is that they are ideally suited for concurrent computing [81].

### Time discretization

Next we envision a process of incremental deformation and seek to determine the solution at discrete times  $t_0, \dots, t_{n+1} = t_n + \Delta t, \dots$ . We begin by discretizing the equations of motion (2.2) in time. Thus, we invert the usual sequence of spatial and temporal discretization and discretize the governing equations in time prior to the

introduction of a spatial discretization. For definiteness, we restrict our attention to the Newmark scheme [63, 17]:

$$\boldsymbol{\varphi}_{n+1} = \boldsymbol{\varphi}_n + \Delta t \mathbf{v}_n + \Delta t^2 [(1/2 - \beta) \mathbf{a}_n + \beta \mathbf{a}_{n+1}] \quad (2.10)$$

$$\mathbf{v}_{n+1} = \mathbf{v}_n + \Delta t [(1 - \gamma) \mathbf{a}_n + \gamma \mathbf{a}_{n+1}] \quad (2.11)$$

$$\rho_0 \mathbf{a}_{n+1} = \nabla_0 \cdot \mathbf{P}_{n+1} + \rho_0 \mathbf{B}_{n+1} \quad (2.12)$$

where  $\mathbf{v}$  and  $\mathbf{a}$  denote the material velocity and acceleration fields, and  $\beta \in [0, 1/2]$  and  $\gamma \in [0, 1]$  are the Newmark's parameters. This defines a non linear system of equations that can be solved using a Newton-Raphson iteration procedure. For the dynamic simulations that are presented in the following chapters, the explicit version of the previous system of equations is used. The second order accurate explicit scheme we used is obtained by assuming  $\beta = 0$  and  $\gamma = 1/2$  (see, [63, 17])

$$\boldsymbol{\varphi}_{n+1} = \boldsymbol{\varphi}_n + \Delta t \mathbf{v}_n + \frac{1}{2} \Delta t^2 \mathbf{a}_n \quad (2.13)$$

$$\mathbf{a}_{n+1} = \mathbf{M}^{-1}(\mathbf{R}_{n+1}^{ext} - \mathbf{R}_{n+1}^{int}) \quad (2.14)$$

$$\mathbf{v}_{n+1} = \mathbf{v}_n + \frac{1}{2} \Delta t (\mathbf{a}_{n+1} + \mathbf{a}_n) \quad (2.15)$$

The presented scheme is stable under the condition that the time step is below a critical time step. Typically, one would like to capture numerically dilatational waves propagation on any element of the mesh. The stable time step that is used in the calculations is

$$\Delta t_{\text{stable}} = C \frac{h_{\min}}{c_d} \quad (2.16)$$

where  $C$  is a security coefficient (of the order of 0.1),  $h_{\min}$  is the minimum element size for the mesh,  $c_d$  is the dilatational wave speed of the bulk material. The stable time step is computed at regular intervals during the calculations and after every remeshing in case the bulk material mesh changes during computational time.

## 2.4 Cohesive formulation

The stress field of linear elastic fracture mechanics diverge as  $1/\sqrt{r}$  approaching the crack tip. In reality, the stress value must be bounded. The actual phenomena in the process zone that limit the stress are unquestionably complicated. Barenblatt and Dugdale proposed a simple cohesive zone model to cancel the apparent elastic singularity around the crack tip [15, 39]. So at distances from the crack tip very large compared to the cohesive zone size  $R$ , the energy release rate due to the singular stress field is

$$G = \frac{1 - \nu^2}{E} A_I(\nu) \sigma_c^2 \frac{8R}{\pi} \quad (2.17)$$

where  $E$  is the Young's modulus;  $\nu$  is the Possion's ratio;  $A_I(\nu)$  is a universal function of crack propagation function [47];  $\sigma_c$  is the critical opening stress for a constant cohesive law. Inverting equation (2.17) and replacing  $G$  with the specific fracture energy  $G_c$  give the characteristic cohesive length:

$$R = \frac{\pi E G_c}{8(1 - \nu^2) A_I(\nu) \sigma_c^2} \quad (2.18)$$

Various cohesive models have been used to describe the process of formation of a new surface in fracture mechanics. Fracture parameters - such as fracture energy - have been incorporated into those models for the material description. Different cohesive laws could be applied to address the separation process, while the bulk material behavior is described through an independent set of constitutive relations.

The feasibility of using cohesive theories of fracture for the direct simulation of fragmentation in brittle materials subjected to impact was established by Camacho and Ortiz, while the applications involving dynamic fracture of ductile materials has been investigated by Pandolfi *et al.* [94, 96]. Repetto *et al.* [103] have applied cohesive models to the simulation of failure waves in glass rods subjected to impact, and correctly captured the development of a sharp failure wave, its propagation speed and its bursting of the comminuted material following the passage of the failure wave.

In presence of a cohesive surface, the weak form of linear momentum balance, or virtual work expression, takes the following form

$$\int_{B_0} [\rho_0(\mathbf{b} - \ddot{\boldsymbol{\varphi}} \cdot \boldsymbol{\eta} - \mathbf{P} \cdot \nabla_0 \boldsymbol{\eta})] dV_0 - \int_{s_0} \mathbf{t} \cdot [\boldsymbol{\eta}] dS_0 + \int_{\partial B_{0,2}} \bar{\mathbf{t}} \cdot \boldsymbol{\eta} dS_0 = \mathbf{0} \quad (2.19)$$

where  $B_0$ ,  $S_0$ ,  $dS_0$ ,  $\partial B_{0,2}$  are defined in Fig. 2.3. The consideration of the cohesive traction brings a new term in the virtual work expression. The definition of the cohesive law can be based on the assumption of the existence of a free energy density

$$\phi = \phi(\boldsymbol{\delta}, \theta, \mathbf{q}; \mathbf{n}) \quad (2.20)$$

where

$$\boldsymbol{\delta} = [\boldsymbol{\varphi}] \quad (2.21)$$

is the opening displacement over the cohesive surface,  $\theta$  is the local temperature,  $\mathbf{q}$  is the set of internal variables describing the current state of decohesion of the surface,  $\mathbf{n}$  is the unit normal to the cohesive surface in deformed configuration. The dependence on  $\mathbf{n}$  permits differentiation the cohesive behavior for opening and sliding. By recourse to Coleman and Noll's method, the cohesive law takes the form:

$$\mathbf{t} = \frac{\partial \phi}{\partial \boldsymbol{\delta}} \quad (2.22)$$

The cohesive behavior is completed by defining the evolution of internal variables which are governed by a set of kinetic relations of the general form

$$\dot{\mathbf{q}} = f(\boldsymbol{\delta}, \theta, \mathbf{q}) \quad (2.23)$$

A simple expression of the cohesive law can be derived by defining (Camacho and

Ortiz, 1996) the effective opening displacement

$$\delta = \sqrt{\beta^2 \delta_S^2 + \delta_n^2} \quad (2.24)$$

where

$$\begin{aligned} \delta_n &= \delta \cdot \mathbf{n} \\ \delta_S &= |\boldsymbol{\delta} - \delta_n \mathbf{n}| \end{aligned}$$

are the normal and sliding displacement respectively.

Assuming  $\phi$  depend on  $\boldsymbol{\delta}$  only through  $\delta$ , then

$$\phi = \phi(\delta, \theta, \mathbf{q}; \mathbf{n}) \quad (2.25)$$

we have

$$\mathbf{t} = \frac{t}{\delta} (\beta^2 \boldsymbol{\delta}_S + \delta_n) \quad (2.26)$$

where

$$t = \frac{\partial \phi}{\partial \delta}(\delta, \theta, \mathbf{q}) = \sqrt{\beta^{-2} |\mathbf{t}_S|^2 + \mathbf{t}_n^2} \quad (2.27)$$

where  $\beta$  defines the ratio between the shear and the normal resistance and roughly gives the ratio of  $K_{IIc}$  to  $K_{Ic}$  of the material.

Fig. 2.1 depicts the irreversible cohesive law used in our simulation for isotropic materials, where  $\sigma_c$  and  $\delta_c$  remain the same for all the cohesive elements of a fixed material; a cohesive law that can be applied to transversely cohesive materials is described in the following section. Irreversibility manifests itself upon unloading. Therefore, an appropriate choice of internal variable is the maximum attained effective opening displacement  $\delta_{\max}$ . Loading is then characterized by the conditions:  $\delta = \delta_{\max}$  and  $\dot{\delta} \geq 0$ . Conversely, we shall say that the cohesive surface undergoes unloading

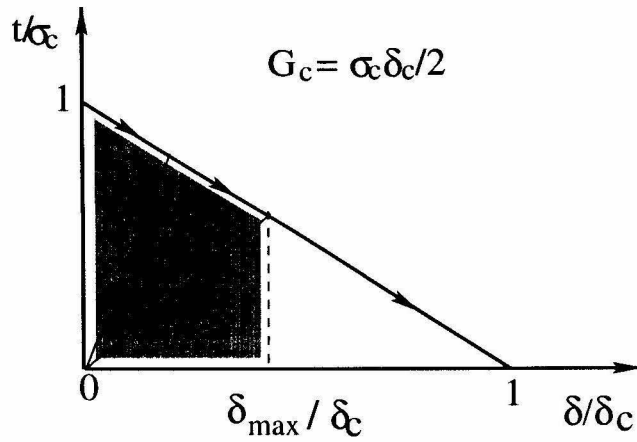


Figure 2.1: Linear loading and unloading behavior.

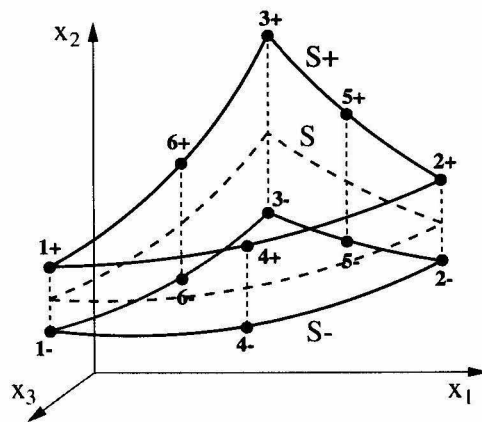


Figure 2.2: Geometry of a 3D cohesive element. The surfaces  $S^+$  and  $S^-$  coincide in the reference configuration of the solid [92].

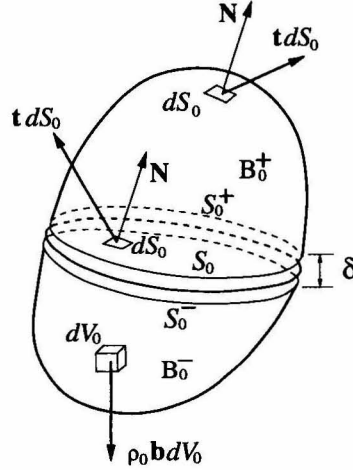


Figure 2.3: Cohesive surface traversing a 3D body.

when it does not undergo loading. We assume the existence of a loading envelop defining a relation between  $t$  and  $\delta$  under conditions of loading. From equation (2.27), for small values of  $\beta$ , the the initiation of a cohesive crack is ostensibly independent of the magnitude of normal tractions.

Camacho and Ortiz first proved that the cohesive theories introduce a well-defined length scale, and in conjunction with inertia, a well-defined time scale, into the material description. The characteristic length of the material is

$$l_c = \frac{EG_c}{\sigma_c^2} \quad (2.28)$$

where  $E$  is Young's modulus;  $G_c$  is the specific fracture energy (or the dynamic crack propagation energy, represents the resistance of the material to crack advance);  $\sigma_c$  the material spall strength. As a consequence of this intrinsic scale, cohesive model are sensitive to the size of mesh, and the characteristic time is

$$t_c = \frac{\rho c \delta_c}{2\sigma_c} \quad (2.29)$$

where  $\rho$  is the material density;  $c$  is the wave speed;  $\delta_c$  is the critical opening displacement. Owing to the time scale, the material behaves differently when subjected to fast and slow loading rates, which confers on the cohesive model the ability to

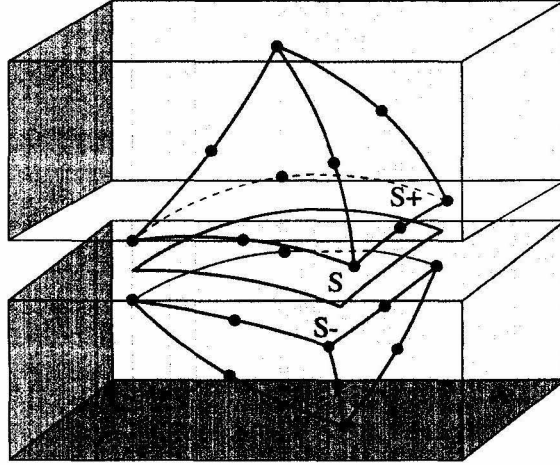


Figure 2.4: Assembly of 12-node triangular cohesive element and two 10-node tetrahedral elements.

reproduce subtle features of dynamic behavior of brittle solids, such as crack growth initiation time and propagation speed and the dependence of the pattern fracture and fragmentation on strain rates. This has been verified by Ruiz *et al.* [112] in the simulations of advanced ceramics.

The class of cohesive elements considered consists of two surface elements which coincide in space in the reference configuration of the solid, Fig. 2.3. The particular triangular geometry depicted is compatible with three-dimensional tetrahedral elements, Fig. 2.4.

## 2.5 Transversely isotropic cohesive law

The transversely isotropic behavior manifests itself especially in fracture events. A meso-modeling for composite materials was introduced and discussed in [7, 36, 8], where the authors proposed the dependence of a cohesive law on the direction of fibers of adjacent layers. A recent work by Ravichandran [89] enhanced the strong dependence of the fracture energy and fracture toughness on the relative orientation of the fracture surface and fibers. A very simple way to render such dependence is to assume that the tensile strength varies sinusoidally with the inclination of the fracture surface (see Fig. 2.5). If  $\alpha$  is the angle between the fibers and the normal to

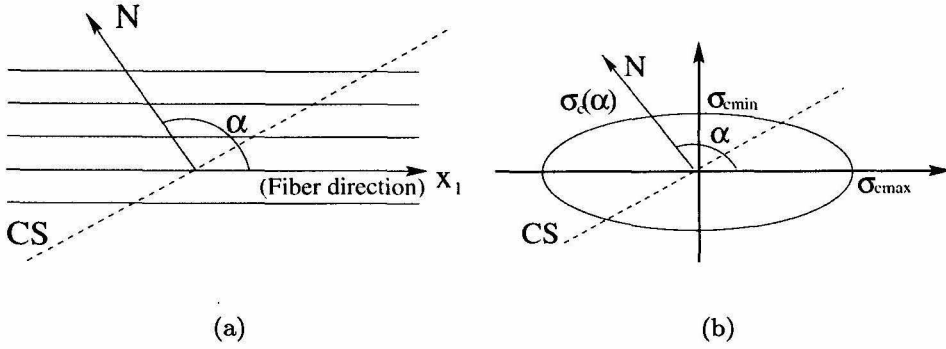


Figure 2.5: Transversely isotropic cohesive law: (a) a cohesive surface CS, the normal  $N$  is inclined to the fiber direction at angle  $\alpha$ ; (b) the cohesive strength for surface CS.

the fracture surface, we can write

$$\sigma_c(\alpha) = \sigma_{cmin} + (\sigma_{cmax} - \sigma_{cmin}) |\cos\alpha| \quad (2.30)$$

where  $\sigma_{cmax}$  denotes the maximum tensile strength, in the direction parallel to the fibers, and  $\sigma_{cmin}$  the minimum tensile resistance, normally to the fibers (Fig. 2.5). Assuming a cohesive model for the description of the progressive decohesion between two separating surfaces, the characteristic strength of the material will vary locally according to equation (2.30).

## 2.6 Small strain friction/contact algorithm

Upon closure, the cohesive surfaces are subject to the contact unilateral constraints, possibly including friction [92]. Contact must be regarded as an independent phenomenon to be modeled outside the cohesive law. A rigorous approach to frictional contact would require, though, a complex and expensive implementation (see e.g., [66, 95]). In our application, the contact process is mainly constrained near the middle surface of the specimen, so we choose as expedient to incorporate a simple small-strain contact law, as described in the following.

We superimpose a very simple model of contact elements to the cohesive elements.

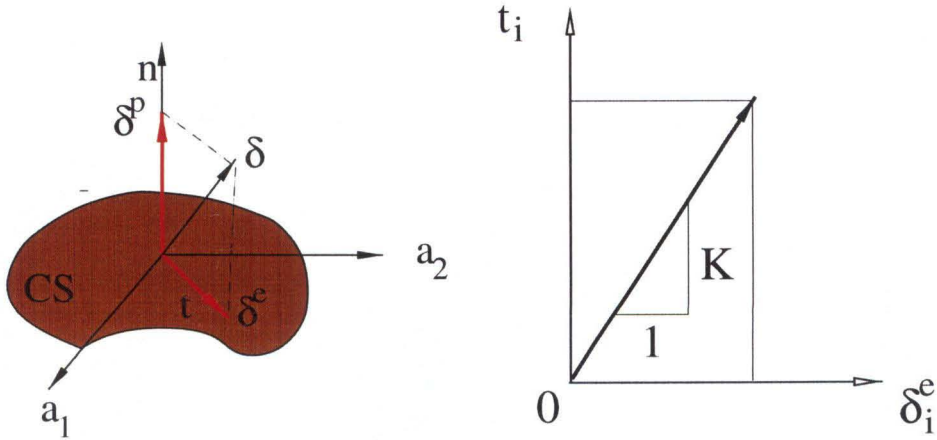


Figure 2.6: Frictional contact model: (a) decomposition of the jump  $\delta$  as sum of the elastic normal displacement  $\delta^e$  (negative) and irreversible tangential displacement  $\delta^p$ ; (b) contact law for the direction  $i$ , in the penetration case.

Contact and cohesive elements share the same global nodes and facets. When the normal component of the opening displacement  $\delta_n$  is negative, denoting interpenetration between the two fracture surfaces, the relation between opening displacement and surface traction is governed by a frictional contact law. Specifically, the normal component of the surface reaction follows a linear elastic response, whereas the tangential component obeys the classic Coulomb's friction law.

Let  $\delta = \llbracket \mathbf{u} \rrbracket$  denote the displacement jump across the contact surface,  $\mathbf{t}$  the tractions,  $\mathbf{n}$  the unit normal, Fig. 2.6. Given any vector  $\mathbf{x}$ , its normal component is

$$x_n = \mathbf{x} \cdot \mathbf{n} \quad (2.31)$$

whereas its tangential component is

$$\mathbf{x}' = \mathbf{x} - x_n \mathbf{n} \quad (2.32)$$

In particular, we write  $p = t_n$  for the normal contact pressure. We assume an additive

decomposition:

$$\boldsymbol{\delta} = \boldsymbol{\delta}^e + \boldsymbol{\delta}^p \quad (2.33)$$

into an elastic or recoverable displacement jump  $\boldsymbol{\delta}^e$  and a frictional or irrecoverable displacement jump  $\boldsymbol{\delta}^p$ . We set

$$\boldsymbol{\delta}^p = \boldsymbol{\delta}', \quad \text{if } \delta_n > 0, \quad (2.34)$$

i. e., in the absence of contact. The tractions follow in the form

$$\mathbf{t} = \begin{cases} 0 & \text{if } \delta_n \geq 0 \\ K \boldsymbol{\delta}^e = K (\boldsymbol{\delta} - \boldsymbol{\delta}^p) & \text{otherwise} \end{cases} \quad (2.35)$$

where  $K$  is the elastic stiffness of the surface, computed as

$$K \approx \frac{\lambda + 2\mu}{h_{min}} \quad (2.36)$$

$\lambda$  and  $\mu$  are the Lamé constants of the bulk material,  $h_{min}$  is the minimum mesh size.

The rate of irreversible sliding obeys the rule

$$\dot{\boldsymbol{\delta}}^p = \dot{\boldsymbol{\delta}}^p \frac{\mathbf{t}'}{\tau} \quad (2.37)$$

where

$$\tau = |\mathbf{t}'| \quad (2.38)$$

is the shear stress magnitude acting on the surface, and  $|\dot{\boldsymbol{\delta}}^p|$  is the magnitude of the irreversible sliding rate. Finally, we assume that frictional sliding requires that

$$f = \tau - \tau_c(p) = 0 \quad (2.39)$$

where  $\tau_c(p)$  is the critical shear at pressure  $p$ . The loading unloading conditions are,

therefore,

$$f \leq 0, \text{ and } \dot{\delta}^p \geq 0, \text{ and } f \dot{\delta}^p = 0 \quad (2.40)$$

In the case of Coulomb friction we have that

$$\tau_c = -\mu p, \quad p < 0 \quad (2.41)$$

The exact equations are solved by a fully implicit update, distinguishing the following cases:

**Case 1. No contact.**

In the absence of contact,  $\delta_n > 0$ , we simply set

$$\delta_{n+1}^p = \delta'_{n+1} \quad (2.42)$$

$$\mathbf{t}_{n+1} = \mathbf{0} \quad (2.43)$$

and exit.

**Case 2. Stick.**

In the presence of contact,  $\delta_n < 0$ , we start by evaluating the elastic or *stick* predictor:

$$\delta_{n+1}^{p,pre} = \delta_n^p \quad (2.44)$$

$$\mathbf{t}_{n+1}^{pre} = K (\delta_{n+1} - \delta_{n+1}^{p,pre}) = K (\delta_{n+1} - \delta_n^p) \quad (2.45)$$

If

$$\tau_{n+1}^{pre} \leq \tau_c(p_{n+1}^{pre}) \quad (2.46)$$

then we conclude that there is no frictional sliding during the step, set

$$\boldsymbol{\delta}_{n+1}^{p,pre} = \boldsymbol{\delta}_{n+1}^{p,pre} \quad (2.47)$$

$$\mathbf{t}_{n+1} = \mathbf{t}_{n+1}^{pre} \quad (2.48)$$

$$D\mathbf{t}_{n+1} = K \mathbf{I} \quad (2.49)$$

and exit. In (2.49),  $D\mathbf{t}_{n+1}$  is the tangent stiffness matrix of the contact.

### Case 3. Slip.

If there is contact and the friction condition (2.46) is violated by the stick predictor, then slip must necessarily occur during the time step. In this case we write:

$$\boldsymbol{\delta}_{n+1}^p = \boldsymbol{\delta}_n^p + \Delta\delta^p \frac{\mathbf{t}'_{n+1}}{\tau_{n+1}} \quad (2.50)$$

$$p_{n+1} = p_{n+1}^{pre} \quad (2.51)$$

$$\mathbf{t}'_{n+1} = K (\boldsymbol{\delta}'_{n+1} - \boldsymbol{\delta}_{n+1}^p) \quad (2.52)$$

$$\tau_{n+1} = \tau_c(p_{n+1}) \quad (2.53)$$

A useful identity which follows from these equations is

$$\frac{\mathbf{t}'_{n+1}}{\tau_{n+1}} = \frac{\mathbf{t}'_{n+1}^{pre}}{\tau_{n+1}^{pre}} \quad (2.54)$$

which fixes the direction of slip. It also follows that

$$\Delta\delta^p = \frac{\tau_{n+1}^{pre} - \tau_c(p_{n+1})}{K} \quad (2.55)$$

which solves the update equations explicitly. Finally, linearization of the update gives the tangent stiffness matrix:

$$D\mathbf{t}_{n+1} = K \left( \mathbf{n} - \mu \frac{\mathbf{t}'_{n+1}^{pre}}{\tau_{n+1}^{pre}} \right) \otimes \mathbf{n} \quad (2.56)$$

which, as may be seen, is not symmetric.

## 2.7 Thermal effects

In order to account thermal effects, we refer to the general heat equation:

$$\rho c_v \frac{\partial T}{\partial t} = \nabla \mathbf{q} + g \quad (2.57)$$

where  $c_v$  is the thermal capacity,  $\mathbf{q}$  the heat flux,  $g$  the heat source and  $T$  temperature. For a fast propagating crack, the frictional heat is limited near the crack surface. Assuming adiabatic heating, we adopt the following discretization at time  $t_{n+1}$ :

$$dw_{n+1} = \frac{dW_{n+1}}{L} = \rho c_v (T_{n+1} - T_n) \quad (2.58)$$

where  $dW$  is the incremental frictional work,  $L$  a characteristic length for the adiabatic heating, defined so that it describes the thickness of the adiabatic layer.

## 2.8 Fragmentation algorithm

In order to follow the evolution of the geometry of a three-dimensional finite-element model as a consequence of fracture and fragmentation, a simple adaptive procedure according to Pandolfi and Ortiz [95] is here applied.

Pandolfi and Ortiz's approach to fragmentation is based on the explicit modeling of the crack evolution. The basic idea is that in a 3D finite element discretization, all the potential cracks are represented by the interfaces between solid elements. In a tetrahedral 3D mesh, a fine discretization is able to guarantee a good set of crack paths in different directions. Special crack paths, as material interfaces, are included in the solid model by several interelement triangular surfaces. The adaptive procedure remodels the original mesh by the insertion of cohesive elements between two solid elements previously coherent. During the numerical analysis, the nucleation of the crack along an interface is related to the attainment of a critical condition. This is generally represented by a scalar inequality that must be chosen in agreement with the problem at the hand. In our dynamic analysis we applied the "effective traction

criterion,” which is related to the decomposition of the traction  $\mathbf{t}$  acting on the interface into normal  $t_n$  and tangential  $t_s$  components. Assigning different weights to sliding and normal components, the effective traction  $t_{\text{eff}}$  is computed as

$$t_{\text{eff}} = \sqrt{\beta^{-2}|t_s|^2 + t_n^2}, \quad \beta = \frac{\tau_c}{\sigma_c} \quad (2.59)$$

The facet is fractured when

$$t_{\text{eff}} \geq t_{\text{max}} = \sigma_c \quad (2.60)$$

$\sigma_c$  is the cohesive strength. Once that criterion is met, the interface is remodeled by a cohesive element, whose insertion leads to changes into the connectivities of the adjacent elements and to insertion of new nodes.

# Chapter 3 Intersonic Crack Growth in Asymmetrically Loaded Unidirectional Composite Plates

## 3.1 Introduction

In homogeneous materials and in the absence of a preferential crack growth path, mode-II crack propagation is somehow prevented by the natural kink of the crack tip, which propagates in a direction defined by a local mode-I stress state. This is not necessarily true in solids that may be homogeneous regarding their constitutive properties but may involve preferable crack paths in the form of weak planes of lower toughness. Indeed, dynamic crack growth along weak planes is the predominant mode of failure in composites and other layered materials. The presence of a weak straight line crack path, a characteristic that may accommodate growing cracks of both opening and shear modes, makes the unidirectional composite a natural candidate for studying the maximum allowable crack tip speeds of both modes in a macroscopically homogeneous system.

In the past years, tests on dynamic crack growth along weak planes of composite specimens showed that interfacial crack tip speeds rapidly approach and exceed the shear wave speed  $c_s$  of the more compliant material [67, 72, 121, 120, 107]. A crack speed exceeding the shear wave speed and lower than the longitudinal wave speed of a material is called intersonic. In isotropic or anisotropic homogeneous elastic solids, purely elastodynamic crack growth theory excludes intersonic growth of mode-I cracks. Though, in cases of self-similar cracks growing into their own planes, the possibility of intersonic mode-II crack growth is not excluded [23]. The issue of the evaluation of the critical speed  $v_c$  at which intersonic crack growth is possible has

been addressed by several researchers [25, 48, 23, 60, 61, 24]. These works were mainly concerned with isotropic materials, and fiber-reinforced composites received less attention. A description of the most relevant results in this field can be found in [31, 32].

Intersonic crack tip speeds are characterized by a ray emanating from the crack tip, related to a jump in the shear tractions (shear shock wave). This feature has been predicted theoretically and observed experimentally and numerically [72, 121, 86, 87]. In order to obtain intersonic crack tip speeds, the loading conditions and the bond strength are such that they promote the locally shear dominated deformations at the crack tip. Those deformations are further enhanced by the stress wave mismatch, due to the elastic properties discontinuity across the interface.

A wealth of experimental results concerning dynamic crack growth tests on unidirectional composites has been recently presented by Coker and Rosakis [31, 108, 32]. They used unidirectional graphite/epoxy composite plates, with an edge pre-notch machined in the fiber direction, either symmetrically or asymmetrically loaded by impact in a one-point bend configuration. For asymmetric –mode-II– type of loading, the results revealed highly unstable and intersonic shear-dominated crack growth along the fibers. The interferograms obtained by the lateral shearing interferometric technique of coherent gradient sensing (CGS) featured a shock wave structure typical of disturbances traveling with speeds higher than the characteristic wave speeds in the solid. A further experimental outcome was the evidence of large-scale frictional contact.

Coker and Rosakis experiments provide a challenging comparative collection of data for a new application of cohesive models. Cohesive theories are demonstrating themselves as one of the most appealing and reliable approaches to numerical simulation of complex fracture processes. As main feature, they do not suffer the well-known shortcomings of classical fracture mechanics.

In this chapter we investigate the feasibility of cohesive theories of fracture, incorporated with small strain contact and friction, to the simulation of intersonic crack growth in asymmetrically loaded unidirectional composite plates, in the particular

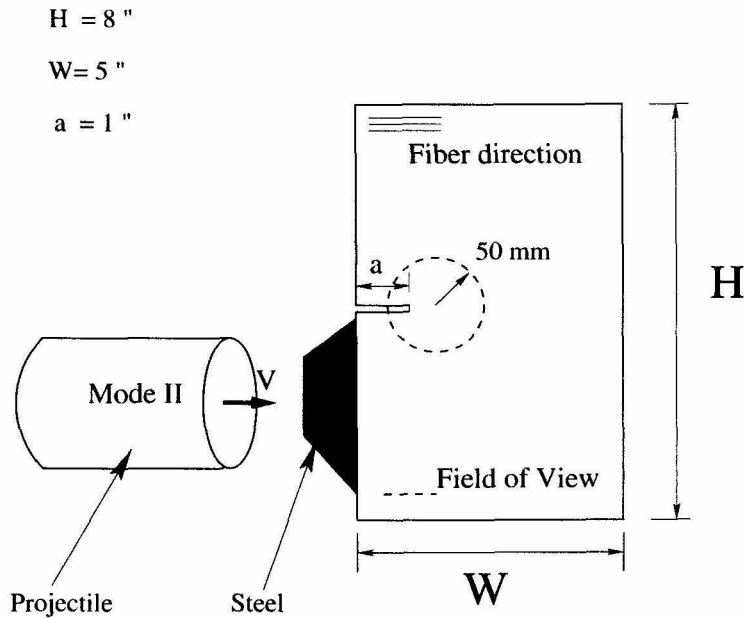


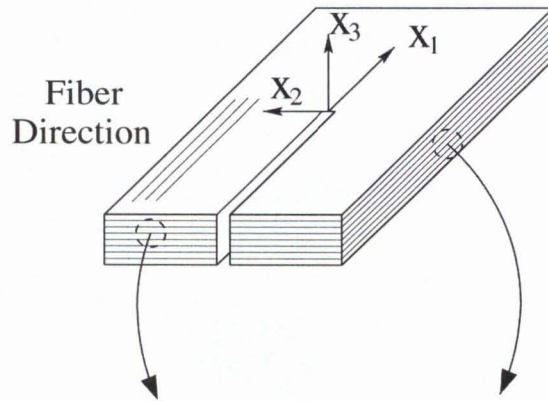
Figure 3.1: Single edge notch (SEN) specimen geometry and size for shear dominated dynamic fracture experiments.

configuration tested by Coker and Rosakis [31, 32]. We aim to reproduce the most complex features arisen from the experiments, including the observed double shock wave structure, the large scale contact as well as the “hot spots” generated by frictional heating.

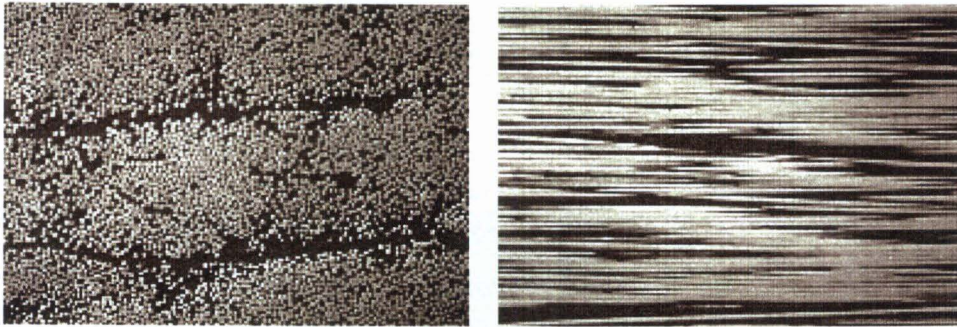
## 3.2 Material properties and experimental set-up

The plates, used in the asymmetric loading condition experiments, have an edge pre-notch machined in the fiber direction. They are loaded by impact in a one-point bend configuration. The impact speed of the projectile during the experiments was varying from 10 to 57 m/s. The loading apparatus is sketched in Fig. 3.1.

The specimens used by Coker and Rosakis [31, 32] are unidirectional composite plates, 7 mm thick, formed by 48 layers of graphite fiber in epoxy matrix. The plates are 150 mm in width and 75 mm in height. The specimen dimensions are reported in Fig. 3.1. Crosssections of the composite, normal and parallel to the fiber respectively,



(a)



(b)

Figure 3.2: Crosssection of fiber-reinforced unidirectional graphite/epoxy composite.

are shown in Fig. 3.2b.

## Material properties

The orientation of an orthonormal coordinate set with respect to the composite plates is shown in Fig. 3.2a. The  $x_1$  axis is defined to lie along the fibers, the  $x_3$  axis is perpendicular to the plane of the composite surface (with an outward pointing unit vector), while the  $x_2$  axis is perpendicular to  $x_1 - x_3$  plane. If we assume the fibers are randomly distributed in the epoxy matrix, then the  $x_1 - x_3$  plane can be taken as a plane of isotropy, and the material may be considered transversely isotropic. The

constitutive relation is therefore [30]:

$$\begin{bmatrix} \sigma_1 = \sigma_{11} \\ \sigma_2 = \sigma_{22} \\ \sigma_3 = \sigma_{33} \\ \sigma_4 = \sigma_{23} \\ \sigma_5 = \sigma_{13} \\ \sigma_6 = \sigma_{12} \end{bmatrix} = \begin{bmatrix} c_{11} & c_{12} & c_{12} & 0 & 0 & 0 \\ c_{12} & c_{22} & c_{23} & 0 & 0 & 0 \\ c_{12} & c_{23} & c_{22} & 0 & 0 & 0 \\ 0 & 0 & 0 & c_{44} & 0 & 0 \\ 0 & 0 & 0 & 0 & c_{66} & 0 \\ 0 & 0 & 0 & 0 & 0 & c_{66} \end{bmatrix} \begin{bmatrix} \varepsilon_1 = \varepsilon_{11} \\ \varepsilon_2 = \varepsilon_{22} \\ \varepsilon_3 = \varepsilon_{33} \\ \varepsilon_4 = \varepsilon_{23} \\ \varepsilon_5 = \varepsilon_{13} \\ \varepsilon_6 = \varepsilon_{12} \end{bmatrix}, \quad \boldsymbol{\sigma} = \mathbf{c}\boldsymbol{\varepsilon} \quad (3.1)$$

where

$$c_{44} = \frac{c_{22} - c_{23}}{2} \quad (3.2)$$

The stiffness matrix  $\mathbf{c}$  for a transversely isotropic matrix is defined by five independent parameters:  $c_{11}$ ,  $c_{22}$ ,  $c_{12}$ ,  $c_{23}$  and  $c_{66}$ . The value of the stiffness coefficients for the unidirectional composite used here are collected in Table 3.1.

Coefficient	$c_{11}$	$c_{22}$	$c_{12}$	$c_{23}$	$c_{66}$	$c_{44}$
GPa	82	11.1	4.0	4.9	3.6	3.1

Table 3.1: 3-D stiffness coefficients for the graphite/epoxy unidirectional composite.

The stiffness constants are related to the mechanical parameters  $E_1$ ,  $E_2$ ,  $\mu_{23}$ ,  $\mu_{12}$  and  $\nu_{12}$  (easily measurable with standard laboratory tests) through the following relations:

$$E_1 = c_{11} - \frac{2c_{12}^2}{c_{22} + c_{23}}, \quad E_2 = \frac{(c_{22} - c_{23})(c_{11}c_{22} + c_{23}c_{11} - 2c_{12}^2)}{c_{11}c_{22} - c_{12}^2} \quad (3.3)$$

$$\nu_{12} = \frac{c_{12}}{c_{22} + c_{23}}, \quad \nu_{21} = \frac{c_{12}(c_{22} - c_{23})}{c_{11}c_{22} - c_{12}^2}, \quad \nu_{23} = \frac{c_{23}c_{11} - c_{12}^2}{c_{11}c_{22} - c_{12}^2} \quad (3.4)$$

$$\mu_{12} = c_{66}, \quad \mu_{23} = \frac{c_{22} - c_{23}}{2} = \frac{E_2}{2(1 + \nu_{23})} \quad (3.5)$$

Specifically, the shear modulus  $\mu_{12}$  was determined by quasi-static Iosipescu shear test, while uniaxial compression tests were conducted on an MTS hydraulic testing machine to evaluate Young's moduli,  $E_1$  and  $E_2$ , and the Poisson ratio,  $\nu_{12}$ .

The values of the coefficients  $c_{11}$ ,  $c_{22}$  and  $c_{66}$ , computed through eqs. (3.5), were also compared with the ones obtained from the plane strain longitudinal and shear wave speeds in the direction of the major axis, using the following relations:

$$c_i^{\parallel} = \sqrt{\frac{c_{11}}{\rho}}, \quad c_i^{\perp} = \sqrt{\frac{c_{22}}{\rho}}, \quad c_s = \sqrt{\frac{c_{66}}{\rho}} \quad (3.6)$$

The longitudinal wave speeds parallel  $c_i^{\parallel}$  and perpendicular  $c_i^{\perp}$  to the fibers and the shear wave speed  $c_s$  were obtained using ultrasonic pressure and shear transducers operating at 5 MHz frequency. The mass density of the composite plate was 1478  $kg/m^3$ . Table (3.2) reports the measured wave speeds values, for both plane stress and plane strain conditions. In the same table the Rayleigh speed  $c_R^{\parallel}$  for waves propagating in the fibers direction is reported.

Wave type	Plane strain (m/s)	Plane stress (m/s)
$c_i^{\parallel}$	7450 $\pm$ 100	7380
$c_i^{\perp}$	2740 $\pm$ 100	2740
$c_s$	1560 $\pm$ 50	1560
$c_R^{\parallel}$	1548	1548

Table 3.2: Characteristic plane-strain and plane-stress wave speeds for the graphite/epoxy unidirectional composite.

The fracture properties for the unidirectional graphite/epoxy composite are collected in Table 3.3.

Fracture toughness	$K_{Ic}$	2.2 MPa $\sqrt{\text{m}}$
Fracture energy	$G_{Ic}$	474.0 N/m
Maximum cohesive stresses	$\sigma_c$	35.8 MPa
Critical opening displacement	$\delta_c$	0.0265 mm
Weighting coefficient	$\beta$	0.726

Table 3.3: Fracture parameters for graphite/epoxy composites.

## Optical technique

The coherent gradient sensing (CGS) is a shearing interferometric technique that is sensitive to in-plane gradients of out of plane displacements in reflection mode and in-plane stress gradients in transmission mode. A detailed description of the technique and of the equations governing optical mapping and fringe formation can be found in [127, 128]. A schematic of the experimental set-up along with the CGS optical technique is shown in Fig. (3.3). For opaque materials, CGS uses a coherent, monochromatic, collimated laser beam incident on the specimen and reflected from the initially optically flat and specularly reflective surface. Near the crack tip, the reflected beam acquires an optical path difference, due to the non-uniformly deformed surface of the specimen. The reflected beam crosses two high density line diffraction gratings of pitch  $p = 0.0254$  mm (40 lines/mm), normal to  $x_3$  direction (see Fig.( 3.3)) and separated by a distance  $\Delta$ . The gratings diffract the reflected beam and recombine it to form an interferogram. The reflected light is collected by a filtering lens, which blocks all but either of the  $\pm 1$  diffraction orders. One of those two remaining diffraction spots is imaged to produce an interference pattern on the image plane of a high-speed camera.

When used in reflective mode, CGS measures the in-plane gradients of out-of-plane displacement  $u_3(x_1, x_2)$  [127, 128]:

$$u_{3,1} = \frac{\partial u_3}{\partial x_1} = \frac{mp}{2\Delta}, \quad m = 0, \pm 1, \pm 2, \dots \quad (3.7)$$

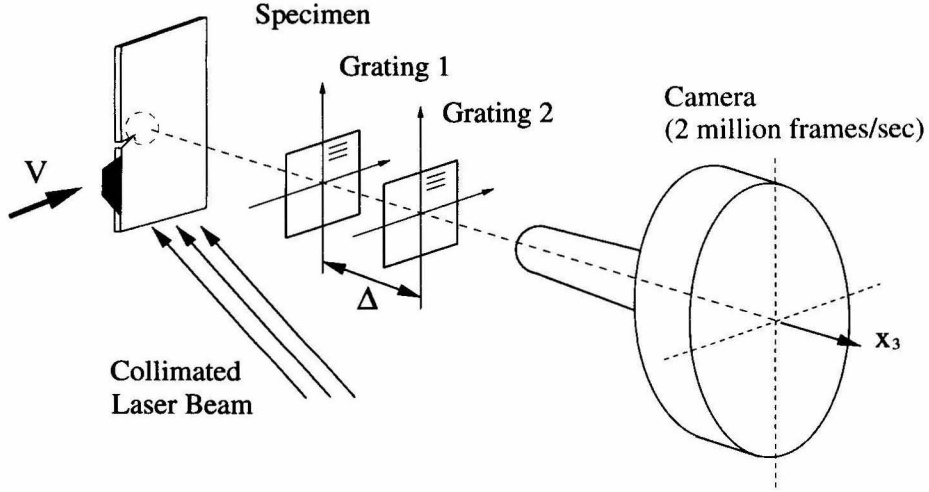


Figure 3.3: Schematic of the experimental set-up and optical technique of coherent gradient sensing (CGS).

where  $m$  is the fringe order for the  $x_1$  gradient. Eq. (3.7) holds when the lines of gratings are parallel to  $x_2$  direction. Each CGS fringe is a locus of points of constant  $u_{3,1}$  on the specimen surface. Under plane stress conditions,  $u_3(x_1, x_2)$  is related to the average stresses across the thickness as follows [68, 73]:

$$u_3 = \frac{h}{2}(b_{31}\sigma_{11} + b_{32}\sigma_{22}) \quad (3.8)$$

where  $h$  is the specimen thickness and  $b_{ij}$  are components of the compliance matrix  $\mathbf{b}$ , inverse to the stiffness matrix  $\mathbf{c}$  in eq. (3.1).

## Meaningful experimental observations

A sequence of six CGS interferograms, corresponding to shear dominated dynamic crack growth along the fibers, is shown in Fig. 3.4 [31, 32]. As the crack propagates, it accelerates and further dramatic changes can be observed in the shapes of the crack-tip fringe patterns. The fringes are pushed further back and elongated. The rear loop shape changes from rounded to a triangular wedge, bounded by a line of highly concentrated fringes emerging from the crack tip at a well-defined angle. This

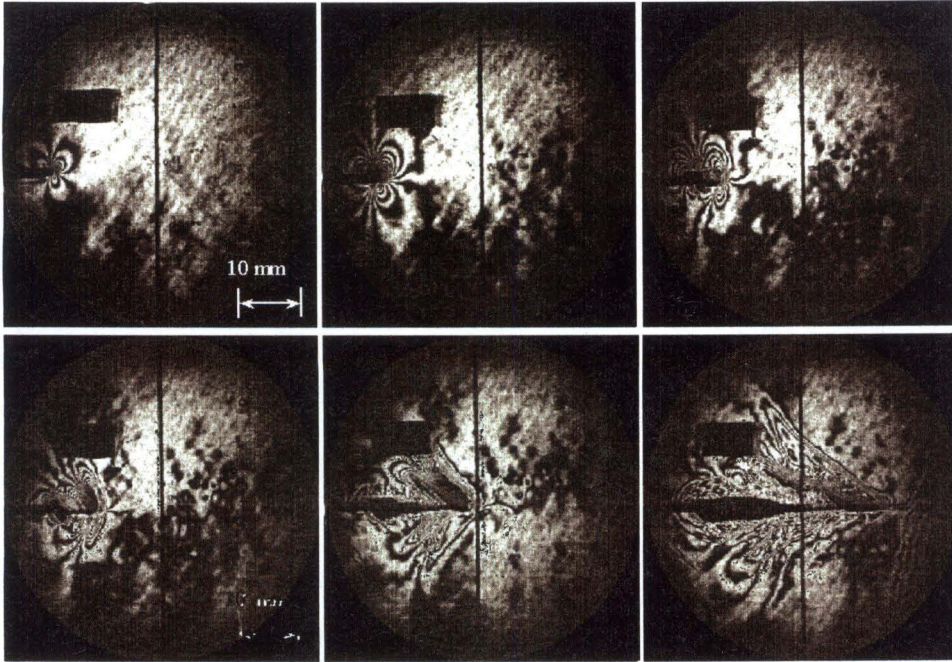


Figure 3.4: A selected sequence of CGS interferograms for an intersonically propagating crack tip at time 2.8, 4.2, 5.6, 6.9, 8.3, 9.7  $\mu\text{s}$ . The field of view is a 50 mm diameter circle around the notch tip.

line is caused by a steep change in the stress gradients in a localized area, which later (as the crack exceeds the shear wave speed) forms a discontinuity in the stress, i. e., a shear shock wave [72, 107]. Finally this line broadens into two parallel lines (a double shock wave) which intercept the crack surfaces over a finite area of about 4-5 mm behind the crack tip. One possible reason for the observed double shock wave structure may be the existence of a finite size contact region behind the crack tip. This contact region is indeed clearly shown by the “hot spots” captured by an infrared camera. Pictures recorded by the infrared camera are collected in Fig. 3.5. It bears emphasis that the crack-tip speed approaches 7000 m/s, 3.3 times higher than the shear wave speed and clearly intersonic [31, 32].

The elastic asymptotic field analysis of Huang *et al.* [61] on unidirectional fiber-reinforced composites also verifies the existence of a limit or critical speed in intersonic range. Huang *et al.* showed that for Mode-II intersonically propagating crack tip, the power of the stress singularity is always between 0 and 1/2. For general orthotropic

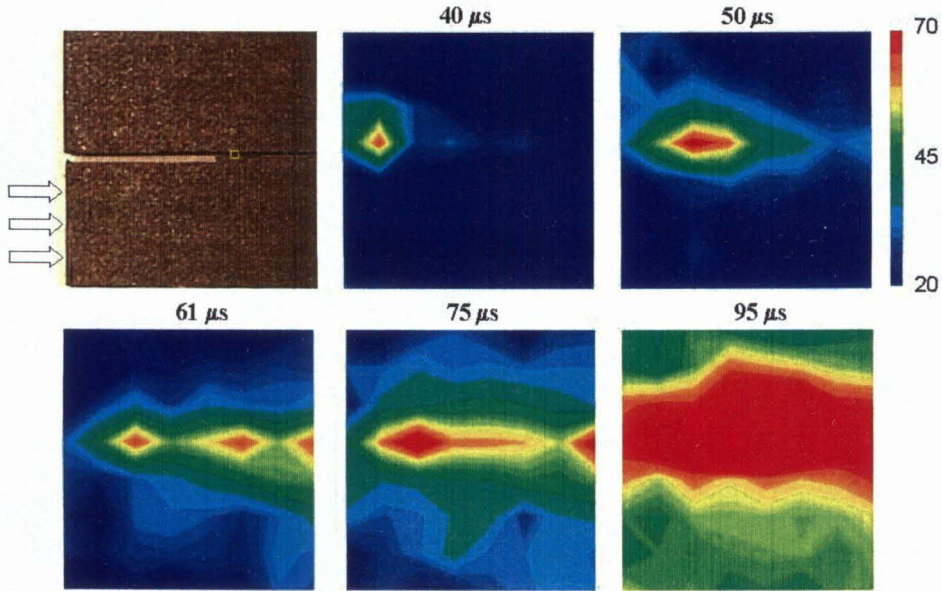


Figure 3.5: High-speed infrared images of hot spot formation due to contact behind an intersonically moving shear crack.

materials there is only one crack tip velocity  $v_c$  that gives a square-root singularity. Its expression is

$$v_c = c_s \sqrt{\frac{c_{11}c_{22} - c_{12}^2}{c_{66}(c_{12} + c_{22})}} \quad (3.9)$$

For graphite/epoxy composite, this yields  $v_c = 6327m/s$ .

### 3.3 Numerical results

We illustrate the three-dimensional simulations of the crack growth in asymmetrically loaded unidirectional composite plates, which demonstrate the scope and versatility of the finite element formulation described in chapter 2. The contemplated configuration is shown as in Fig. 3.1. The effect of the bullet impact is approximated by prescribing a velocity profile, Fig. 3.6a, over the contact area. The impulse duration  $t_p$  is  $27.3 \mu s$ ;

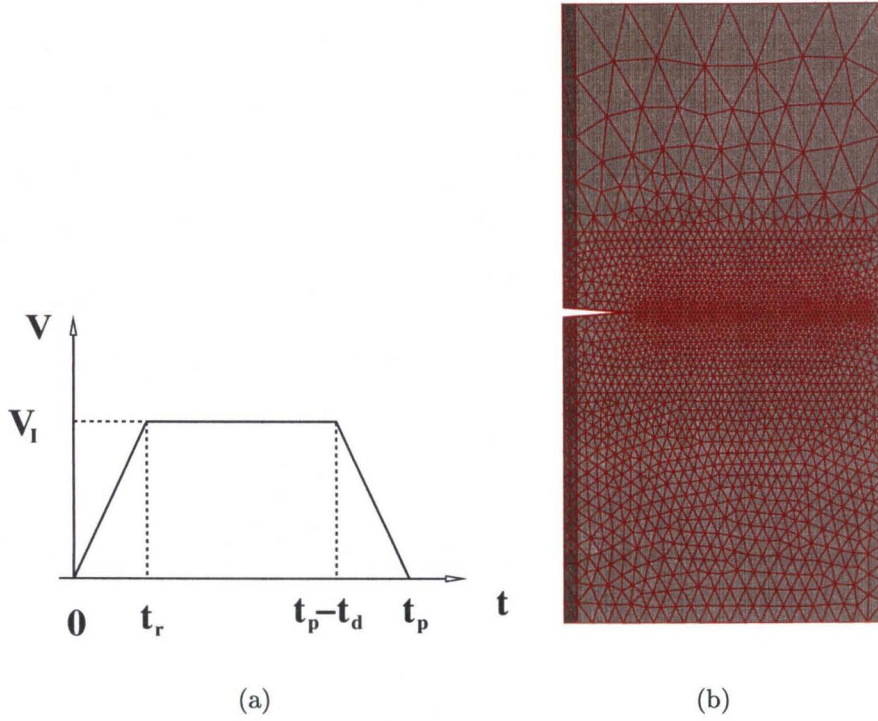


Figure 3.6: Computational model: (a) Impact velocity versus time; (b) 3-D mesh:  $\bar{h}_{min} = 1$  mm, 44,593 nodes and 24,685 elements.

both the rise time  $t_r$  and the step down time  $t_d$  are  $2 \mu\text{s}$ ; impact velocity is 30 m/s.

The 3-D computational mesh (see Fig. 3.6) comprises 44,593 nodes and 24,685 ten-node quadratic tetrahedra elements. Cohesive elements are adaptively inserted at the interfaces between solid elements, according to the stress level reached during the computation. The mesh is very fine along the expected crack path. It is also designed such that it is finer in the bottom part, where the impact occurs, and coarser in the top part. The minimum mesh size  $\bar{h}_{min}$  along the expected crack path is 1 mm, and it has been chosen in order to resolve the process zone of fracture. The size of the cohesive zone has been evaluated as follows. For a Dugdale-Barrenblatt mode-I crack –where the cohesive stress takes a constant value  $\sigma_{ave}$  up to a critical opening displacement  $\delta_c$  and vanishes henceforth [39], [15]– the size  $R$  of the cohesive

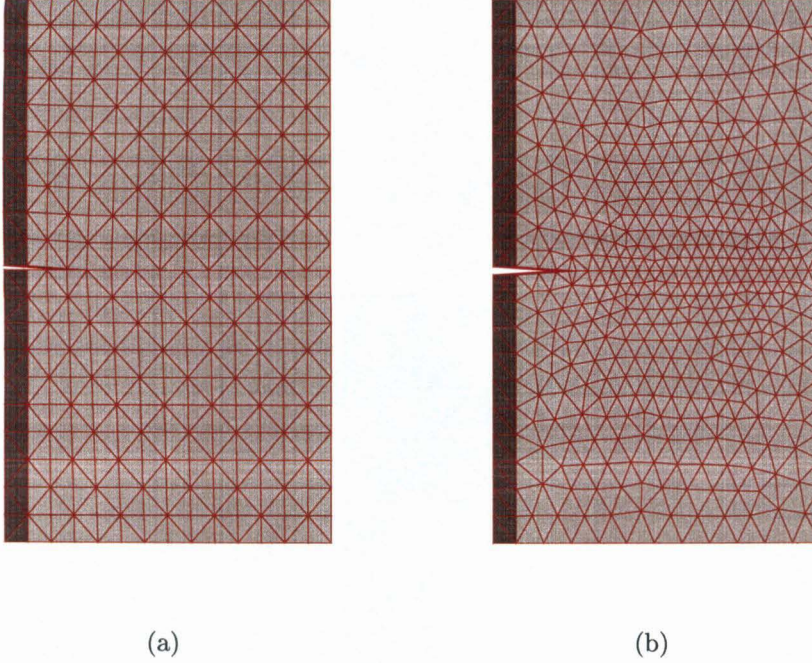


Figure 3.7: Alternative meshes: (a) mesh C1:  $h_{min} = 3$  mm, 3,356 nodes, 1,573 elements; (b) mesh C2,  $h_{min} = 1.43$  mm, 5,465 nodes, 2,666 elements.

zone according to equation 2.18 in quasi-static conditions is given by [104]:

$$R = \frac{\pi E G_c}{8(1 - \nu^2) \sigma_{ave}^2} \quad (3.10)$$

where  $E$  is the Young modulus,  $\nu$  the Poisson ratio and  $G_c$  the fracture energy. In order to apply the above expression to a linearly decreasing cohesive envelop, we assume  $\sigma_{ave} = 0.5 \sigma_c$ . The corresponding cohesive zone size is  $R = 5.5$  mm, which is larger than the minimum mesh size.

In order to verify the mesh independency for the chosen  $\bar{h}_{min}$ , we performed some additional analysis using two coarser meshes, i. e., C<sub>1</sub> ( $h_{min} = 3$  mm) and C<sub>2</sub> ( $h_{min} = 1.43$  mm), Fig. 3.7. The comparison is done through the crack tip history plots and crack tip speed versus crack tip position plots, see Fig. 3.8. Mesh C<sub>2</sub> gives results very close to the ones obtained with the computational mesh. Both the meshes closely capture the crack propagation speed, which oscillates around the limit value

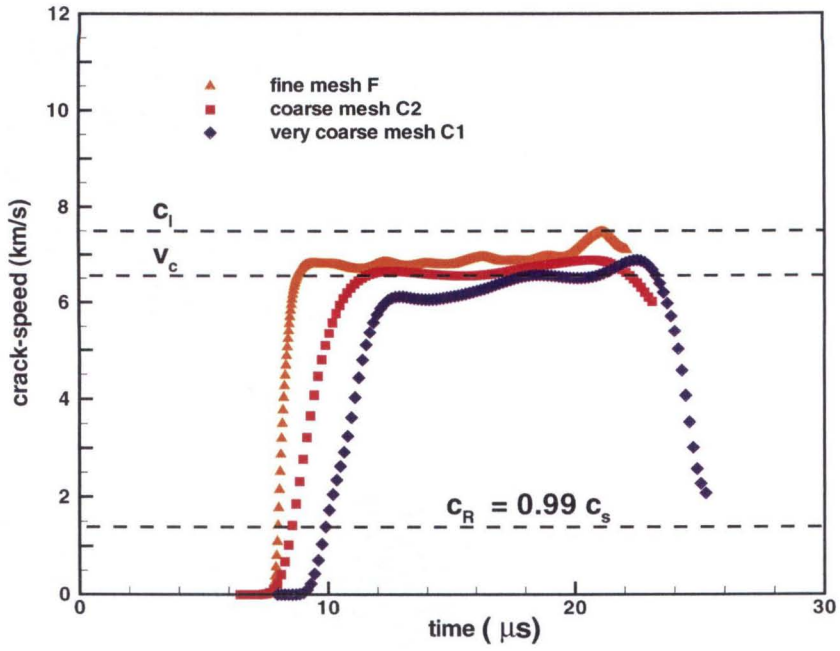
$v_c = 6450$  m/s [31, 32]. It is though evident that the first mesh gives a more realistic stress wave structure, thus the simulation performed in order to display stress and thermal effects has been done with the finest mesh. Mesh C<sub>2</sub> has been instead used for the parametric study, where the crack propagation speed was the main concern, in order to reduce the computational effort.

## Comparison with experiments

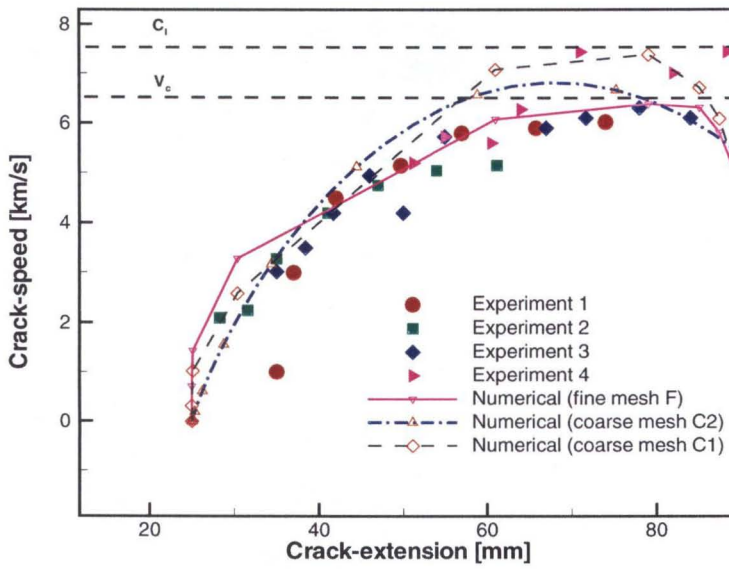
Contour levels of the normal stress component in  $x_2$  direction,  $\sigma_{22}$ , at four different times in the calculation are shown in Fig. 3.9. The stress range is -3 to 3 MPa. At the early stage of the crack propagation, time  $10.8 \mu\text{s}$  after the impact (Fig. 3.9a), a broad band of compressive stresses inclined at an angle about 30 degrees clearly forms at the top side of the crack. At the same time, a distinct unstressed zone, surrounded by compressive stresses, forms at the bottom part of the crack. The strong stress discontinuity testifies that the crack tip speed is bigger than the shear wave speed. In the next phases, at  $14.4$  and  $18.6 \mu\text{s}$  (Fig. 3.9b,c), a double shock wave structure becomes evident. In the last picture (Fig. 3.9d), after the stress wave reached the rear edge of the specimen, a more complex structure is observed.

A comparison between the calculated wave structure around the crack tip and the corresponding experimental CGS fringes at time  $18.6 \mu\text{s}$  is given in Fig. 3.10. The agreement between the two images is noteworthy.

The evolution of the crack is very well described by the damage contour levels along the crack tip, Fig. 3.11. Damage is defined as the ratio between the expended cohesive energy density and the fracture energy density, and its value ranges 0 to 1. A null value denotes a closed fracture; the value 1 represents a fully damaged or open crack, where the cohesive tractions are zero. The cross sections of the specimen along the straight crack path depicted in Fig. 3.11 show a curved thin zone of transition between undamaged and full cracked material, which can be regarded as the extension of the process zone. The crack propagates from the left side to the right side of the specimen. At time  $22.2 \mu\text{s}$  after the impact, the crack is completely open. The curved



(a)



(b)

Figure 3.8: Crack position and speed history computed from mesh with different mesh sizes, comparison with experimental data.

shape of the transition zone is typical for a Mode-II crack propagation.

A comparison between the temperature raise in a region near the crack surface and the experimentally observed “hot-spots” is presented in Fig. 3.12. At the initial stage of the crack propagation, the temperature quickly increases in a very small region around the formed crack surface. The temperature contour levels across the specimen section are drawn in Fig. 3.13. The region near the specimen boundary clearly shows a higher temperature increase, which can be related to a strong degree of contact.

### 3.4 Parametric studies

A sensitivity analysis of the crack-tip trajectory and velocity to the impulse time, the cohesive strength and the impact speed  $\sigma_c$  is shown in Fig. 3.14, 3.15 and 3.16.

As may be seen from Fig. 3.14, where the impact speed and the cohesive strength have been kept constant (50 m/s and 35.8 MPa respectively), the impulse duration affects both the crack tip trajectory and velocity. The numerical experiments explored the effect of impulse duration in the range 2.5-31  $\mu$ s. For an impulse duration greater than 4  $\mu$ s, the crack reaches the critical speed  $v_c$ . For shorter impulse durations, the crack propagation clearly shows two distinct phases. In the earlier stage the crack reaches an intersonic speed (above the Rayleigh speed); then the speed drops quickly, because the energy supply is not enough to keep it constant. The crack arrests, before starting again its propagation, going through the specimen. For a very small duration of the impulse (e. g., 2.5  $\mu$ s), the crack tries to jump to intersonic speeds, but it drops immediately because of lack of energy. The duration of 2.75  $\mu$ s shows a typical transitional situation, where the crack speed oscillates between  $c_R$  and  $v_c$ .

For the cohesive strength sensitivity analyses, Fig. 3.15, we keep the characteristic length  $R$  in eq. (3.10) constant. Therefore, we modify with the same rate the critical opening displacement  $\delta_c$  and the cohesive strength  $\sigma_c$ . The impulse duration is kept at 31  $\mu$ s and the impact speed at 30 m/s. We explore the cohesive strength range 0.1 to 7 times the experimental value ( $\sigma_c = 35.8$  MPa). Correspondingly, the cohesive

energy density varies in the range 0.01 to 49 times the experimental value. The ratio between the current and the original cohesive strength is given by  $R_s$ . The crack speed history and the crack speed versus the crack position are plotted in Fig. 3.15. It may be noticed that the main effect of an increase (decrease) in  $\sigma_c$  is to retard (anticipate) the crack-growth initiation time, and to reduce (increase) the maximum propagation speed. For high values of  $\sigma_c$  the propagation speed does not reach the Rayleigh wave speed, and as a consequence, the crack arrests shortly after initiation. It is noteworthy that for a small value of  $\sigma_c$  the crack speed gets close to the longitudinal wave speed, in keeping with the observations previously done by Needleman [86]. For  $R_s$  ranging between 5 to 7, the crack propagation speed shows two phases. Initially it always tries to reach the critical speed  $v_c$ . If the energy supply is not enough, the crack tends to arrest, jumping again to high speeds once a sufficient amount of energy is accumulated. A clear example of this behavior is given by  $R_s = 7$ .

The investigation regarding the effects of the impact speed, upon the same impulse duration (31  $\mu$ s) and the same cohesive strength (35.8 MPa), is illustrated in Fig. 3.16. When the impact speed exceeds 20 m/s, the crack propagation speed quickly reaches the critical speed  $v_c$  and then keeps a constant value. A smaller impact speed delays the crack initiation time, which can barely reach the critical speed; afterwards the crack arrests without splitting the specimen. For very high impact speeds, the crack speed approaches the longitudinal wave speed (7450 m/s).

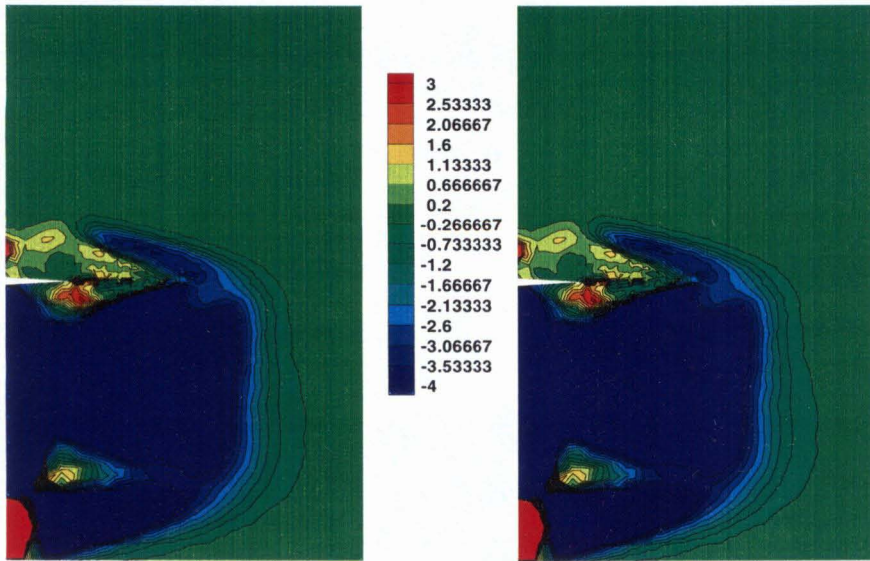
In Fig. 3.17, the minimum impact speed for the crack to achieve the limit speed  $v_c$  at different impulse durations with respect to the same cohesive strength 35.8 MPa is plotted. It is obvious that in order to obtain the speed  $v_c$ , a minimum amount of energy is required; such amount is supplied through a combination of impulse duration and impact speed. It follows that, for the the crack to travel at  $v_c$  speed, at a fixed impact speed, the impulse duration must cover a minimum time; whereas, at a fixed impulse duration, the impact speed needs to reach a minimum value. Notice that in real experiments, the duration of the impulse is related to the length of the impact bullet; this simulation can offer an approximate guide for the projectile design.

### 3.5 Summary

We have applied the cohesive theories of fracture, in conjunction with the direct simulations of fracture and fragmentation, to the numerical simulation of intersonic crack propagation in unidirectional graphite/epoxy composite plates. The experiments performed by Coker and Rosakis in a asymmetric configuration [31, 32] have been taken as a convenient basis for assessing the fidelity and predictive ability of cohesive models of fracture in applications involving dynamic crack growth. Fracture has been modeled by recourse to an irreversible cohesive law embedded into three-dimensional cohesive elements. These cohesive elements govern all aspects of the separation of the incipient cracks, whereas a simple frictional contact element has been superimposed in order to account for the crack closure. The cohesive behavior of the material is assumed to be rate independent and, consequently, all rate effects predicted by the calculations are due to inertia. The numerical models were calibrated by means of experimentally obtained constitutive and cohesive law parameters.

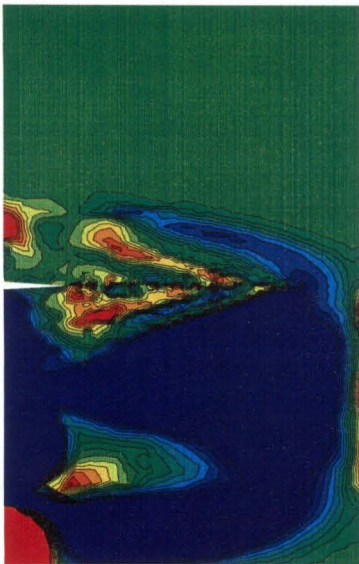
The numerical simulations have proven highly predictive of a number of observed features, including: the double shock wave structure, the large scale face contact behind the crack tip and the “hot spots” generated by frictional heating. These features follow naturally from a single description of the fracture properties of the material, supplied by the cohesive law, and are not built into the model. The fidelity of the model in reproducing very complex fracture events also gives a high reliability to the final sensitivity analysis, where the effects of several parameters have been investigated.

The accurate description of fracture processes by means of cohesive elements requires the resolution of the characteristic cohesive length of the material [26]. In some materials this length may be exceedingly small. Thus calculations based on cohesive elements inevitably have a *multiscale* character, in as much as the numerical model must resolve two disparate length scales commensurate with the macroscopic dimensions of the solid and the cohesive length of the material.



(a)

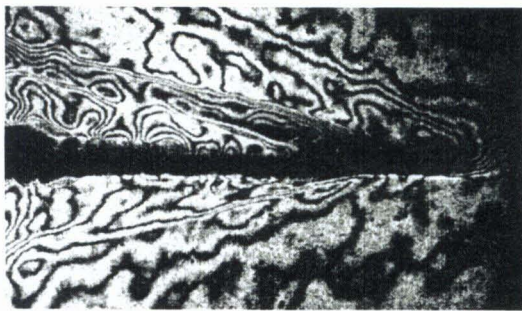
(c)



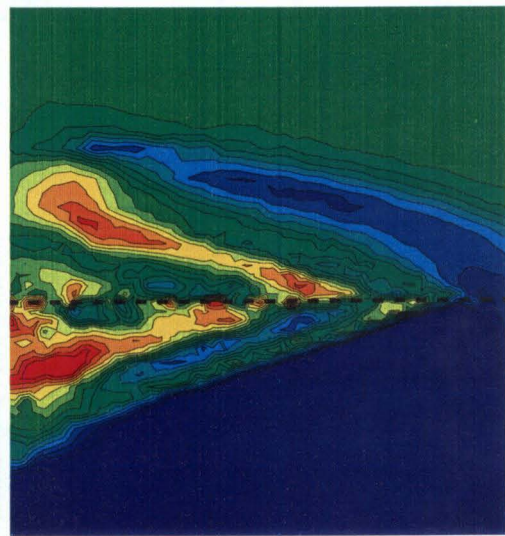
(d)

(e)

Figure 3.9: Contour levels of  $\sigma_{22}$  at times: (a) 10.8; (b) 14.4; (c) 18.6; (d) 22.2  $\mu\text{s}$ .



(a)



(b)

Figure 3.10: Comparison between the experimental and the numerical shock wave structure. The color scale in the numerical contour plot refers to the legend in Fig. 3.9.

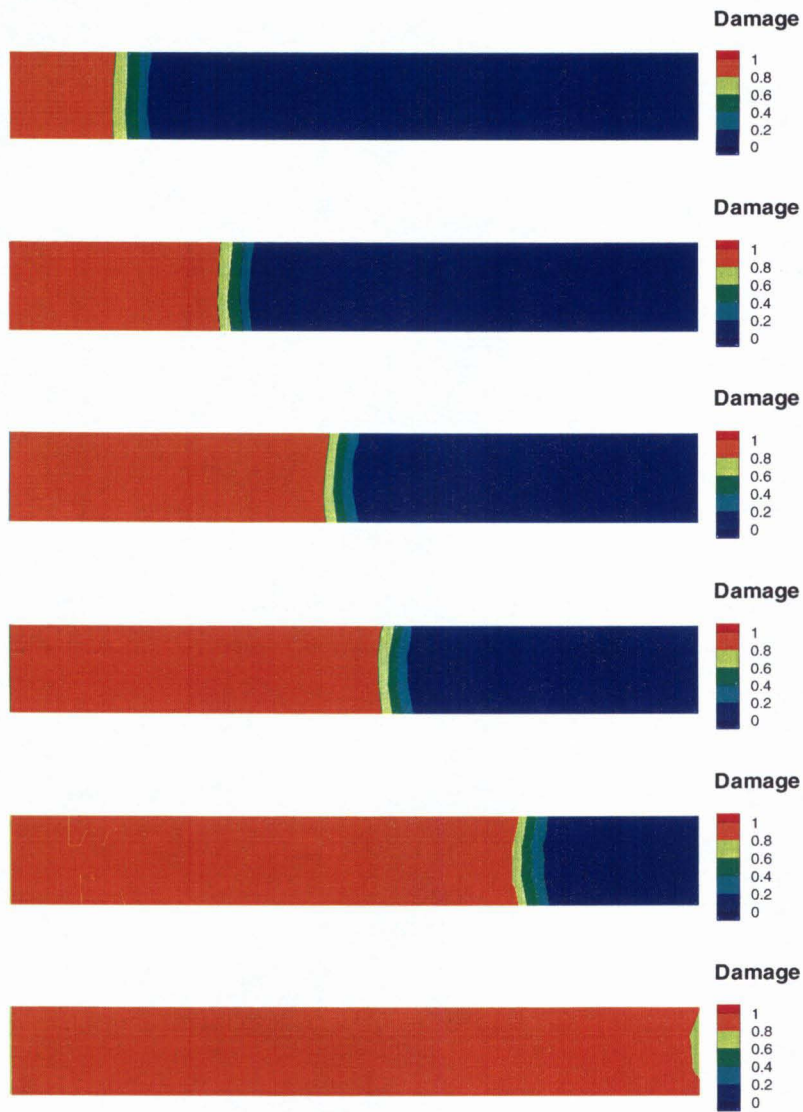


Figure 3.11: Contour levels of damage variable at time 9.6, 12, 13.2, 15.6, 18.6 and 22.2  $\mu s$ .

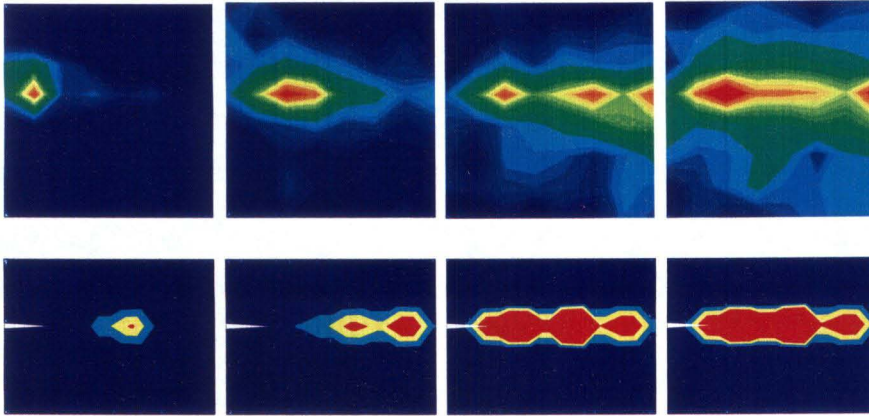


Figure 3.12: Comparison of experimental and numerical temperature values at time 40, 50, 60 and 70  $\mu$ s. See Fig. 3.13 for the temperature scale.

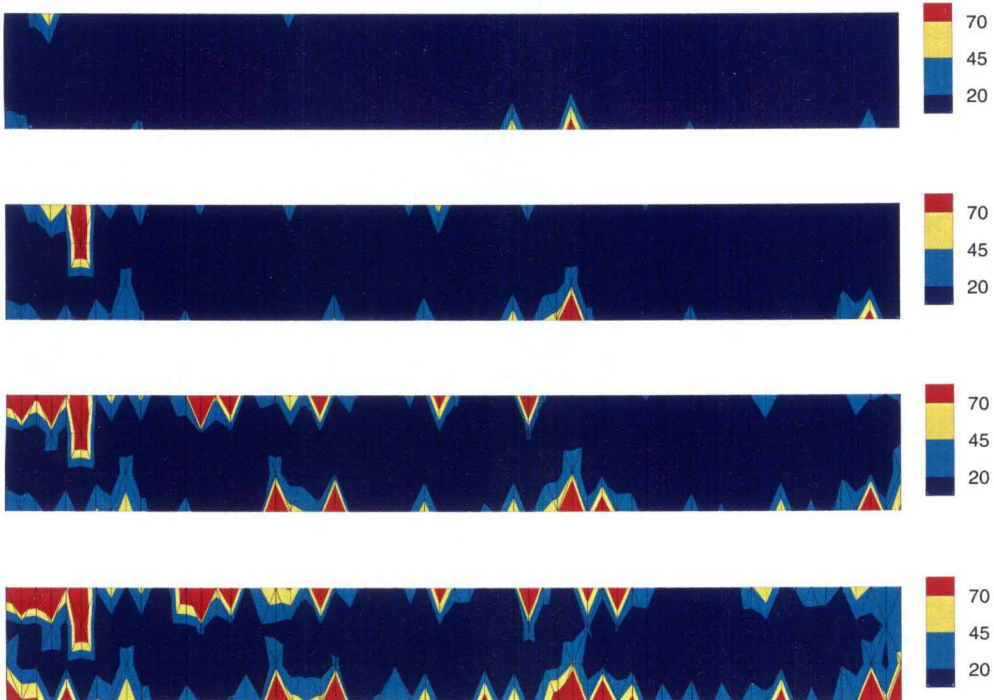
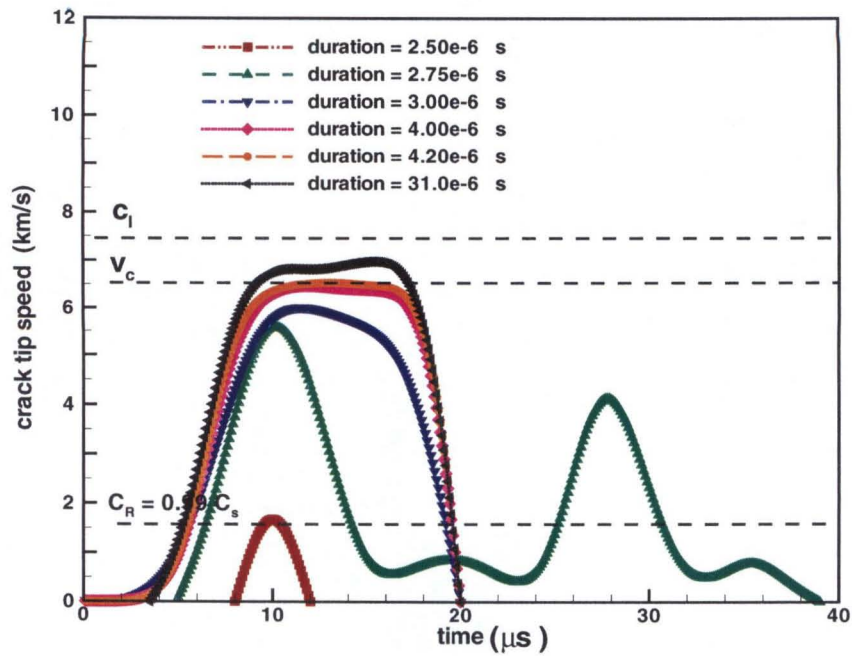
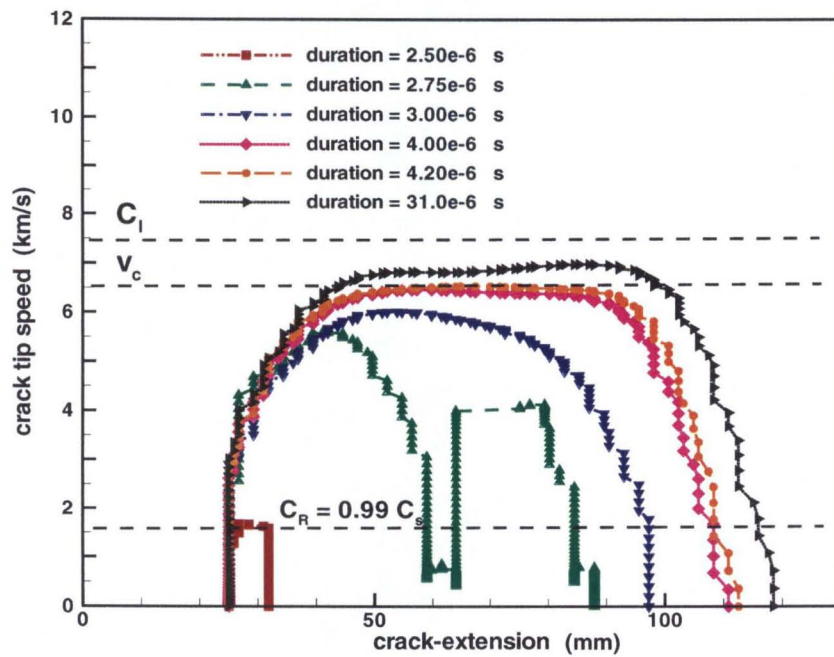


Figure 3.13: Temperature distribution across the crack surface at time 40, 50, 60 and 70  $\mu$ s.

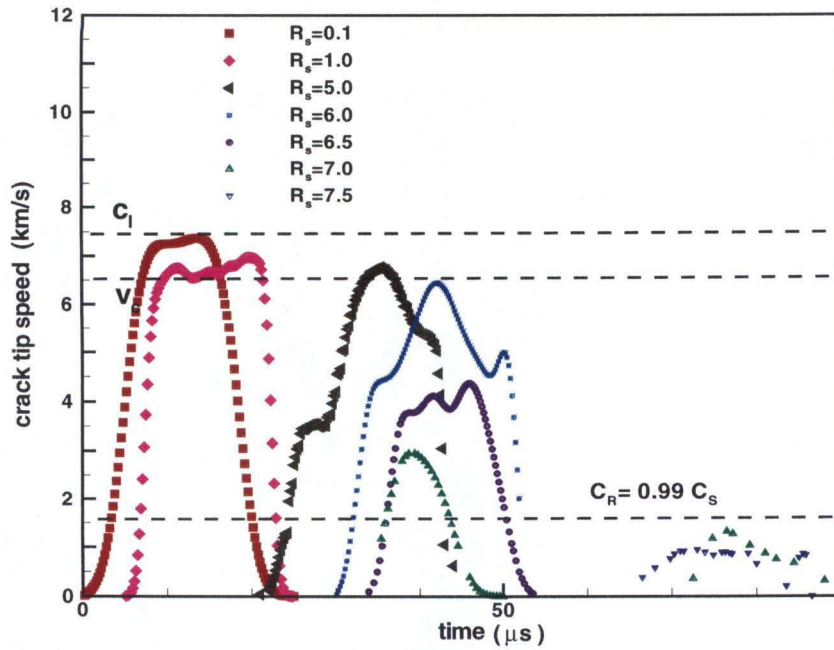


(a)

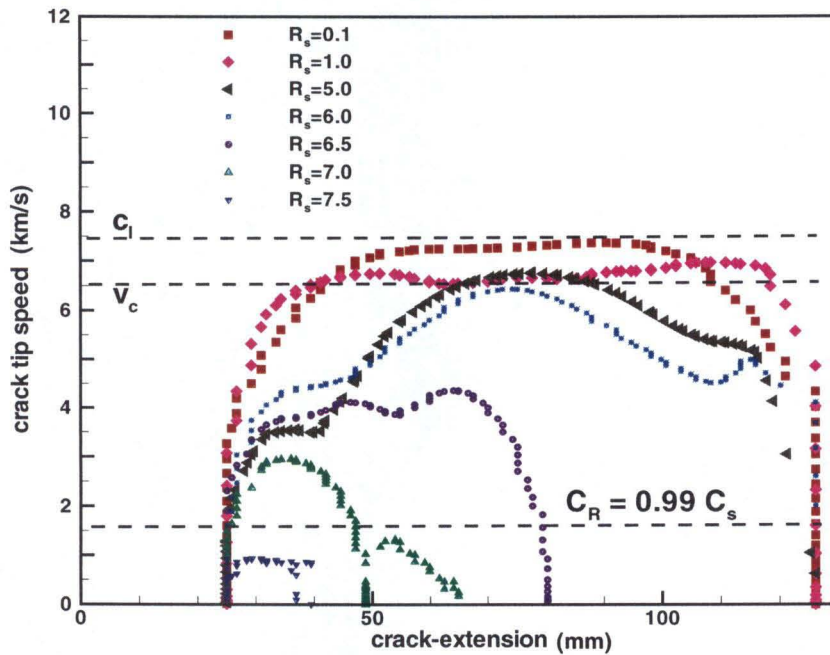


(b)

Figure 3.14: Crack speed history as a function of (a) time and location (b) at different impulse duration, the impact speed is 50 m/s.

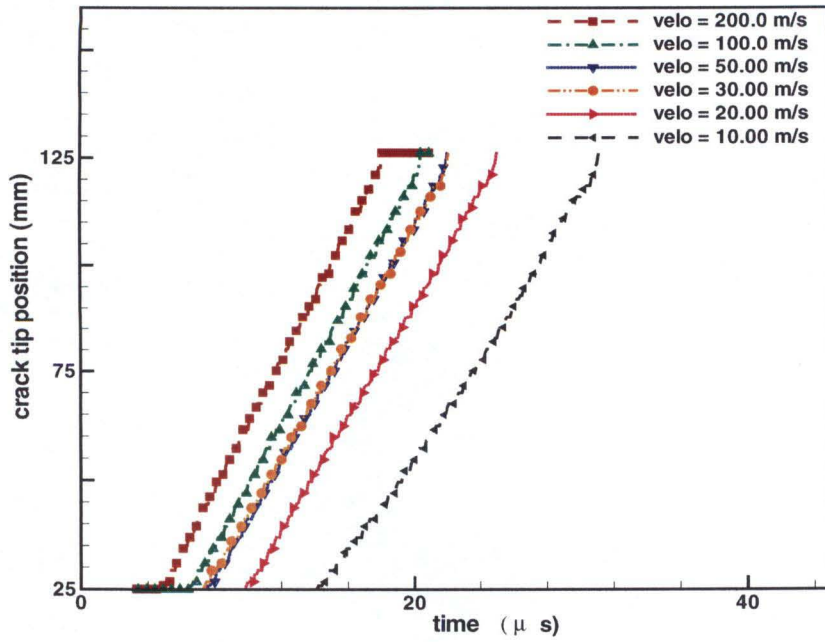


(a)

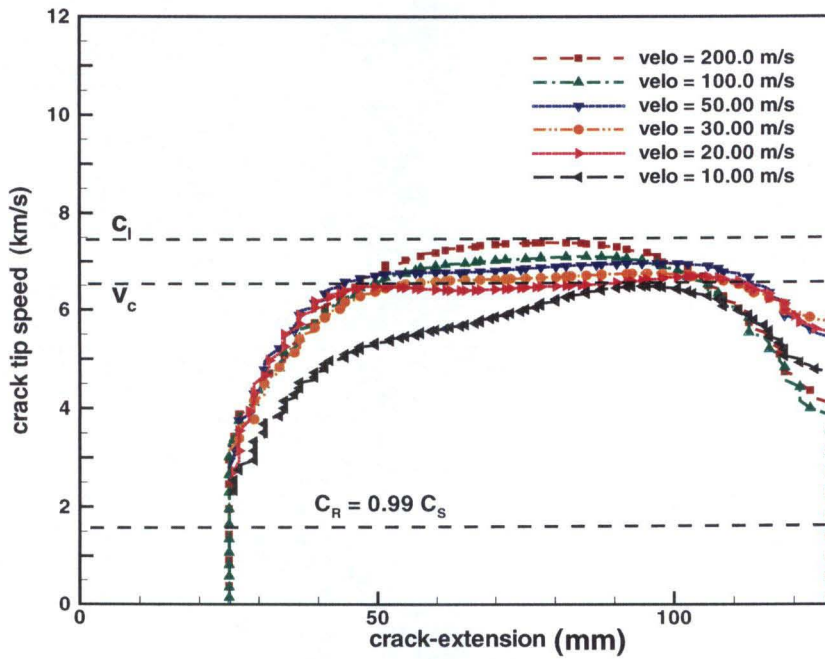


(b)

Figure 3.15: Crack speed history as a function of (a) time and (b) location at different relative cohesive strength  $R_s = \sigma_c / \sigma_{c0}$ , where  $R_s=1$  is corresponding to real experimental data  $\sigma_{c0} = 35.8$  MPa; impact speed  $v = 30$  m/s; impulse duration =  $31 \mu s$ .



(a)



(b)

Figure 3.16: Crack tip position (a) and crack speed history (b) at different impact speeds; cohesive strength:  $\sigma_c = 35.8$  MPa; impulse time =  $31 \mu s$ .

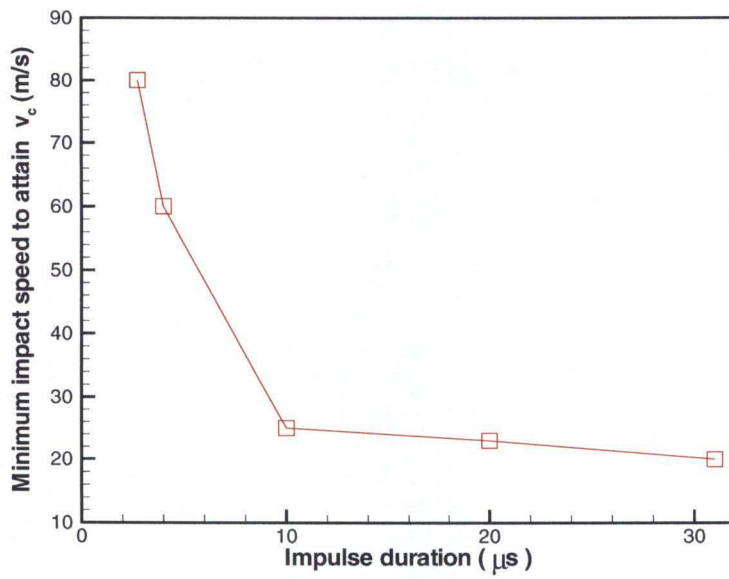


Figure 3.17: Minimum impact speed for the crack speed to achieve  $v_c$  at different impulse duration at the same cohesive strength:  $\sigma_c = 35.8 \text{ MPa}$ .

# Chapter 4 Failure mode selection of sandwich structures

## 4.1 Introduction

A typical sandwich structure is characterized by the presence of two high strength facings or panels separated by a low density material core. The sandwich structures have relative advantages over other structural materials in terms of improved stability, weight savings, crash worthiness and corrosion resistance. Therefore, the use of composite sandwich construction is rapidly increasing in current and planned future airframe design, especially for general aviation aircrafts and rotorcrafts, helicopter blades, optical benches for space applications and nonferrous ship hulls [129]. One of the shortcomings of sandwich structures is the still incomplete understanding of damage, as it can develop as consequence of low-velocity impacts (such as tool drops) or high-energy events (such as ballistic penetration) or an unusual level of the design loading. The damage characterization of sandwich structures is certainly more complicated than the one of conventional laminates. A first reason, related to their special structure, is that the damage often does not develop uniformly across the thickness. A second reason is that besides typical failure modes (such as penetration and delamination), also crushing and facetsheets debonding must be addressed. The shear load transfer through the core is often combined with unsymmetric damage, which requires a deep investigation in order to understand the damage progression and evaluate the residual strength.

A precise understanding of the real behavior in failure of sandwich structures *should* aid in establishing certification guidelines and confidence involving their damage tolerance, and also will improve the structural efficiency of aircraft. Moreover, the accurate assessment of damaged structures will reduce the frequency and cost of

repair thus improving the serviceability of the aircraft [4, 5, 6].

Motivated by those concerns, Xu and Rosakis [135] conducted a series of systematic experiments investigating the generation and subsequent evolution of dynamic failure modes in layered materials subjected to impact. High-speed photography and dynamic photo-elasticity were utilized to study the nature and sequence of failure modes. They found that in this loading condition, the dominant dynamic failure mode is the interlayer crack (delamination between panel and core), which is shear-driven and proceeds at intersonic speed. Very often, the intralayer cracks nucleate at the location of the local maximum shear stress. In order to pinpoint the shear-driven nature of the delamination avoiding free edges effects, longer specimens were also adopted.

## **4.2 Experimental set up**

### **Material description**

The sandwich specimen used in the experiments of Xu and Rosakis [135] is a thin plate obtained by bonding along their thickness two 4340-steel (external) plates to an Homalite (internal) plate. The interface bonding was Weldon-10. The geometry for two types of specimens is shown in Fig. 4.1. Both steel and Homalite are characterized by elastic material properties, reported in Table 4.1. The fracture parameters for the three materials are reported in Table 4.2.

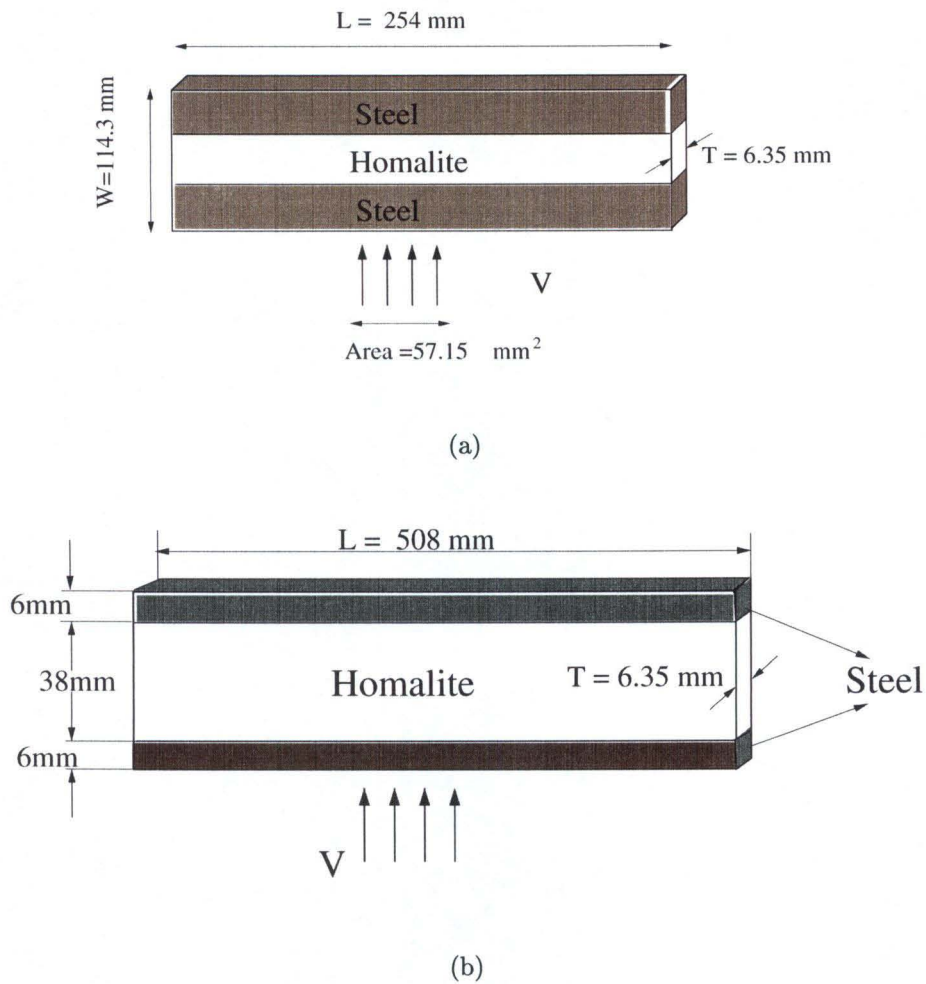


Figure 4.1: Geometry for: (a) Specimen A; (b) Specimen B.

## Experimental technique

The photo-elasticity technique records the maximum in-plane shear stress, so shear shock waves can be observed. A schematic setup of the photo-elasticity technique is given in Fig. 4.2. Two sheets of a circular polarizer were placed on both sides of the specimen. An Innova Sabre argon-ion pulsed laser served as the light source. The coherent, monochromatic, plane-polarized light output was collimated to a beam of

<i>Material</i>	Homalite 100	4340 Steel
<i>Strain rate</i>	10 <sup>3</sup>	/
<i>Young Modulus E (GPa)</i>	5.3	208
<i>Possion ratio ν</i>	0.35	0.3
<i>Material density ρ(kg/m<sup>3</sup>)</i>	1230	7830
<i>Longitudinal wave speed c<sub>d</sub>(m/s)</i>	2200	5500
<i>Shear wave speed c<sub>s</sub>(m/s)</i>	1255	3320
<i>Rayleigh wave speed c<sub>R</sub>(m/s)</i>	1185	2950

Table 4.1: Elastic material properties for 4340 Steel and Homalite 100.

<i>Material</i>	4340 Steel	Homalite 100	Weldon-10
<i>Maximum cohesive stresses σ<sub>c</sub> (MPa)</i>	1490	35	7.74
<i>Maximum shear stresses τ<sub>c</sub> (MPa)</i>	1053.6	40	14
<i>Critical opening displacement δ<sub>c</sub> (μ m)</i>	14.26	6.65	45.6
<i>Weighting coefficient β</i>	0.875	1.14	1.0
<i>Fracture energy G<sub>C</sub> (N/m)</i>	10620.0	88.1	176.6
<i>Characteristic length R (mm)</i>	14.26	2.77	18.05

Table 4.2: Fracture and cohesive parameters for 4340 Steel, Homalite 100 and Weldon-10 interface.

100 mm diameter. The laser beam was transmitted through the specimen, and the resulting fringe pattern was recorded by the high speed camera (Cordin model 330A rotating mirror type). During the impact test, the projectile was fired by a gas gun and hit the specimen on side the to trigger the recording system. Under dynamic deformation, the generation of isochromatic fringe patterns is governed by the stress optic law. For the case of monochromatic light, the condition for the formation of fringes can be expressed as:

$$\sigma_1 - \sigma_2 = \frac{N f_\sigma}{h} \quad (4.1)$$

where  $\sigma_1 - \sigma_2$  is the principal stress difference of the stress tensor averaged through the thickness;  $f_\sigma$  the material fringe value (23.7 KN/m for Homalite-100) or isochromatic fringe order;  $h$  is the half-thickness of the specimen. The isochromatic fringe patterns observed are proportional to the contours levels of the maximum shear stress, i. e.,  $\tau_{max} = (\sigma_1 - \sigma_2)/2$ .

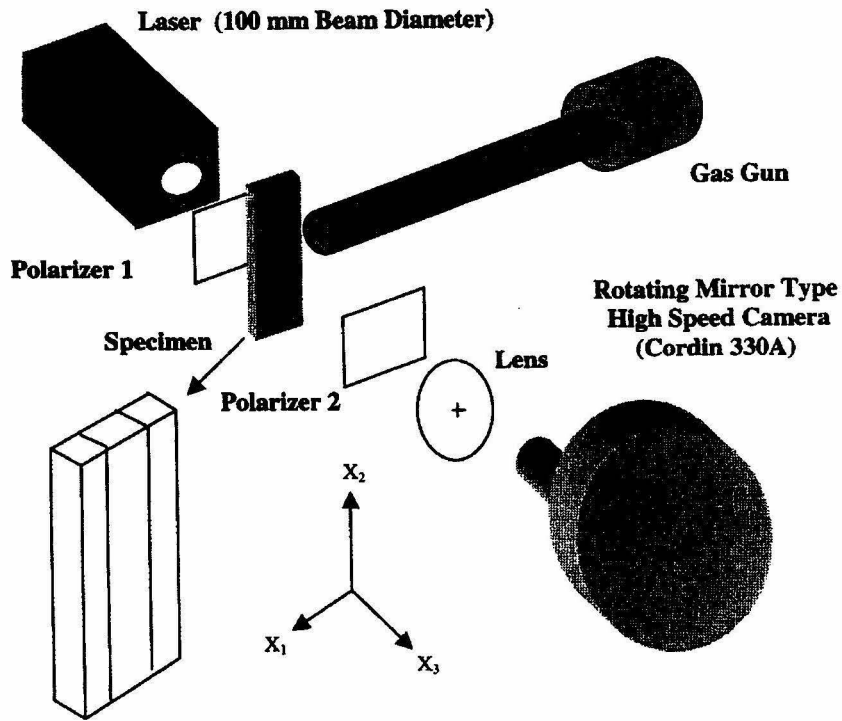


Figure 4.2: Schematic of the dynamic photo elasticity setup (Xu and Rosakis).

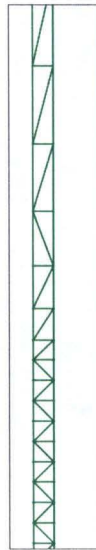
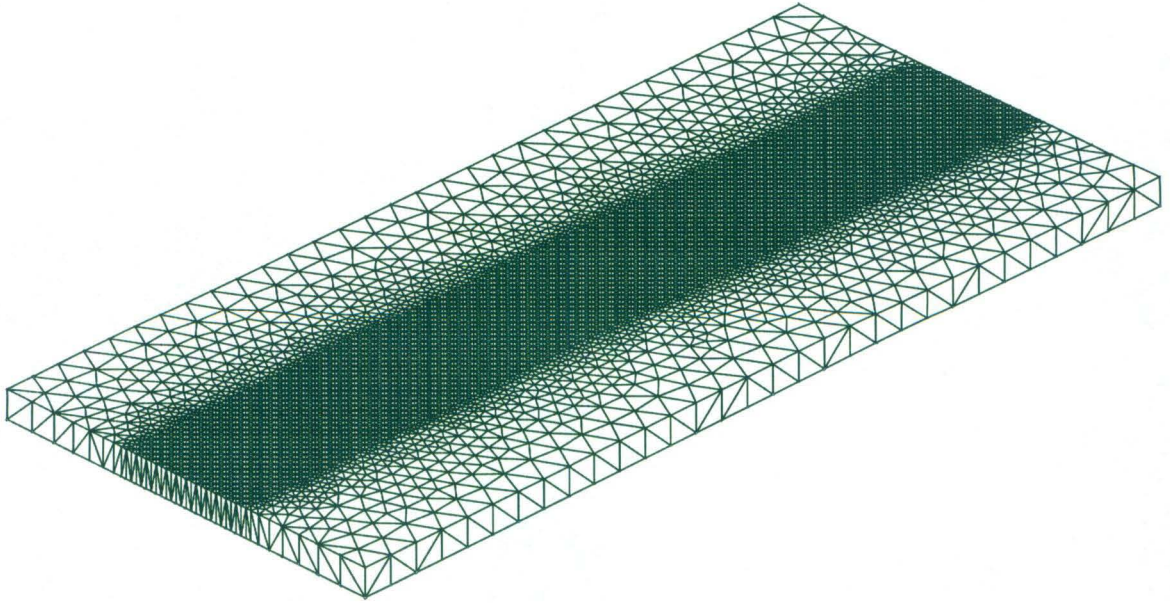
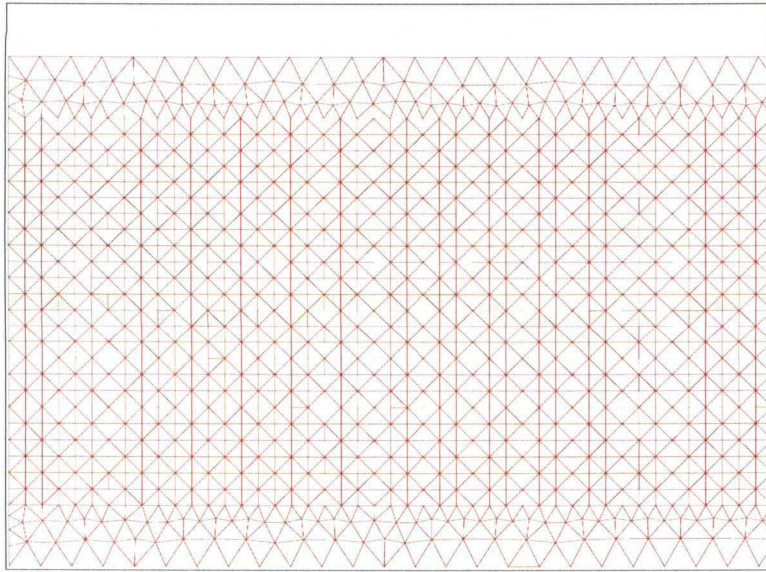


Figure 4.3: Computational mesh for specimen A, comprising 65365 nodes and 32482 10-node tetrahedra: (a) Upper view; (b) Side view.



(a)



(b)

Figure 4.4: Computational mesh for specimen B, comprising 113454 nodes and 56292 10-node tetrahedra: (a) Upper view; (b) Orthographic view.

## 4.3 Numerical simulations

### 4.3.1 Mesh description

In order to reduce the computational effort, without losing correspondence with the experimental situation, we modeled a slice of the specimen, 1.6 mm thick (1/4 of the real specimen thickness). The out of plane displacements along one surface of the plate are constrained to avoid buckling. The computational mesh comprises 65365 nodes and 32482 10-node quadratic tetrahedra, Fig. 4.3. The core is modeled using an uniform minimum mesh size of 0.79 mm; the mesh coarsens in the steel layer, in order to have one tetrahedral element in the thickness. The cohesive elements are adaptively inserted during the analysis, along previously coherent elements interfaces when the local stress attains a critical value. The effect of the bullet impact is approximated by prescribing a velocity profile to the nodes lying on the contact area. The load profile on the contact area and its time history are presented in Fig. 4.5. The velocity profile is parabolic, with a width of 16.4 mm centered at bottom edge of the specimen. The impulse duration  $t_p$  is 18.4  $\mu\text{s}$ ; both the rise time  $t_r$  and the step down time  $t_d$  are 1.8  $\mu\text{s}$ ; the impact speed assumed in the calculation is 32.4 m/s. The analysis has been conducted up to 300  $\mu\text{s}$  after impact.

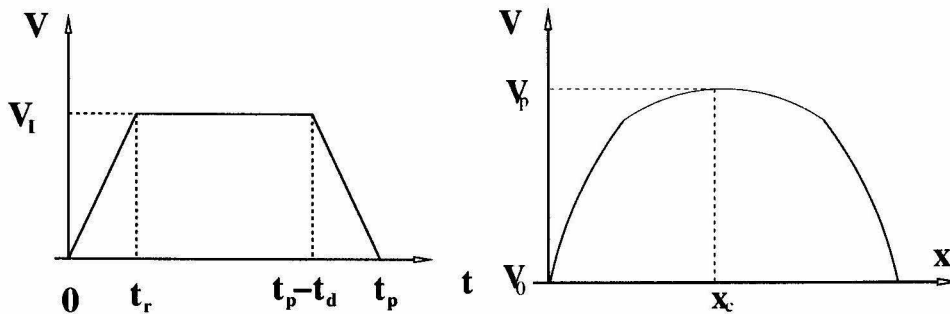
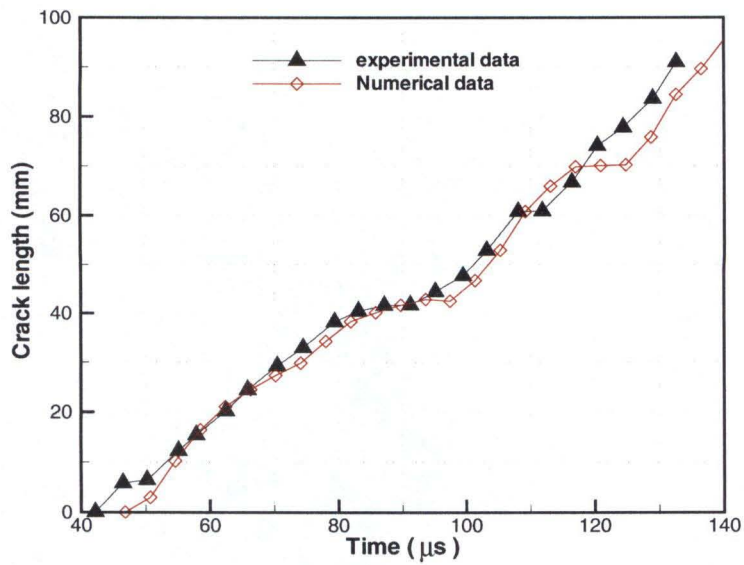
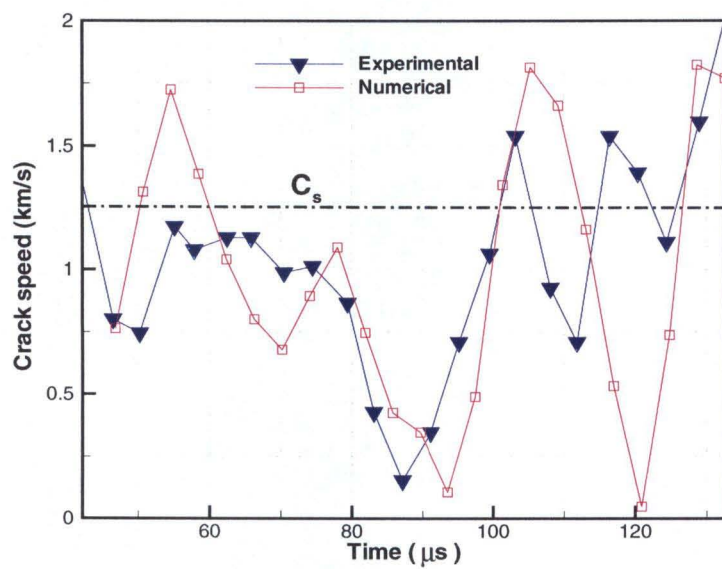


Figure 4.5: Impact velocity profile with respect to time (a) and position (b) rising time and stepping down time  $t_r$  and  $t_d$  are 1.8  $\mu\text{s}$ ; the impulse time  $t_p$  is 18.3  $\mu\text{s}$ .



(a)



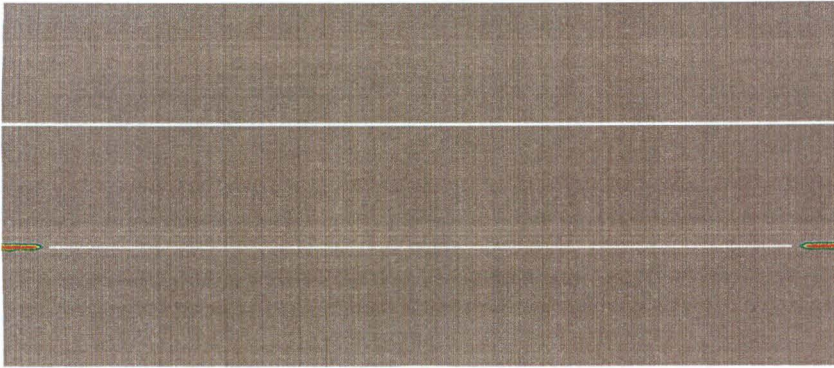
(b)

Figure 4.6: Crack tip position (a) and crack speed (b) history of the lower interface. Comparison between experimental and numerical results.

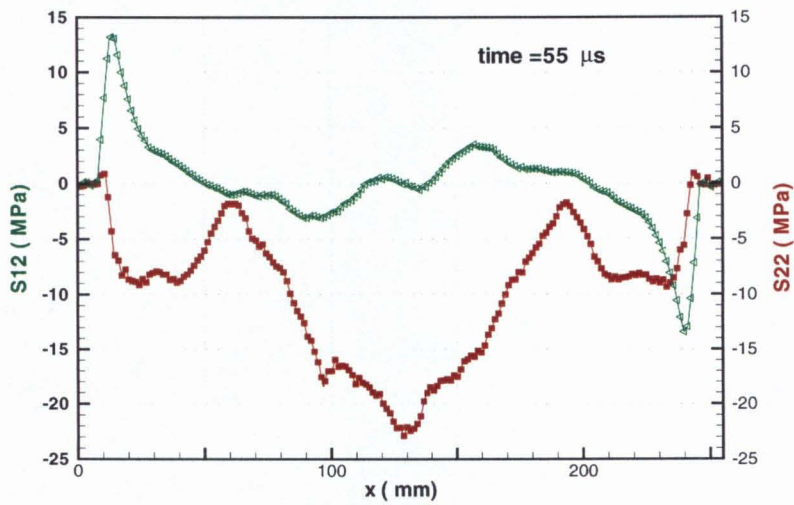
### 4.3.2 Results and discussion

After the impact, the stress wave propagates from the center of the specimen towards the edges. The wave reaches the corner  $50 \mu\text{s}$  after the impact. At this time the interfacial cracks start from both the ends of the bottom interface and propagate towards the center. The two traveling cracks meet at time  $140 \mu\text{s}$  after the impact. Afterwards, the Rayleigh wave starts from the center of the specimen and propagates towards the edges. Meanwhile, interfacial cracks start from the center of upper interface and interact with the Rayleigh wave later on. As a result the crack kinks into the core layer, clearly forming several branches. Fig. 4.6 shows the history of the crack tip position and of its velocity, comparing numerical and experimental results, which have a noteworthy match. It bears emphasis that the crack speed along the lower interface reaches the Rayleigh wave speed soon after initiation, and drops to a very low value around  $90 \mu\text{s}$  after impact; next, it increases again dramatically up to the shear wave speed of Homalite-100. This behavior is very consistent with what was observed during the experiments, see Fig. 4.6.

The analysis of the stress distribution along the interfaces clearly shows that the delamination is shear-driven. Fig. 4.7a shows the profile of the stress components  $\sigma_{12}$  (green triangles) and  $\sigma_{22}$  (red squares) along the interface at time  $55 \mu\text{s}$  after impact. Fig. 4.7b shows the damage distribution at the same time. The interface crack along the bottom interface has just started, and the stress state is still compressive, but the shear stress  $\sigma_{12}$  attains the maximum absolute values at those two locations.



(a)



(b)

Figure 4.7: Specimen A, time  $55 \mu\text{s}$  after the impact: (a) Damage pattern; (b)  $\sigma_{12}$  and  $\sigma_{22}$  stress components distribution.



(a)



(b)

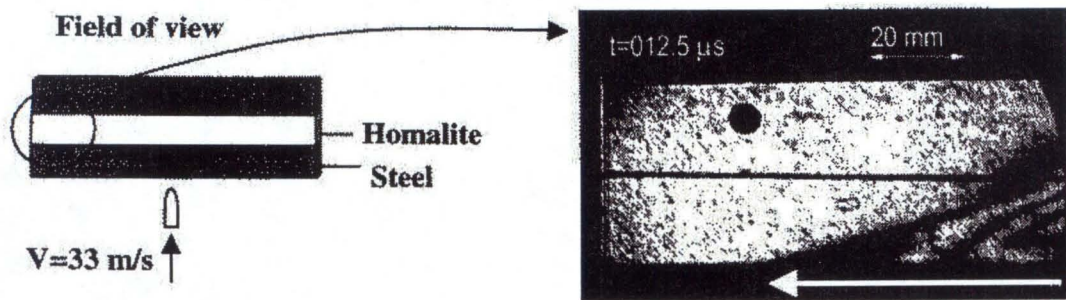
Figure 4.8: Specimen B: branch pattern of the core material (Homalite-100) at (a) 60; and (b) 100  $\mu s$  after impact.

In a further simulation carried out with specimen B (see Fig. 4.8), the branch starts from the middle of the bottom interface instead of near the free edges; and propagates toward the center as well as two free edges, this confirmed that the fracture propagates indeed in shear-mode. It is also interesting to see the buckling of the compressed steel layer in the long specimen simulation.

An important observation is that the branches sprout from the bottom interface are in the beginning parallel to each other, with a branching angle around 45-60 degrees; later on, when those branches get close to the top interface, they start to kink and try to propagate parallel to the debonded top interface. This confirms that near an interface, the maximum hoop stress acts parallel to that interface.

Fig. 4.9 shows the contour levels of the maximum shear stress  $\tau_{max}$  at different times of the analysis, compared with the experimental fringes at the same time and from the same observing window, shown in Fig. 4.9a. Similar patterns between the experimental photoelastic fringes and the contour plots of the maximum shear stress are observed. The right part of Fig. 4.9a shows a surface wave entering the field of view at time 12.5  $\mu s$  after impact, the arrow indicating the direction of the wave propagation. Fig. 4.9b,c show a comparison between numerical and experimental

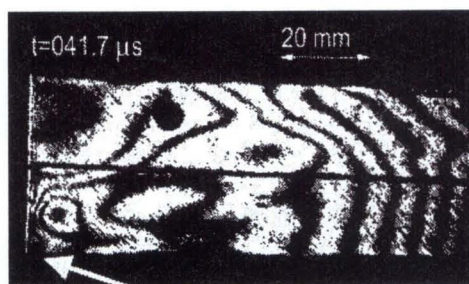
contour plots of  $\tau_{max}$  at 47.2  $\mu s$ , when the wave has reached the free edge and initiated a shear interfacial crack there. Fig. 4.9d-e, shows the contour levels at time 79.2  $\mu s$ , when the crack propagates toward the specimen center. Both the concentration of the photoelastic fringes and the maximum shear stress contour lines indicate that the crack propagates at an intersonic speed relative to the core material.



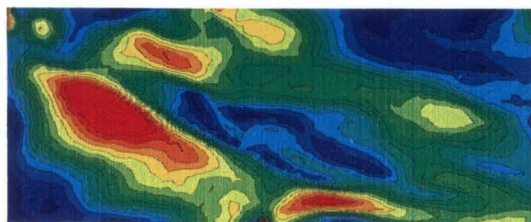
(a)



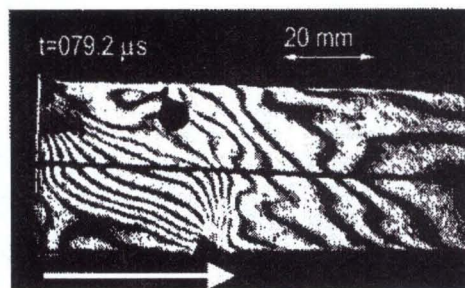
(b)



(c)



(d)



(e)

Figure 4.9: Specimen A: (a) the observing window and the experimental fringes at time  $12.5 \mu\text{s}$  after impact. (b) and (d) are contour levels of  $\tau_{max}$  at times 41.7, 79.2  $\mu\text{s}$ ; (c) and (e) are experimental fringes at time 41.7 and 79.2  $\mu\text{s}$ .

## 4.4 Parametric studies

### The effect of contact area (bullet diameter)

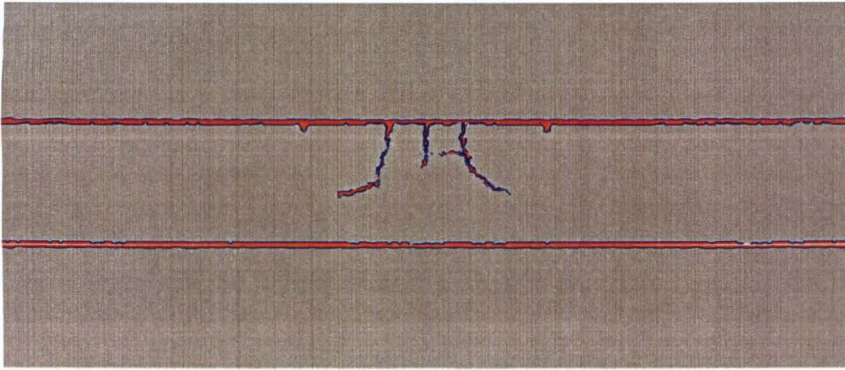
In numerical simulation, the effects of a change in the impact area are obtained through changing the size of the zone where the velocity profile is imposed (along the external edge) 4.10. The comparison has been conducted by keeping a fixed speed, therefore the amount of energy supplied to the specimen increases with the increase of the impact area. As expected, the main effect of enlarging the contact area is to move the location of the crack patterns closer to the edges. The distribution of damage is highly affected by the size of the impactor.

### The effect of core material fracture energy

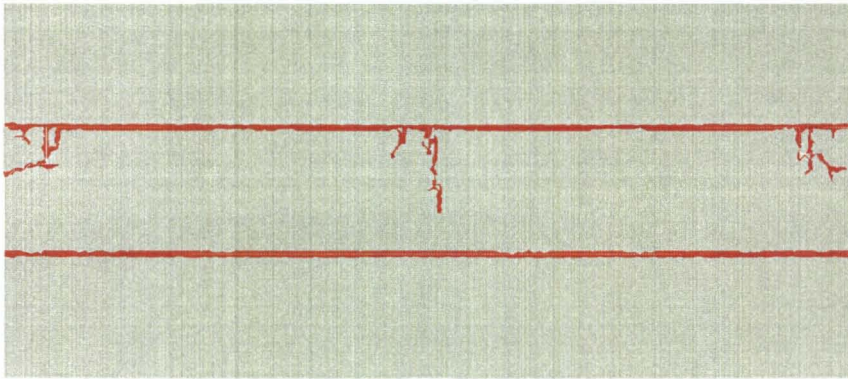
A second investigation is concerning the effect of the fracture energy of the core material. Fig. 4.11 shows that the fracture energy  $G_c$  plays an important role for the damage of the sandwich structure. When  $G_c$  is high, the damage concentrates in the central area of the upper interface, near the impact point, and the so-formed structure still has some residual strength. In contrast, when  $G_c$  is lower, the damage is more severe, involving a more extended zone, and may reduce the residual damage tolerance to zero. An interesting observation is related to the fact that the main crack patterns remain similar, whenever the impact speed and impact area are kept fixed.

### The effect of interface weighting parameter $\beta$

The effect of the interface cohesive weighting coefficient parameter  $\beta$  is shown in Fig. 4.12. It can be noticed that for very small values of  $\beta$ , the branching within the core layer can be completely avoided, and only interface delamination can be observed. This reflects the fact that for a large  $\beta$ , the critical condition for the initiation of a cohesive crack is ostensibly independent of the magnitude of the shear tractions, and the ensuing sliding displacements are constrained to remain close to zero at all times.

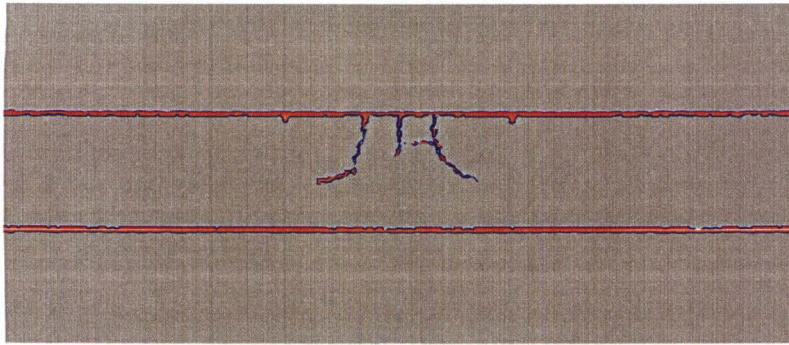


(a)

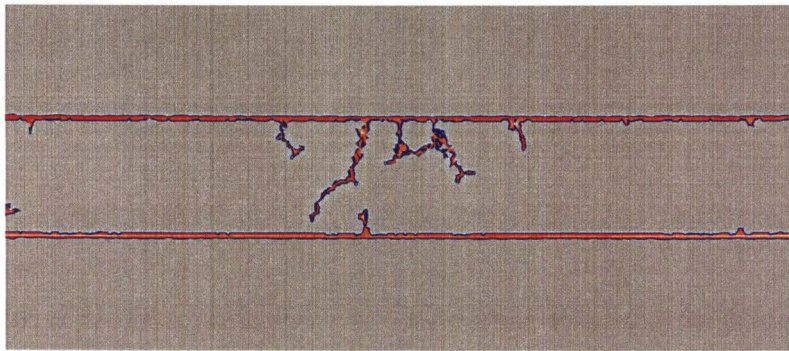


(b)

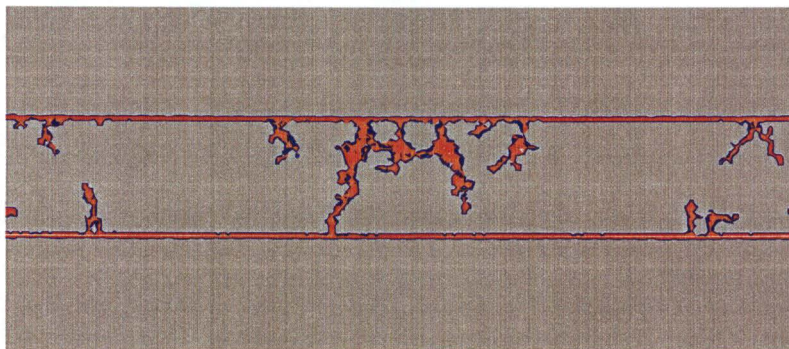
Figure 4.10: Crack patterns at  $300 \mu\text{s}$  after impact, impact speed  $32 \text{ m/s}$ , for different contact area: (a)  $15 \text{ mm}^2$ ; (b)  $90 \text{ mm}^2$ .



(a)

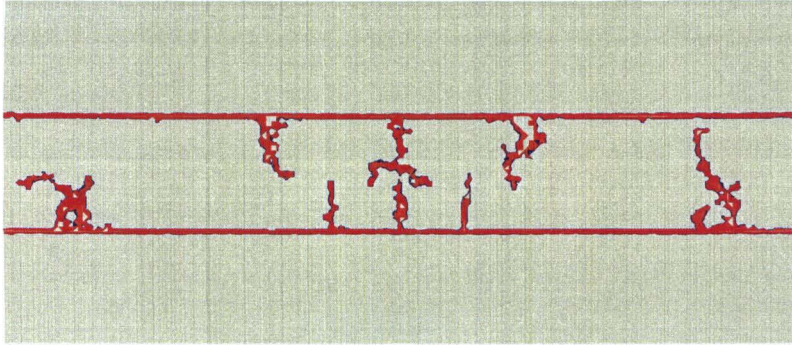


(b)

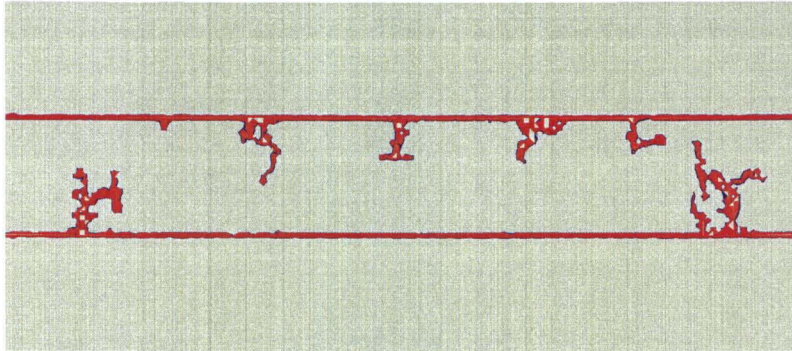


(c)

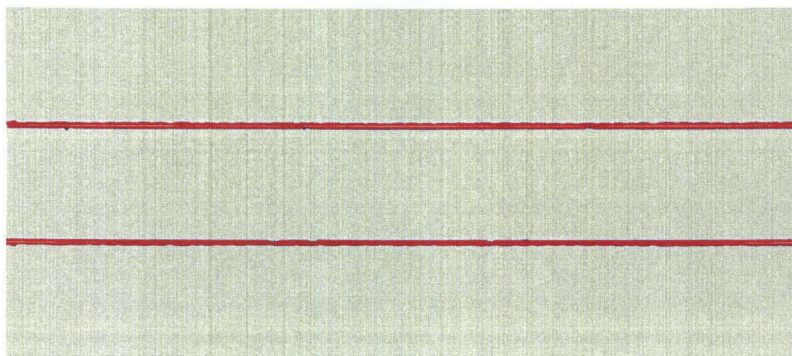
Figure 4.11: Crack patterns for different Homalite fracture energy  $G_c$ : (a) 359 N/m; (b) 176 N/m; (c) 88 N/m (impact speed 32 m/s, contact area 57 mm<sup>2</sup>, 300  $\mu$ s after impact).



(a)



(b)



(c)

Figure 4.12: Crack patterns for different cohesive weight coefficients of the interface (a)  $\beta=10$ ; (b)  $\beta=2.5$ ; (c)  $\beta =0.32$ . (impact speed 32 m/s, contact area 57 mm<sup>2</sup>, 300  $\mu$ s after impact,  $G_c = 88$  N/m)

## 4.5 Summary

Our simulation captures qualitatively the main experimental observations. The most relevant correspondence is in the development of the first crack at the interface between the layers, the presence of shear stresses along the interface, which renders the crack shear driven and often intersonic, and the transition between interlayer crack growth and intralayer crack branching. The effects of the bullet diameter (impact area), the core material fracture energy, as well as the cohesive weighting coefficient  $\beta$  have been investigated. All the results confirm the feasibility of the cohesive theories.

# Chapter 5 Dynamic crack branching

## 5.1 Introduction

During the last decade, Fineberg and Sharon have conducted a series of well controlled experiments of crack propagation in PMMA (polymethyl methacrylate) and in soda lime glass, and have raised considerable interest in the development of fracture in highly brittle materials [43, 44, 51, 118, 21, 20, 19]. Fineberg and Sharon pointed out several “universal” features of micro-branching instability in dynamic fracture, such as the existence of a critical velocity for the onset of micro-branching, the shape and the growth pattern of micro-branches and their relation to specimen surface roughness and the effects of the 3D-to-2D transition. Fineberg and Sharon showed experimental evidence that the crack dynamics change dramatically when the speed of the advancing crack exceeds a critical velocity  $v_c$ , which they demonstrated to be  $0.36 V_R$  (Rayleigh wave speed of the material). For speeds higher than  $v_c$ , the crack locally changes its topology and sprouts small, microscopic, short-lived side branches. Furthermore, at the onset of this instability, the mean acceleration of the crack suddenly drops and the crack velocity starts to oscillate, provoking a correlated oscillation on the fracture surface [43, 51].

The instability mechanism for a moving crack manifests itself as a local crack branching, where both the mean crack velocity and the average crack length are strictly determined by the amount of energy flowing into the crack tip. A larger energy supply results in a higher mean velocity and in a longer branch length.

Branching instability is the main mechanism for energy dissipation by a moving crack in brittle, amorphous material. Beyond the onset of instability, any amount of energy supplied to the crack which exceeds the amount requested for the smooth crack propagation is not used to increase the crack tip speed, but in creating new surfaces. It has been observed that the fracture surfaces created by micro-branches are

nearly an order of magnitude larger than those of smooth cracks, therefore absorbing a larger amount of energy. This observation explains why the theoretical limiting velocity cannot be experimental realized, i. e., other than accelerating, a crack will prefer to dissipate energy by creating new surfaces via multiple parallel cracks [114].

As a further observation, the branch length and the distance between branches are well-modeled by a log-normal distribution. This may somehow explain that the observed log-normal distribution in the fragment size of a brittle object fractured at high energy is dynamical by its nature, and is not necessarily the result of a cascade of fractures at different scales.

Taguchi [124] also studied the non-branching to branching morphological transition for a tearing (hot) elastic plate and a quenching (cold) glass plate. In his experiments, he observed that when the temperature between the hot plate and the cool plate increases, the shape of the cracks changes from straight to branching patterns.

There have been several approaches to investigate the crack branching or crack propagation instability. The main features of the instability have also been noticed in the modes of ideal crystals [78, 77], molecular dynamics [1, 2, 141] and finite-element simulations [65, 137] of dynamic fracture.

Langer's phenomenological model equations [69, 113] yield in 1D oscillations of the crack tip velocity about a critical speed. Without distinguishing branching and dislocation emission, Marder and Liu [78, 77] modeled the elastic medium as a 2D lattice of coupled springs. Allowing a spring to be elastic until a critical displacement at which time they snap, and introducing a small viscous term, they could reproduce the Yoffe instability [140]. They found periodic occurrence of local branching events, where the main crack sprouts side branches that propagate for a short distance and die. The spacing between the frustrated branches is a function of the amount of dissipation [78].

Several attempts in Molecular Dynamics (MD) have also been performed by Gao, Abraham and Zhou [1, 3, 141, 52], to investigate the crack branching. The earliest MD simulations of fracture were carried out by Ashurst and Hoover [9] in the

1980s. Gumbsch *et al.* [52] showed that crack branching is closely tied to dislocation nucleation and emission. They observed that: the driving force for dislocation nucleation in a crystal increases with increasing speed; dislocation nucleation and mobility determine the initial crack branching path and the branching angle; dislocation emission and crack propagation repeats until branching finally occurs; cracks release the surplus of mechanical energy by emitting strong acoustic waves at the breaking of every atomic bond, which are caused by the nonlinearity in the interatomic interaction; reaching the terminal crack velocity is not sufficient to cause crack branching; branching occurs not right at the maximum velocity but after has passed it and has propagated for a while. From all those observations, Gumbsch *et al.* therefore claimed that the energy associated with the dynamic crack rather than crack-tip velocity would provide a good criterion for describing the crack branching instability. Zhou *et al.* [141] also found that instead of the crack-tip velocity, the gradual accumulation of energy around the dynamic crack tip is an essential feature for the ultimate emission of dislocations and development of crack branching.

Fineberg and Sharon ([118, 43, 44] and Zhou [141] concluded that changing the loading rate (or the Morse potential parameter in Zhou's case) dramatically changes the branching pattern; once the crack branches and grows a short distance, instability gradually alters their path so that the average paths have small angles with respect to the original straight crack path.

This result is also in agreement with the numerical observations of Martin *et al.* [80]. They applied a finite difference scheme to a discrete lattice model from the continuum equations of elasticity that respects the properties of isotropy and linear elasticity at large length scales and simulated the crack propagation under Mode I loading. The simulations of Martin *et al.* showed that when the crack reaches a critical velocity, it branches into two macroscopic running cracks, and that the lattice has a strong symmetric influence on the stress field near the crack tip. The stress field near the tip of the crack "alternates" between two almost "mirror" configurations as the crack snaps bonds of different orientations as it proceeds.

In this chapter, we apply the cohesive theories of fracture to the simulation of

crack branching in a PMMA thin plate, in the configuration tested by Sharon and Fineberg [118, 43, 44]. We are interested in reproducing the main features of their experiments, such as branch angles and branch patterns, which have a very good agreement with the MD simulations of Zhou [141].

## Confirmation of continuum theory

Sharon and Fineberg [117] experiments confirmed the continuum theory of dynamic brittle fracture for fast cracks by pointing out that when a spontaneously forming crack front reaches propagation speeds greater than the critical speed,  $v_c$ , it can no longer be considered as a single crack. The continuum theory derived by Eshelby, Kostrov and Freund [47] is based on the fact that, in an elastic material, the tip of a moving crack is the only energy sink for the elastic energy that is released from the surrounding material as fracture occurs. Linear elasticity theory predicts that the stress field is dominated by a square-root singularity in the close vicinity of the tip.

The continuum theory makes use of the universal nature of the near-tip field by computing the energy flux through a loop surrounding the tip and entirely enclosed within the “singular zone” (the region dominated by the singular stress field). When the external stresses driving the crack are independent of the time and can be mapped to stresses directly applied to the crack surfaces, the equation for the energy balance at the crack tip is predicted to have the following form:

$$\Gamma = G(l)A(v) \approx G(l)\left(1 - \frac{v}{V_R}\right) \quad (5.1)$$

where  $l$  is the instantaneous crack length,  $A(v)$  is a universal function of  $v$  and  $G(l)$  is the amount of energy per unit area present at the tip of a static crack of length  $l$  and contains all the effects of applied stresses and specimen geometry. Inverting equation (5.1) we obtain the equation of motion for a moving crack:

$$v(l) = V_R \left(1 - \frac{\Gamma}{G(l)}\right) \quad (5.2)$$

Since  $G(l)$  can be arbitrarily large, equation (5.2) predicts that  $V_R$  is the limiting speed of a moving crack. However, it needs to be pointed out that equation (5.2) is of first order in time, and therefore describes a “massless crack” (no inertial terms); all of the dissipative processes dependence on the material, and possible dependence on velocity, should be included in  $\Gamma$ . Equation (5.2) can be considered valid as long as all the dissipative processes are enclosed within the singular zone.

Below the limiting speed  $v_c$ , the single-crack condition is met, and equation (5.2) describes the mean velocity of a multi-crack-state. In contrast, when the crack velocity exceeds  $v_c$ , the largest micro-branches gradually extend beyond the singular zone, and the conditions for the validity of equation (5.2) do not hold anymore. This explains the apparent discrepancies between experimental measurements and continuum predictions [114, 101, 102].

## 5.2 Model Description

The original experiments of Sharon and Fineberg [43, 44, 118] were conducted on thin, quasi-2D sheets of brittle, cast PMMA with a thickness of either 0.8 mm or 3 mm, 50-200 mm and 200-400 mm in the vertical (defined as  $y$ ) and the horizontal (defined as  $x$ ) direction respectively. We reproduce here the simulations in PMMA and apply the same analysis to Homalite-100 specimens.

To reduce the numerical effort, we resize the computational model into a square plate of dimension  $l \times l \times t = 3 \text{ mm} \times 3 \text{ mm} \times 0.03 \text{ mm}$ , with a pre-crack of 0.25 mm along the horizontal symmetry axis  $x$  (Fig. 5.1). The initial velocity is imposed in the  $y$  direction everywhere in the model is  $v_{y0}(y) = \gamma y$ , where  $\gamma$  is an initial strain rate. Along the two edges parallel to the  $x$  axis, a uniform and constant velocity  $v_y^\pm = \gamma l/2$  is imposed during the analysis, which lasts up to 5  $\mu\text{s}$ .

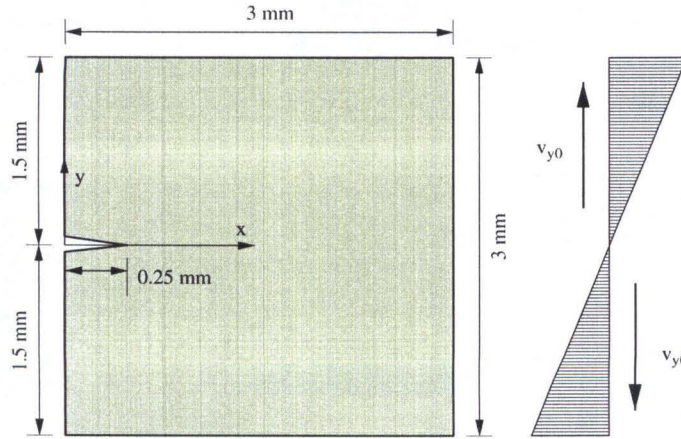


Figure 5.1: Geometry of the plate and initial velocity field  $v_{y0}$  in  $y$  direction.

In order to resolve the cohesive zone and avoid spurious mesh size effects, along the expected crack path the element size has to be smaller than the characteristic size  $R$ . The size  $R$ , defined through equation (2.18), is  $19.5 \mu\text{m}$  for PMMA,  $682 \mu\text{m}$  for Homalite-100.

We carry out our analysis using the mesh labeled F (Fig. 5.2), which initially consists of 36769 nodes and 18162 10-nodes quadratic tetrahedra. The minimum mesh size is  $20 \mu\text{m}$  and is designed so that it is finer along the main crack trajectory, and coarsen away to the edges. The cohesive elements are inserted later on with the already mentioned self-adaptive procedure. The elastic material properties for PMMA and Homalite-100 are collected in Table 5.1; the fracture properties are collected in Table 5.2.

<i>Material</i>		PMMA	Homalite-100
<i>Youngs Modulus (GPa)</i>	$E$	3.24	5.3
<i>Possions' ratio</i>	$\nu$	0.35	0.35
<i>Material density (kg/m<sup>3</sup>)</i>	$\rho$	1190	1230
<i>Longitudinal wave speed (m/s)</i>	$c_d$	2760 [44]	2200
<i>Shear wave speed (m/s)</i>	$c_s$		1255
<i>Rayleigh wave speed (m/s)</i>	$c_R$	926	1185

Table 5.1: Mechanical parameters for PMMA and Homalite-100.

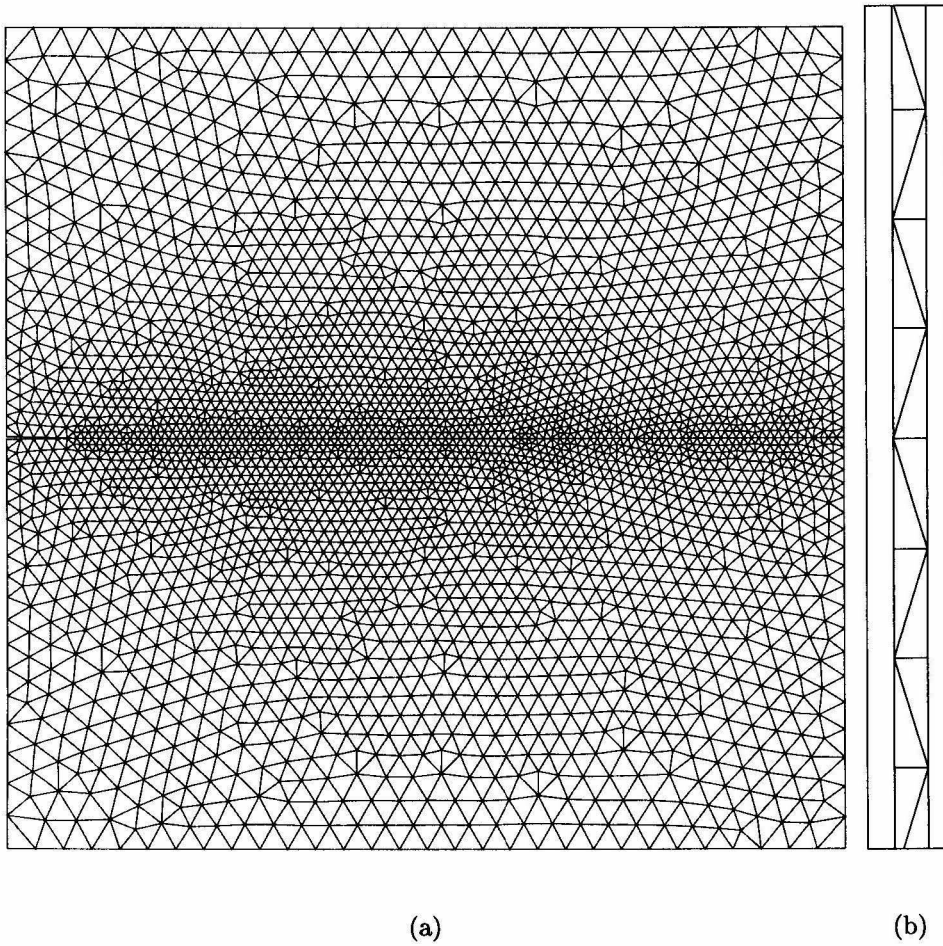


Figure 5.2: Computational mesh F, comprising 36769 nodes and 18162 10-nodes tetrahedra, minimum mesh size  $20 \mu\text{m}$ : (a) Upper view; (b) lateral view.

<i>Material</i>		PMMA	Homalite-100
<i>Fracture energy (N/m)</i>	$G_{Ic}$	352.35	81
<i>Maximum cohesive stresses(MPa)</i>	$\sigma_c$	324	35
<i>Critical opening displacement(<math>\mu\text{m}</math>)</i>	$\delta_c$	2.175	6.65
<i>Weighting coefficient</i>	$\beta^2$	5.4365	1.306

Table 5.2: Fracture parameters for PMMA and Homalite-100.

### 5.3 Results and Discussion

An efficient way to visualize the crack propagation and the formation and distribution of branches is to plot the contour levels of the damage variable previously introduced, see section 3.3. For a low loading rate of  $500 \text{ s}^{-1}$ , a single, smooth, straight crack is formed behind the wake (see Fig. 5.3).

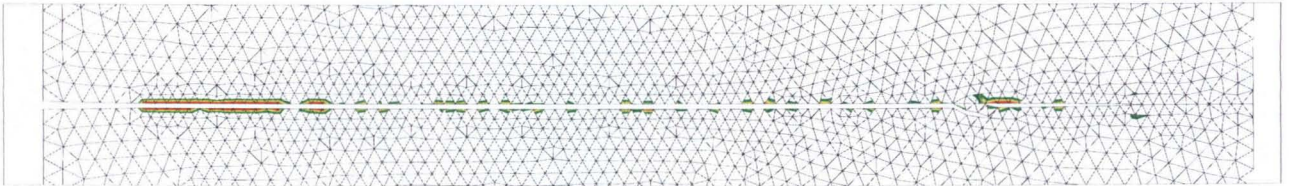


Figure 5.3: PMMA specimen at loading rate  $500 \text{ s}^{-1}$ : single crack propagation.

When the loading rate is increased up to  $1000 \text{ s}^{-1}$ , the crack develops in a smooth, straight path only at the early stages of its propagation (see Fig. 5.4 a-d). Later on, the main crack attempts to branch out (Fig. 5.4 e, f), but most of the side branches only live up to one element and die. Only one side branch propagates parallel to the main crack for about a short time interval ( $0.3 \mu\text{s}$ ) and furthermore it merges into the main crack. The main crack continues to grow as a single crack for about  $0.5 \mu\text{s}$ , and permits the accumulation of energy. When a suitable amount of energy is stored, the cracks branches out again; this sequence is repeated until the specimen splits into two parts.



(a)



(b)



(c)



(d)



(e)



(f)

Figure 5.4: PMMA specimen at loading rate  $1000 \text{ s}^{-1}$ . Branching patterns at successive times: (a) 3.2; (b) 3.4; (c) 3.6; (d) 3.8; (e) 4.0; (f) 4.6  $\mu\text{s}$ .

The main crack velocity versus time is plotted in Fig. 5.5. The plot shows a drop of the crack velocity when side branches develop. Oscillations in the velocity also appear when the propagation is faster than a critical value, which is around 340-350 m/s (Fig. 5.5). This results in a perfect agreement with the critical velocity  $v_c$  340 m/s reported by Fineberg and Sharon [44, 115, 43].

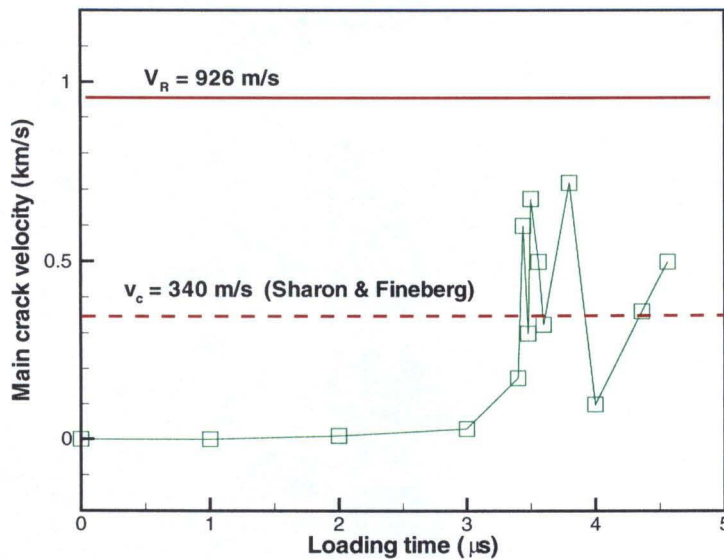
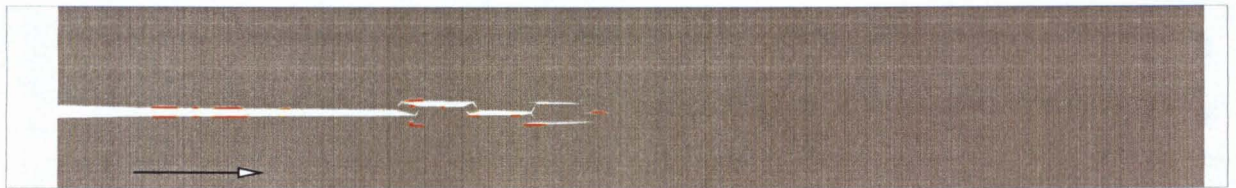


Figure 5.5: PMMA specimen at loading rate  $1000 \text{ s}^{-1}$ ; main crack velocity history,  $V_R = 926 \text{ m/s}$  is the Rayleigh wave velocity. The velocity is averaged over a distance of 0.2 mm along the horizontal direction.

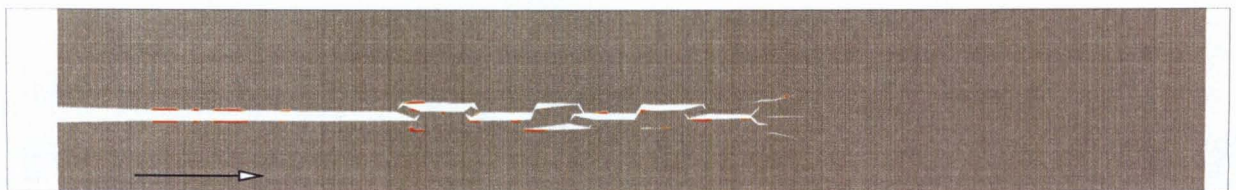
Increasing the loading rate up to  $5000 \text{ s}^{-1}$ , the crack starts as a smooth single crack (Fig. 5.6a). A short time later, small short-lived side branches form and die, so that the crack surface appears to to be hackled periodically (Fig. 5.6 b, c). Finally the crack sprouts out into two long-lived branches, almost symmetric with respect to the main crack (Fig. 5.6 d).



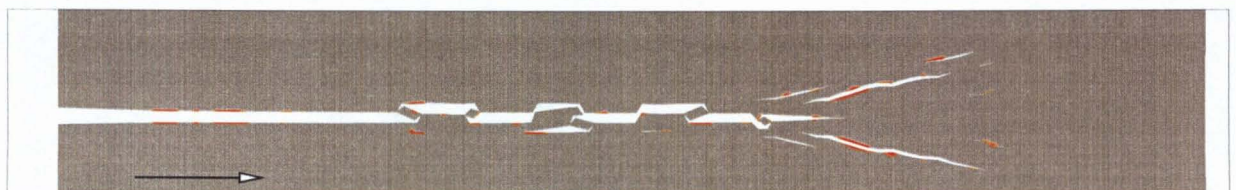
(a)



(b)



(c)



(d)

Figure 5.6: PMMA specimen at loading rate  $5000 \text{ s}^{-1}$ . Branching patterns at successive times: (a)  $1.08 \mu\text{s}$ ; (b)  $1.28 \mu\text{s}$ ; (c)  $1.48 \mu\text{s}$ ; (d)  $1.68 \mu\text{s}$ . The arrow of length  $0.25 \text{ mm}$  indicates the direction of main crack propagation and scales the branches extension.

The final branch angle is around  $14$  degrees (Fig. 5.7), and nicely falls within the

range of 10 to 15 degrees reported in literature ([114]) for scales about 0.1-0.3 mm.

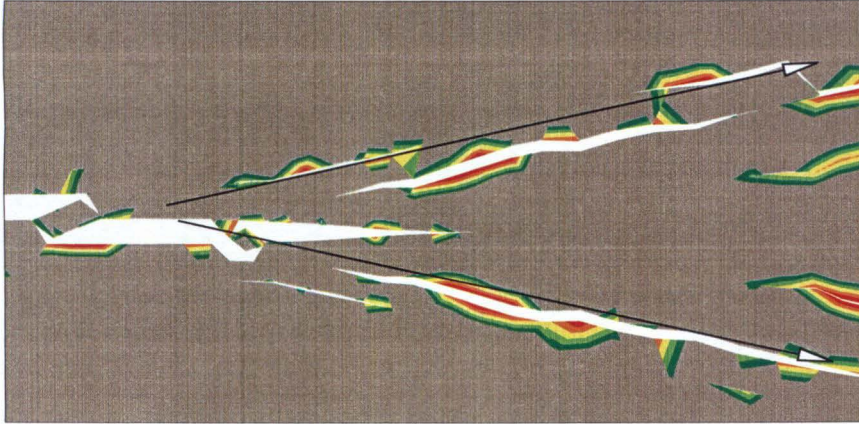
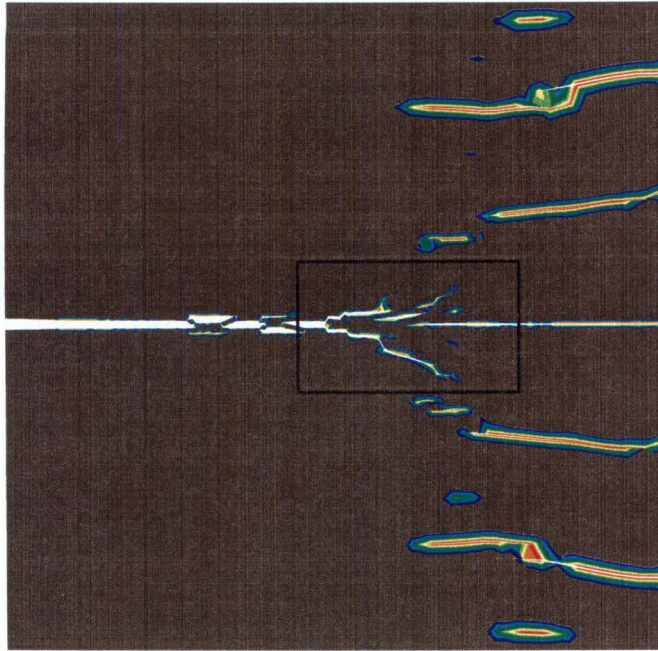


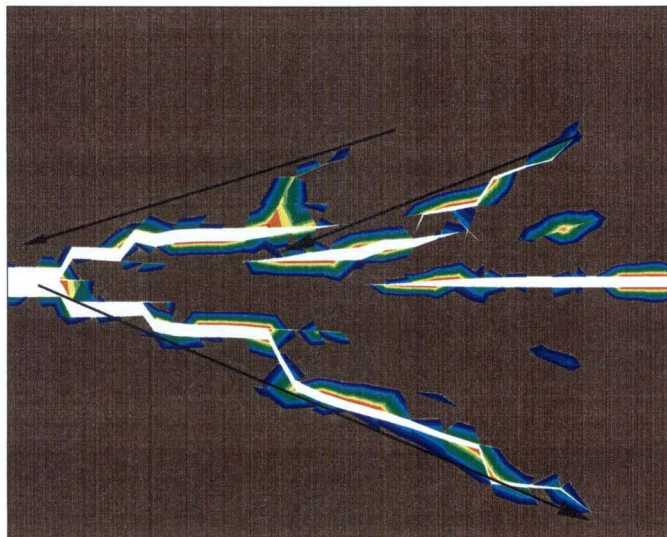
Figure 5.7: PMMA specimen at loading rate  $5000 \text{ s}^{-1}$ , time  $1.72 \mu\text{s}$ . The arrow shows a branching angle about 14 degrees.

When the loading rate is higher, i. e.,  $10,000 \text{ s}^{-1}$ , similar phenomena are observed. The main differences are in the length of the hackled region (Fig. 5.9) which is shorter compared to the one obtained at a smaller loading rate (Fig. 5.4); and the first appearance of long-lived branches is earlier. Besides, other cracks develop in regions far from main trajectory of the crack, and a straight crack starts form the opposite side of the original notch. The two main cracks try to coalesce during the later stages of the process.

The branching angle in this case appear to be bigger, about 19 to 24 degrees (Fig. 5.8b).

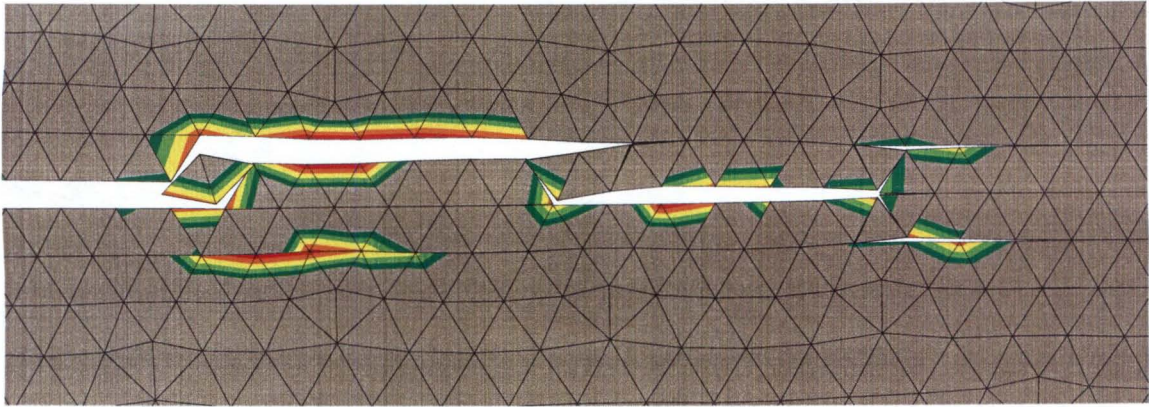


(a)

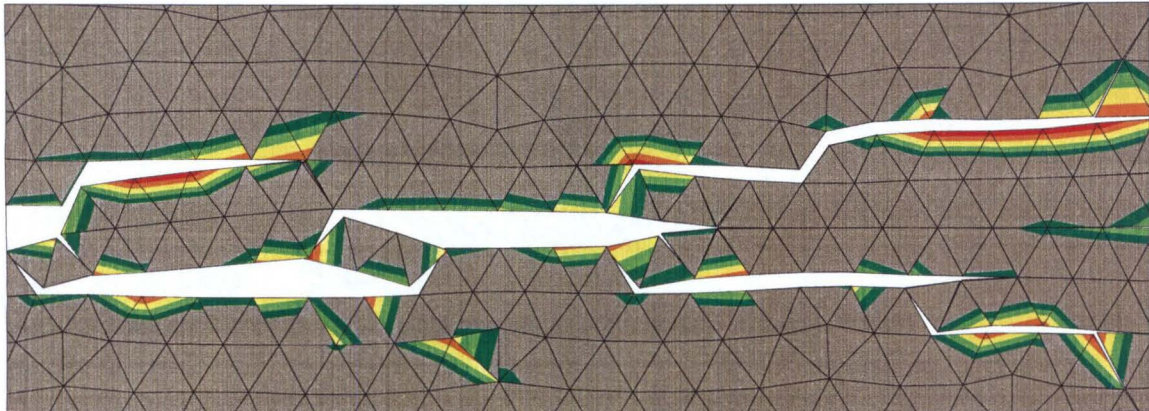


(b)

Figure 5.8: PMMA specimen: branching pattern and branching angle at  $1.2 \mu\text{s}$  for the strain rate  $10,000 \text{ s}^{-1}$ . The branching angle is between 19 to 24 degrees.



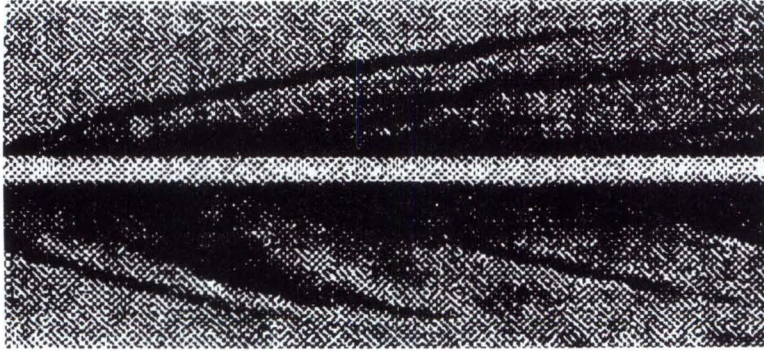
(a)



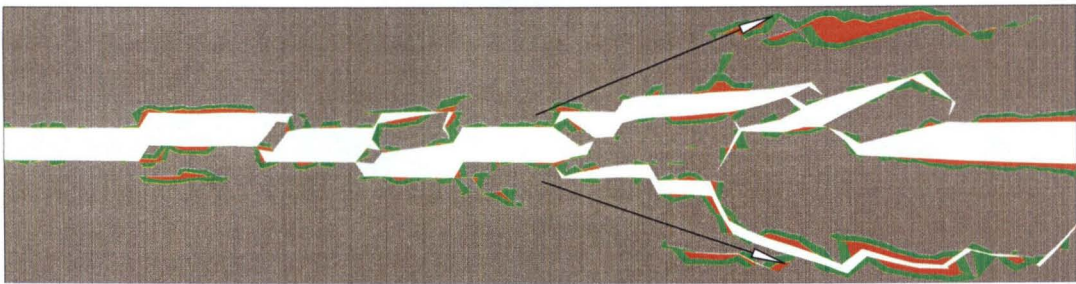
(b)

Figure 5.9: PMMA specimen: zoomed view of the hackled region at time  $0.8 \mu\text{s}$  and  $1 \mu\text{s}$ , loading rate  $10,000 \text{ s}^{-1}$ .

A comparison between numerical and experimental branching patterns is shown in Fig. 5.10. Similar branch profiles are observed, i.e., the parallel branches start out with an angle inclined to the main crack, after propagating for a while they tend to go parallel to the main crack, following a parabolic shape. This explains why the branching angle appears to be larger in a microscopic scale than in a macroscopic scale [115].



(a)



(b)

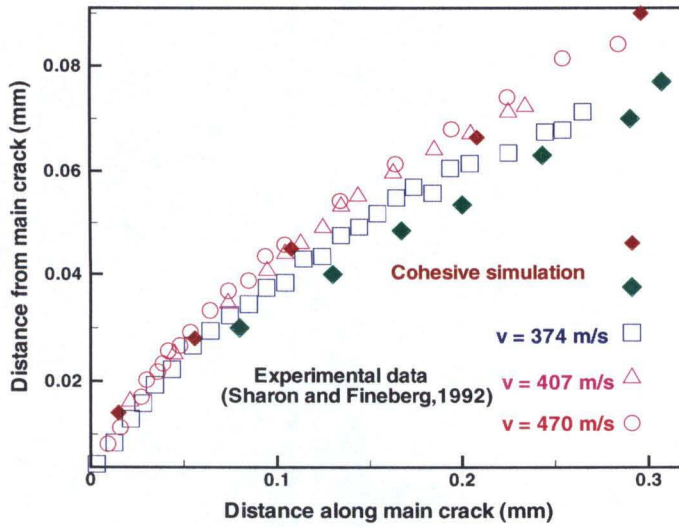
Figure 5.10: PMMA specimen: branching pattern compared with experiments for loading rate  $10,000 \text{ s}^{-1}$ .

We now examine the shape and structure of the micro branches. The experiments reported by Fineberg and Sharon [44, 43], about the mean profile of the distributed branches are shown in Fig. 5.11, where the branches follow a distinct trajectory of the form:

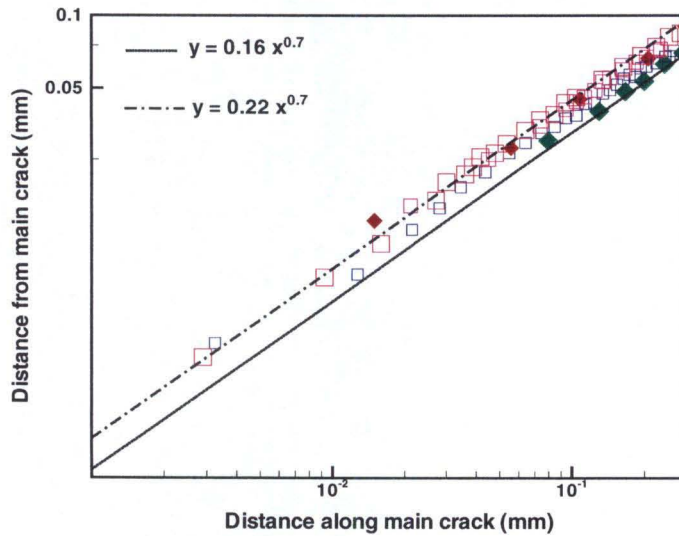
$$y = 0.2x^{0.70} \quad (5.3)$$

$y$  being normal and  $x$  being parallel to the propagation direction of the main crack. The experiments show that the branch trajectories are independent of the velocity near the main crack, but they diverge successively. Eq. (5.3) holds for velocities

within 10 percent of  $v_c$ , but the coefficient 0.2 requires a slight adjustment for higher velocities. During the numerical investigation, because of the oscillation of the main crack velocity, it is difficult to evaluate the exact velocity value for each branch, so we collected the branch profile data without distinguishing the difference from the main crack velocity. Two sets of data were obtained for the loading rates 5000 and 1000  $s^{-1}$ , and are reported in Fig. 5.11 to compare with the experiments. The same exponent 0.7 is obtained, and the coefficients range about 0.17 and 0.2, showing that a very good agreement has been achieved.



(a)



(b)

Figure 5.11: The mean profile of micro branches obtained by Fineberg and Sharon [44, 43] (hollow symbols) for different propagation velocities compared with numerical simulation (filled diamonds).

Interesting observations arise from the analysis of the energy consumption during the crack propagation and of the total fracture area produced. Fig. 5.12 shows the energy histories for the PMMA specimen, at the loading rate of  $5000 \text{ s}^{-1}$ . The cohesive energy increases when new surfaces form, i.e., when fracture area increases. The strain energy show a drop at later time. The plot of the cohesive energy release rate shows a peak following the decreasing of the strain energy. An interesting observation is that the kinetic energy and the energy release rate show the same trend, the two peaks being shifted about  $0.5 \mu\text{s}$ . This reveals that the accumulated deformation energy is partially dissipated through branching into cohesive energy and partially provides kinetic energy for separation of the newly formed fracture surfaces. Afterwards, a large increase of the cohesive energy and a delayed increase of the kinetic energy are observed. Once the energy has been dissipated, the energy release rate decreases, the crack slows down, and some side branches die; it follows that the kinetic energy also decreases. This plot confirms that the formation of side branches does dissipate much more energy than the propagation of a single crack.

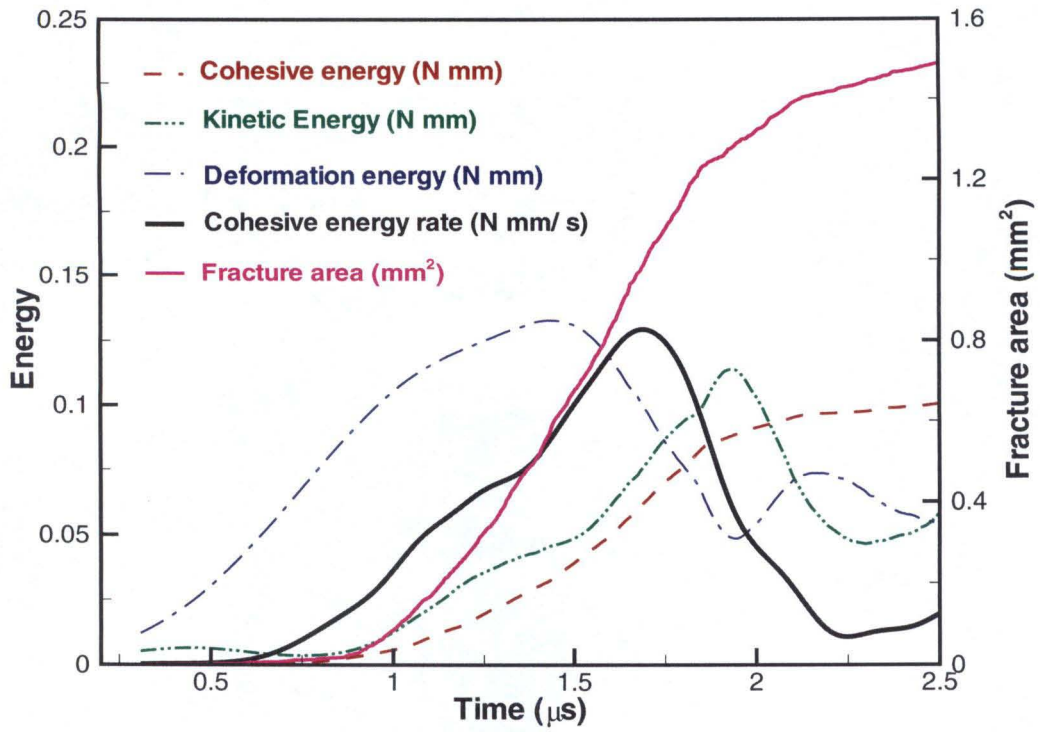


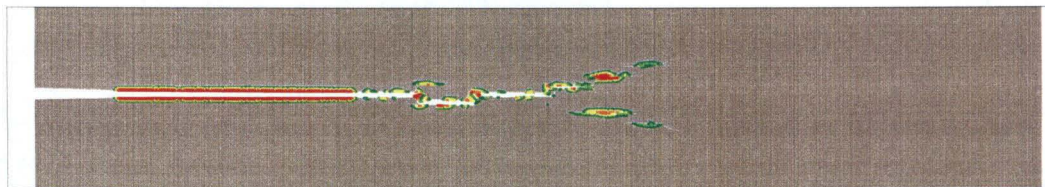
Figure 5.12: PMMA specimen: loading rate  $5000 \text{ s}^{-1}$ . Energy and fracture area evolution.



(a)



(b)



(c)



(d)

Figure 5.13: Homalite-100 specimen: branching pattern at loading rate  $1000 \text{ s}^{-1}$ , at times: (a) 4.7; (b) 5.2; (c) 5.7; (d) 6.2  $\mu\text{s}$ .

The mesh size adopted for mesh F is  $20 \mu\text{m}$ , very close to the characteristic size ( $19.5 \mu\text{m}$ ). To rule out the possibility of a mesh size dependence, we repeated the same analysis for a different material, Homalite-100, which has a characteristic length

of 2.7 mm. We adopted the same mesh F. Similar results have been obtained; they are reported in Fig. 5.13 and Fig. 5.14.

Adopting the same loading rate used in the PMMA simulation (Fig. 5.4), the difference in the material properties results mainly in a different branching angle, which is about 16 to 18 degrees. The long-lived branches appear earlier.

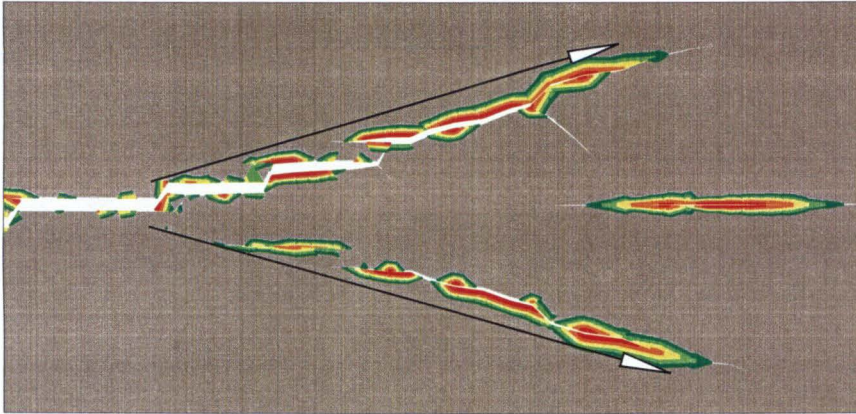


Figure 5.14: Detailed view of branching pattern for Homalite-100 at  $6.2 \mu\text{s}$ , for loading rate  $1000 \text{ s}^{-1}$ . Branching angle about 16.5 degrees.

## Summary

We applied the cohesive model to investigate the dynamic fracture under pure tension (mode I loading) for PMMA, and have obtained the main features of the experiments by Fineberg and Sharon [43, 44, 118, 114, 116]. Below a critical velocity  $v_c$ , a single crack propagates and produces a smooth fracture surface in its wake; beyond  $v_c$ , dynamic instability, in the form of micro branches, interrelates with the main crack, resulting in a non-trivial structure of the fracture surface. Once the instability occurs, the amount of energy dissipated by the system can increase up to an order of magnitude. This simulation not only further testifies to the fidelity of our cohesive model, its descriptive and predictive power, but also confirms the continuum theory of fracture, a physical process that naturally connects large and small scales [47].

## Chapter 6 Conclusions and future work

During this dissertation, based on the previous work by Camacho and Ortiz [26], Pandolfi and Ortiz [92, 95], we have extended the cohesive theories of fracture to transversely isotropic materials, incorporated with small strain frictional contact and adiabatic thermal effect, by direct simulation of impact-induced damage on graphite/epoxy composites, sandwich structures and brittle polymers. The simulations have been conducted using a partially self-adapting procedure, able to explicitly reproduce the evolution of crack initiation and propagation. The coupling of cohesive theories with an adaptive procedure can be easily applied to any kind of brittle material, and has been also used to reproduce ductile fracture [94].

The extended cohesive theories of fracture are proved predictive in situations involving material interfaces, material heterogeneity, material anisotropy, dynamic shear cracks and dynamic crack branching. We have reproduced the double shock wave structure, verified that “hot spots” arise from the frictional contact between fracture surfaces in the graphite/epoxy composites simulation; we also confirmed the shear-driven nature of the debonding between layers, the main damage patterns for the failure mode selection of sandwich structure investigation; for the first time in available literature, using continuum cohesive model, we are able to reproduce the dynamic branching instability in brittle materials; the obtained power-law scaling relation of the branch profiles in PMMA reached an excellent agreement with the experimental results of Fineberg and Sharon [43, 44, 118].

The extension to include heat conduction in bulk material and full thermo-mechanical coupling can be easily added to the model; the incorporation of true (non-smooth) contact would enable a full 3D impact modeling of the projectile over a target; parallel implementation of the fragmentation and contact algorithms will bring even higher computational performance and fidelity; the combination with adaptive remeshing for bulk material and fragmentation would render more complicated problems solv-

able. We also envision extensions to include optimization by defining a single target function for damage, and using genetic algorithms for optimal design of layered, composite, sandwich structures.

# Appendix A Interpolation in 3D

## tetrahedra - field interpolation

In order to extrapolate the field variables from the Gauss points of a tetrahedra to those of the cohesive surface, the right interpolation procedure is very important.

We want to find the value of a field scalar variable  $v(\mathbf{x})$  on the Gauss points of a facet of a tetrahedra, the values  $v_i$  of the same variable being known at the volume Gauss points of the element. We extrapolate the gauss points values  $v_i$  of the variable into the nodes  $V_i$ , then we will interpolate the node values  $V_i$  into the gauss point on the requested facet.

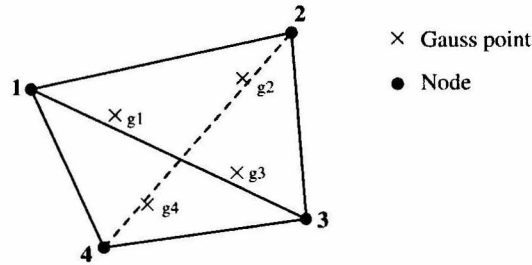


Figure A.1: Nodes and Gauss points location in a tetrahedra.

Let's number the nodes 1, 2, 3 and 4 (see Fig. A.1), and  $v_1, v_2, v_3, v_4$  the values of the variable field into the corresponding gauss points. The volume coordinates  $\mathbf{n}_i$  of the four corner nodes in the parent configuration are

$$\begin{aligned}
 \mathbf{n}_1^T &= \begin{bmatrix} 1 & 0 & 0 & 0 \end{bmatrix} \\
 \mathbf{n}_2^T &= \begin{bmatrix} 0 & 1 & 0 & 0 \end{bmatrix} \\
 \mathbf{n}_3^T &= \begin{bmatrix} 0 & 0 & 1 & 0 \end{bmatrix} \\
 \mathbf{n}_4^T &= \begin{bmatrix} 0 & 0 & 0 & 1 \end{bmatrix}
 \end{aligned} \tag{A.1}$$

In the same configuration, the volume coordinates  $\mathbf{g}_i$  of the four gauss point are

$$\begin{aligned}\mathbf{g}_1^T &= \begin{bmatrix} g_a & g_b & g_b & g_b \end{bmatrix} \\ \mathbf{g}_2^T &= \begin{bmatrix} g_b & g_a & g_b & g_b \end{bmatrix} \\ \mathbf{g}_3^T &= \begin{bmatrix} g_b & g_b & g_a & g_b \end{bmatrix} \\ \mathbf{g}_4^T &= \begin{bmatrix} g_b & g_b & g_b & g_a \end{bmatrix}\end{aligned}\tag{A.2}$$

where

$$g_a = 0.5854102, \quad g_b = 0.1381966\tag{A.3}$$

The gauss points values  $v_i$  of the variable  $v(\mathbf{x})$  are interpolated from the nodal values  $V_i$  as

$$\mathbf{v} = \mathbf{M}\mathbf{V}, \quad \begin{bmatrix} v_1 \\ v_2 \\ v_3 \\ v_4 \end{bmatrix} = \begin{bmatrix} g_a & g_b & g_b & g_b \\ g_b & g_a & g_b & g_b \\ g_b & g_b & g_a & g_b \\ g_b & g_b & g_b & g_a \end{bmatrix} \begin{bmatrix} V_1 \\ V_2 \\ V_3 \\ V_4 \end{bmatrix}\tag{A.4}$$

whereas the inverse relation is

$$\mathbf{V} = \mathbf{M}^{-1}\mathbf{v}, \quad \begin{bmatrix} V_1 \\ V_2 \\ V_3 \\ V_4 \end{bmatrix} = \begin{bmatrix} n_a & n_b & n_b & n_b \\ n_b & n_a & n_b & n_b \\ n_b & n_b & n_a & n_b \\ n_b & n_b & n_b & n_a \end{bmatrix} \begin{bmatrix} v_1 \\ v_2 \\ v_3 \\ v_4 \end{bmatrix}\tag{A.5}$$

where

$$n_a = 1.927050, \quad n_b = -0.309017\tag{A.6}$$

The evaluation of the function  $v(\mathbf{x})$  on the facet defined by the nodes 1, 2 and 3 is then done by a surface interpolation of the nodal values  $V_i$ ,  $i = 1, 2, 3$  (see Fig. A).

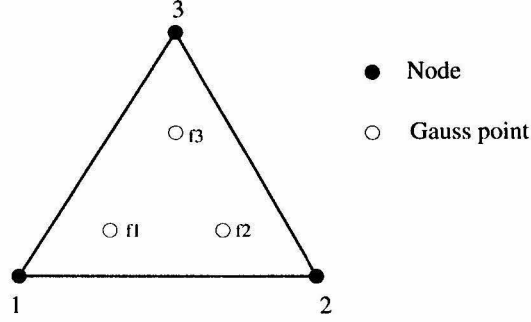


Figure A.2: Nodes and gauss points location on a facet.

The area coordinates  $s_i$  of the three gauss points of the facet in the parent configuration are as follows:

$$\begin{aligned} \mathbf{F}_1^T &= \begin{bmatrix} f_a & f_b & f_b \end{bmatrix} \\ \mathbf{F}_2^T &= \begin{bmatrix} f_b & f_a & f_b \end{bmatrix} \\ \mathbf{F}_3^T &= \begin{bmatrix} f_b & f_b & f_a \end{bmatrix} \end{aligned} \quad (\text{A.7})$$

where

$$f_a = 0.6666666, \quad f_b = 0.1666666 \quad (\text{A.8})$$

The interpolated values  $s_i^\alpha$  of the function on the facet  $\alpha$  are

$$\mathbf{s}^\alpha = \mathbf{T}\mathbf{V}^\alpha \quad (\text{A.9})$$

where  $V^\alpha$  denotes the subset of  $V$  containing the nodes of the facet  $\alpha$ . For example, in the case of the facet  $\alpha = 1$ , being  $\mathbf{V}^{1T} = [V_1 \ V_2 \ V_3]$ , we obtain the following:

$$\mathbf{s}^1 = \begin{bmatrix} s_1^1 \\ s_2^1 \\ s_3^1 \end{bmatrix} = \mathbf{T}\mathbf{V}^1 = \begin{bmatrix} f_a & f_b & f_b \\ f_b & f_a & f_b \\ f_b & f_b & f_a \end{bmatrix} \begin{bmatrix} V_1 \\ V_2 \\ V_3 \end{bmatrix} \quad (\text{A.10})$$

We can now rewrite  $\mathbf{V}^1$  as follows:

$$\mathbf{V}^1 = \mathbf{M}_1^{-1}\mathbf{v}, \quad \begin{bmatrix} V_1 \\ V_2 \\ V_3 \end{bmatrix} = \begin{bmatrix} n_a & n_b & n_b & n_b \\ n_b & n_a & n_b & n_b \\ n_b & n_b & n_a & n_b \end{bmatrix} \begin{bmatrix} v_1 \\ v_2 \\ v_3 \\ v_4 \end{bmatrix} \quad (\text{A.11})$$

Replacing eq. (A.11) into eq. (A.10), we obtain

$$\mathbf{s}^1 = \mathbf{T}\mathbf{M}_1^{-1}\mathbf{v} = \mathbf{Q}_1\mathbf{v}, \quad \begin{bmatrix} f_a & f_b & f_b \\ f_b & f_a & f_b \\ f_b & f_b & f_a \end{bmatrix} \begin{bmatrix} n_a & n_b & n_b & n_b \\ n_b & n_a & n_b & n_b \\ n_b & n_b & n_a & n_b \end{bmatrix} \begin{bmatrix} v_1 \\ v_2 \\ v_3 \\ v_4 \end{bmatrix} \quad (\text{A.12})$$

which gives for the matrix  $\mathbf{Q}_1$ :

$$\mathbf{Q}_1 = \begin{bmatrix} q_a & q_b & q_b & q_c \\ q_b & q_a & q_b & q_c \\ q_b & q_b & q_a & q_c \end{bmatrix} \quad (\text{A.13})$$

where

$$\begin{aligned} q_a &= f_a n_a + 2f_b n_b = 1.18169 \\ q_b &= f_a n_b + f_b n_a + f_b n_b = 0.0636608 \\ q_c &= (f_a + 2f_b) n_b = n_b = -0.309017 \end{aligned} \quad (\text{A.14})$$

For the three remaining facets, we will have

$$\mathbf{s}^\alpha = \mathbf{Q}_\alpha \mathbf{v} \quad (\text{A.15})$$

with

$$\mathbf{Q}_2 = \begin{bmatrix} q_c & q_a & q_b & q_b \\ q_c & q_b & q_a & q_b \\ q_c & q_b & q_b & q_a \end{bmatrix}, \quad \mathbf{Q}_3 = \begin{bmatrix} q_b & q_c & q_a & q_b \\ q_b & q_c & q_b & q_a \\ q_a & q_c & q_b & q_b \end{bmatrix}, \quad \mathbf{Q}_4 = \begin{bmatrix} q_b & q_b & q_c & q_a \\ q_a & q_b & q_c & q_b \\ q_b & q_a & q_c & q_b \end{bmatrix} \quad (\text{A.16})$$

or, alternatively,

$$\mathbf{s}^\alpha = \mathbf{Q}\mathbf{v}^\alpha, \quad \mathbf{Q} = \mathbf{Q}_1 \quad (\text{A.17})$$

where

$$\begin{aligned} \mathbf{v}^{1T} &= \begin{bmatrix} v_1 & v_2 & v_3 & v_4 \end{bmatrix} \\ \mathbf{v}^{2T} &= \begin{bmatrix} v_2 & v_3 & v_4 & v_1 \end{bmatrix} \\ \mathbf{v}^{3T} &= \begin{bmatrix} v_3 & v_4 & v_1 & v_2 \end{bmatrix} \\ \mathbf{v}^{4T} &= \begin{bmatrix} v_4 & v_1 & v_2 & v_3 \end{bmatrix} \end{aligned} \quad (\text{A.18})$$

# Bibliography

- [1] F.F Abraham, D. Brodbeck, R.A. Rafey, and Rudge W.E. Instability Dynamics of Fracture: a Computer Simulation Investigation. *Physical Review Letters*, 73:272–275, 1994.
- [2] F.F Abraham, D. Brodbeck, Rudge W.E., and Xiaopeng Xu. A Molecular Dynamics Investigation of Rapid Fracture Mechanics. *Journal of the Mechanics and Physics of Solids*, 45(9):1595–1619, 1996.
- [3] F.F Abraham and Huajian Gao. How Fast Can Crack Propagate? *Physical Review Letters*, 84(14):3113–3116, 2000.
- [4] S. Abrate. Impact on Laminated Composite Materials. *Applied Mechanics Reviews*, 44(4):155–190, 1991.
- [5] S. Abrate. Impact on Laminated Composites: Recent Advances. *Applied Mechanics Reviews*, 47(11):517–544, 1994.
- [6] S. Abrate. Localized Impact on Sandwich Structures With Laminated Facings. *Applied Mechanics Reviews*, 50(2):69–82, 1997.
- [7] O. Allix and P. Ladeveze. Interlaminar interface modelling for the prediction of laminates delamination. *Composite structures*, 22:235–242, 1992.
- [8] O. Allix, P. Ladeveze, and A. Coriglino. Damage analysis of interlaminar fracture specimens. *Composite structures*, 31:61–74, 1995.
- [9] W.T. Ashurst and W.G. Hoover. Microscopic fracture studies in the two-dimensional triangular lattice. *Phys. Rev. B*, 14:1465–1473, 1976.
- [10] C. Atkinson. The interaction between a dislocation and a crack. *International Journal of Fracture Mechanics*, 2:567–575, 1966.

- [11] C. Atkinson, C. Bastero, and M.I.s Sanchez. Prediction of branching (or relaxation) angle in anisotropic or isotropic elastic bimaterials with rigid substrates. *International Journal of Fracture Mechanics*, 67:231–261, 1994.
- [12] A.G. Avans, B.J. Dalglisch, M.Y. He, and Hutchinson J.W. Analysis of Branched Interface Cracks Between Dissimilar Anisotropic Media. *Journal of Applied Mechanics*, 56:844–849, 1989.
- [13] L. Banks-Sills and D. Ashkenazi. A Note on Fracture Criteria for Interface Fracture. *International Journal of Fracture*, 103:177–188, 2000.
- [14] L. Banks-Sills, N. Travitzky, D. Ashkenazi, and R. Eliasi. A Methodology for Measuring Interface Fracture Properties of Composite Materials. *International Journal of Fracture*, 99:143–160, 1999.
- [15] G. I. Barrenblatt. The mathematical theory of equilibrium of cracks in brittle fracture. *Advances in Applied Mechanics*, 7:55–129, 1962.
- [16] R. Barsoum. Triangular Quarter-Point Elements as Elastic and Perfectly-plastic Crack Tip Elements. *International Journal for Numerical Methods in Engineering*, 11:85–98, 1977.
- [17] T. Belytschko. An overview of semidiscretization and time integration procedures. In T. Belytschko and T. J. R. Hughes, editors, *Computational Methods for Transient Analysis*, pages 1–65. North-Holland, 1983.
- [18] D.B. Bogy. On the Plane Elastostatic Problem of a Loaded Crack Terminating at a Material Interface. *Journal of Applied Mechanics*, 38:911–918, 1971.
- [19] J.F. Boudet and S. Ciliberto. Interaction of sound with fast crack propagation. *Physical Review Letters*, 80:341–344, 1998.
- [20] J.F. Boudet, S. Ciliberto, and V. Steinberg. Dynamics of crack propagation in brittle materials. *Journal of Physics, II*, 6:1493–1516, 1996.
- [21] J.F. Boudet, V. Steinberg, and S. Ciliberto. EXPERIMENTAL-STUDY OF THE INSTABILITY OF CRACK-PROPAGATION IN BRITTLE MATERIALS. *Europhysi. Lett.*, 30(6):337–342, 1995.

- [22] A. Braides and V. Chiado'Piat. Integral representation results for functionals defined on sbv. *J. Math. Pures Appl.*, 75:595–626, 1996.
- [23] K. B. Broberg. Crack expanding with constant velocity in an anisotropic solid under anti-plane strain. *International Journal of Fracture*, 93(1–4):1–12, 1989.
- [24] K. B. Broberg. Intersonic crack propagation in orthotropic material. *International Journal of Fracture*, 99(1–2):1–11, 1999.
- [25] R. Burridge, G. Conn, and L. B. Freund. The stability of a rapid mode ii crack with finite cohesive traction. *Journal of Geophysical Research*, 85:2210–2222, 1979.
- [26] G. T. Camacho and M. Ortiz. Computational modelling of impact damage in brittle materials. *International Journal of Solids and Structures*, 33(20–22):2899–2938, 1996.
- [27] A. Carpinteri. *Mechanical Damage and Crack Growth in Concrete*. Martinus Nijhoff, Dordrecht, The Netherlands, 1986.
- [28] M. Charalambides, A.J. Kinnloch, Y. Wang, and J.G. Williams. On the Analysis of Mixed-mode Failure. *International Journal of Fracture*, 54:269–291, 1992.
- [29] Y. Chen and N. Hasebe. New Integration Scheme for the Branch Crack Problem. *Engineering Fracture Mechanics*, 52(5):791–801, 1995.
- [30] R. M. Christensen. *Mechanics of Composite Materials*. Wiley, New York, 1979.
- [31] D. Coker and A. J. Rosakis. Experimental observations of intersonic crack growth in asymmetrically loaded unidirectional composites plates. *SM Report*, pages 1–34, 1998.
- [32] D. Coker and A.J. Rosakis. Experimental observations of intersonic crack growth in asymmetrically loaded unidirectional composites plates. *Philosophical Magazine A*, 81(3):571–595, 2001.
- [33] M. Comninou. The Interface Crack. *ASME JOURNAL OF APPLIED MECHANICS*, 44:631–636, 1977.
- [34] M. Comninou. The Interface Crack in a Shear Field. *ASME JOURNAL OF APPLIED MECHANICS*, 45:287–290, 1978.

- [35] M. Comninou and D. Schmueser. The Interface Crack in a Combined Tension-Compression and Shear Field. *ASME JOURNAL OF APPLIED MECHANICS*, 46:345–348, 1979.
- [36] A. Coriglino. Formulation, identification and use of interface models in the numerical analysis of composite delamination. *International Journal of Solids and Structures*, 30:2779–2811, 1993.
- [37] C. Daux, N. Moes, J. Dolbow, N. Sukumar, and T. Belytschko. Arbitrary Branched and Intersecting Cracks with the Extended Finite Element Method. *International Journal for Numerical Methods in Engineering*, 48:1741–1760, 2000.
- [38] A. De-Andrés, J. L. Pérez, and M. Ortiz. Elastoplastic finite element analysis of three-dimensional fatigue crack growth in aluminum shafts subjected to axial loading. *International Journal of Solids and Structures*, 36(15):2231–2258, 1999.
- [39] D. S. Dugdale. Yielding of steel sheets containing slits. *Journal of the Mechanics and Physics of Solids*, 8:100–104, 1960.
- [40] A.H. England. A Crack Between Dissimilar Media. *Journal of Applied Mechanics*, 87:400–402, 1965.
- [41] F. Erdogan. Stress Distributions in a Bonded Dissimilar Materials With Cracks. *Journal of Applied Mechanics*, 32:403–410, 1965.
- [42] F. Erdogan and G. Gupta. The Stress Analysis of Multilayered Composites With a Flaw. *International Journal of Solids and Structures*, 7:39–61, 1971.
- [43] J. Fineberg, S.P. Gross, M. Marder, and H.L. Swinney. Instability in Dynamic Fracture. *Physical Review Letters*, 67:457–460, 1992.
- [44] J. Fineberg, S.P. Gross, M. Marder, and H.L. Swinney. Instability in the Propagation of Fast cracks. *Phys. Rev. B*, 45:5146–5154, 1992.
- [45] M. Fleming, Y. Chu, B. Moran, and T. Belytschko. Enriched Element-free Galerkin Methods for Crack Tip Fields. *International Journal for Numerical Methods in Engineering*, 40(8):1483–1504, 1997.

- [46] I. Fonseca and N. Fusco. Regularity Results for Anisotropic Image Segmentation Models. *Proc. R. Soc. Edin.*, 127A:889–902, 1997.
- [47] L. B. Freund. *Dynamic Fracture Mechanics*. Cambridge Univ. Press, New York, 1990.
- [48] H. G. Georgiadis. *International Journal of Fracture*, 301:175, 1986.
- [49] J.G. Goree and W.A. Venezia. Bonded Elastic Half Planes With an Interface Crack and a Perpendicular Intersecting Crack That Extends Into the Adjacent Material–I. *International Journal of Engineering Science*, 15:1–17, 1977.
- [50] J.G. Goree and W.A. Venezia. Bonded Elastic Half Planes With an Interface Crack and a Perpendicular Intersecting Crack That Extends Into the Adjacent Material–II. *International Journal of Engineering Science*, 15:19–27, 1977.
- [51] S.P. Gross, J. Fineberg, W.D. McCormick, M. Marder, and H.L. Swinney. Acoustic Emissions from Rapidly Moving Cracks. *Physical Review Letters*, 71:3162–3165, 1993.
- [52] P. Gumbsch, S.J. Zhou, and B.L. Holian. Molecular Dynamics Investigation of Dynamic Crack Instability. *Phys. Rev. B*, 55(6):3445–3455, 1997.
- [53] K. Hayashi and S. Nemat-Nasser. Energy-release Rate and Crack Kinking under Combined Loading. *Journal of Applied Mechanics*, 48:520–524, 1981.
- [54] K. Hayashi and S. Nemat-Nasser. On Branched, Interface Cracks. *Journal of Applied Mechanics*, 48:529–533, 1981.
- [55] Ming-yuan He, Bartlett, and Anthony Evans. Kinking of a crack out of an interface :Role of in-plane stress. *Journal of American Ceramic Society*, 74(4):767–771, 1991.
- [56] Ming-yuan He, A.G. Evans, and J.W. Hutchinson. Interface Cracking Phenomena in Constrained Metal Layers. *Acta Materialia*, 44:2963–2971, 1991.
- [57] Ming-yuan He and J.W. Hutchinson. Kinking of a Crack Out of an Interface. *Journal of Applied Mechanics*, 56:270–178, 1989.
- [58] H.J. Hermann and S. Roux. Statistical Models for the Fracture of Disordered Media. *North Holland, Amsterdam*, pages 1–12, 1990.

- [59] A. Hillerborg, M. Modeer, and P. E. Petersson. Analysis of crack formation and crack growth in concrete by means of fracture mechanics and finite elements. *Cement Concrete Research*, 6:773–782, 1976.
- [60] Y. Huang, Wang W., C. Liu, and A.J. Rosakis. Intersonic crack growth in bimaterial interfaces: an investigation of crack face contact. *Journal of the Mechanics and Physics of Solids*, 46(11):2233–2259, 1998.
- [61] Y. Huang, Wang W., C. Liu, and A.J. Rosakis. Analysis of intersonic crack growth in unidirectional fiber-reinforced composites. *Journal of the Mechanics and Physics of Solids*, 47(9):1893–1916, 1999.
- [62] T. J. R. Hughes. Analysis of transient algorithms with particular reference to stability behavior. In T. Belytschko and T. J. R. Hughes, editors, *Computational Methods for Transient Analysis*, pages 67–155. North-Holland, 1983.
- [63] T. J. R. Hughes. *The finite element method: linear static and dynamic finite element analysis*. Prentice-Hall, Englewood Cliffs, N.J., 1987.
- [64] J. W. Hutchinson and Z. Suo. Mixed mode cracking in layered materials. *Advances in Applied Mechanics*, 39:63–191, 1992.
- [65] E. Johnson. Process Region Changes for Rapidly Propagating Cracks. *International Journal of Fracture*, 55:47–63, 1992.
- [66] C. Kane, E. A. Repetto, M. Ortiz, and J. E. Marsden. Finite element analysis of nonsmooth contact. *Computer Methods in Applied Mechanics and Engineering*, 180:1–26, 1999.
- [67] J. Lambros and A. J. Rosakis. Development of a dynamic decohesion criterion for subsonic fracture of the interface between two dissimilar materials. *Proceedings of the Royal Society of London, A* 451:711–736, 1995.
- [68] J. Lambros and A.J. Rosakis. Dynamic crack initiation and growth in thick unidirectional graphite/epoxy plates. *Composites Science and Technology*, 57:55–65, 1997.
- [69] J.S. Langer. *Phys. Rev. A*, 46:3123–3130, 1992.

- [70] N.S. Lee. Elastic-plastic deformation at finite strains. *Journal of Applied Mechanics*, 36:1–21, 1969.
- [71] K.Y. Lin and J.W. Mar. Finite-Element Analysis of Stress Intensity Factors for Cracks in a Bimaterial Interface. *International Journal of Fracture*, 12:521–531, 1976.
- [72] C. Liu, Y. Huang, and A. J. Rosakis. Shear dominated transonic interfacial crack growth in a bimaterial—ii. asymptotic fields and favorable velocity regimes. *Journal of the Mechanics and Physics of Solids*, 43(2):198–206, 1995.
- [73] C. Liu, A. J. Rosakis, R. W. Ellis, and M. G. Stout. A study of the fracture behavior of unidirectional fiber-reinforced composite using coherent gradient sensing (cgs) interferometry. *International Journal of Fracture*, 90(4):355–382, 1998.
- [74] K.K. Lo. Analysis of branched cracks. *Journal of Applied Mechanics*, 45:797–802, 1979.
- [75] B.M. Malyshev and R.L. Salganik. The Strength of Adhesive Joints Using the Theory of Fracture. *International Journal of Fracture Mechanics*, 1:114–128, 1965.
- [76] M. Marder and J. Fineberg. How Things Break. *Physics Today*, September:24–29, 1996.
- [77] M. Marder and S. Gross. Origins of Crack-tip Instabilities. *Journal of the Mechanics and Physics of Solids*, 43(1):1–48, 1995.
- [78] M. Marder and Liu X. Instability in Lattice Fracture. *Physical Review Letters*, 71:2417–2420, 1993.
- [79] J. E. Marsden and T. J. R. Hughes. *Mathematical foundations of elasticity*. Prentice-Hall, Englewood Cliffs, N.J., 1983.
- [80] T. Martin, P. Espanol, M. A. Rubio, and I. Zuniga. Dynamic Fracture in a Discrete Model of a Brittle Elastic Solid. *Phys. Rev. E*, 61(6):6120–6131, 2000.
- [81] K. K Mathur, A. Needleman, and V. Tvergaard. Three dimensional analysis of dynamic ductile crack growth in a thin plate. *Journal of the Mechanics and Physics of Solids*, 44:439–464, 1996.

- [82] Marc Andre Meyers. *Dynamic Behavior of Materials*. John Wiley and Sons, inc., New York, 1990.
- [83] A. Needleman. A continuum model for void nucleation by inclusion debonding. *Journal of Applied Mechanics*, 54:525–531, 1987.
- [84] A. Needleman. An analysis of decohesion along an imperfect interface. *International Journal of Fracture*, 42:21–40, 1990.
- [85] A. Needleman. Micromechanical modeling of interfacial decohesion. *Ultramicroscopy*, 40:203–214, 1992.
- [86] A. Needleman. An analysis of intersonic crack growth under shear loading. *Journal of Applied Mechanics*, 66:847–857, 1999.
- [87] A. Needleman and A. J. Rosakis. The effect of bond strength and loading rate on the conditions governing the attainment of intersonic crack growth along interfaces. *Journal of the Mechanics and Physics of Solids*, 47(12):2411–2449, 1999.
- [88] J. Newman. An Improved Method of Collocation for the Stress Analysis of Cracked Plates with Various Shaped Boundaries. *Technical Report TN D-6376, NASA*, 1971.
- [89] K. Oguni and G. Ravichandran. A micromechanical model for failure of unidirectional fiber-reinforced composites. *International Journal of Solids and Structures*, 2001.
- [90] M. Ortiz. Microcrack coalescence and macroscopic crack growth initiation in brittle solids. *International Journal of Solids and Structures*, 24:231–250, 1988.
- [91] M. Ortiz. Computational micromechanics. *Computational Mechanics*, 18:321–338, 1996.
- [92] M. Ortiz and A. Pandolfi. A class of cohesive elements for the simulation of three-dimensional crack propagation. *International Journal for Numerical Methods in Engineering*, 44:1267–1282, 1999.
- [93] M. Ortiz and S. Suresh. Statistical properties of residual stresses and intergranular fracture in ceramic materials. *Journal of Applied Mechanics*, 60:77–84, 1993.

- [94] A. Pandolfi, P. R. Guduru, M. Ortiz, and A. J. Rosakis. Finite element analysis of experiments of dynamic fracture in c300 steel. *International Journal of Solids and Structures*, 37:3733–3760, 2000.
- [95] A. Pandolfi, C. Kane, M. Ortiz, and J. E. Marsden. Finite element analysis of non-smooth contact. *International Journal for Numerical Methods in Engineering*, 2001. Submitted.
- [96] A. Pandolfi, P. Krysl, and M. Ortiz. Finite element simulation of ring expansion and fragmentation. *International Journal of Fracture*, 95:279–297, 1999.
- [97] A. Pandolfi and M. Ortiz. Solid modeling aspects of three-dimensional fragmentation. *Engineering with Computers*, 14(4):287–308, 1998.
- [98] J. Planas, M. Elices, and G. V. Guinea. Book chapter: Cohesive cracks as a solution of a class of nonlocal problems. In Z. P. Bazant, editor, *Fracture and Damage in Quasi-brittle Structures. Experiment, modelling and Computer analysis*. E & FN SPON, 1994.
- [99] Q. Qin. Crack kinking in piezoelectric materials. *ACTA MECHANICA SINICA (English series)*, 14(4):339–352, 1998.
- [100] Q. Qin and Y. Mai. Crack branch in piezoelectric bimaterial system. *International Journal of Engineering Science*, 38:673–693, 2000.
- [101] K. Ravi-Chandar and W.G. Knauss. An Experimental Investigation into Dynamic Fracture II. Microstructural Aspects. *International Journal of Fracture*, 26:65–80, 1984.
- [102] K. Ravi-Chandar and W.G. Knauss. An Experimental Investigation into Dynamic Fracture III On Steady-state Crack Propagation and Crack Branching. *International Journal of Fracture*, 26:141–154, 1984.
- [103] E. A. Repetto, R. Radovitzky, and M. Ortiz. Finite element simulation of dynamic fracture and fragmentation of glass rods. *Computer Methods in Applied Mechanics and Engineering*, 183(1–2):3–14, 2000.

- [104] J. R. Rice. Mathematical analysis in the mechanics of fracture. In H. Liebowitz, editor, *Fracture*, pages 191–311. Academic Press, 1968.
- [105] J. R. Rice and G.C. Sih. Plane Problems of Cracks in Dissimilar Media. *Journal of Applied Mechanics*, 32:418–423, 1965.
- [106] J.R. Rice. Inelastic constitutive relations for solids : an internal-variable theory and its applications to metal plasticity. *Journal of the Mechanics and Physics of Solids*, 19:433–455, 1971.
- [107] A. J. Rosakis, O. Samudrala, R. P. Singh, and A. Shukla. Intersonic crack propagation in bimaterial systems. *Journal of the Mechanics and Physics of Solids*, 46(10):1789–1813, 1998.
- [108] A.J. Rosakis, O. Samudrala, and D. Coker. Cracks faster than the shear wave speed. *Science*, 284(5418):1337–1340, 1999.
- [109] J. H. Rose, J. Ferrante, and J. R. Smith. Universal binding energy curves for metals and bimetallic interfaces. *Physical Review Letters*, 47(9):675–678, 1981.
- [110] G. Ruiz, M. Ortiz, and A. Pandolfi. Three-dimensional finite-element simulation of the dynamic brazilian tests on concrete cylinders. *International Journal for Numerical Methods in Engineering*, 48(7):963–994, 2000.
- [111] G. Ruiz, A. Pandolfi, and M. Ortiz. Three-dimensional cohesive modeling of dynamic mixed-mode fracture. *International Journal for Numerical Methods in Engineering*, 2001. To appear.
- [112] G. Ruiz, C. Yu, and M. Ortiz. Finite-element simulation of the dynamic behavior of advanced ceramics. *Anales de Mecanica de la Fractura*, 18:414–419, 2001.
- [113] K. Runde. Dynamic instability in crack propagation. *Phys. Rev. E*, 49(4):2597–2600, 1994.
- [114] E. Sharon and J. Fineberg. Energy Dissipation in Dynamic Fracture. *Physical Review Letters*, 76(12):2117–2120, 1996.
- [115] E. Sharon and J. Fineberg. Microbranching Instability and the Dynamic Fracture of Brittle Materials. *Physical Review B*, 54(10):7128–7139, 1996.

- [116] E. Sharon and J. Fineberg. Universal Features of the Microbranching Instability in Dynamic Fracture. *Philosophical Magazine B*, 78(2):243–251, 1998.
- [117] E. Sharon and J. Fineberg. Confirming the Continuum Theory of Dynamic Brittle Fracture for Fast Cracks. *Letters to Nature*, 397:333–335, 1999.
- [118] E. Sharon, Gross S. P., and J. Fineberg. Local Crack Branching as a Mechanism for Instability in Dynamic Fracture. *Physical Review Letters*, 74(25):5096–5099, 1995.
- [119] G.C. Sih. Strain energy factors applied to mixed mode crack problems. *International Journal of Fracture*, 10:305–321, 1974.
- [120] R. P. Singh, J. Lambros, A. Shukla, and A. J. Rosakis. Two optical techniques applied to the investigation of the mechanics of intersonic crack propagation along a bimaterial interface. *Proceedings of the Royal Society of London, A* 453:2649–2667, 1997.
- [121] R. P. Singh and A. Shukla. Intersonic crack propagation in bimaterial systems. *Journal of Applied Mechanics*, 63(4):919–924, 1996.
- [122] H.E. Stanley and N. Ostrowsky. *Random Fluctuations and Pattern Growth: Experiments and Models*. Kluwer Academic, Dordrecht, 1988.
- [123] Z. Suo and J.W. Hutchinson. Interface crack between two elastic layers. *International Journal of Fracture*, 43:1–18, 1990.
- [124] Y.-H. Taguchi. Dynamical Modelling of Fracture Propagation. *Material Science and Engineering*, 176:295–298, 1994.
- [125] C. Teodosiu. A dynamic theory of dislocations and its applications to the theory of the elastic-plastic continuum. In J. A. Simmons, editor, *Conf. Fundamental Aspects of Dislocation Theory*, volume 2, page 837, Washington, 1969. Natl. Bureau of Standards Special Publication.
- [126] M.E. Thurston and A.T. Zehnder. Nickel-alumina Interfacial Fracture Toughness: Experiments and Analysis of Residual Stress Effects. *International Journal of Fracture*, 76:221–241, 1996.

- [127] H. V. Tippur, S. Krishnaswamy, and A. J. Rosakis. Coherent gradient sensor for crack tip deformation measurements: Analysis and experimental results. *International Journal of Fracture*, 48:193–204, 1990.
- [128] H. V. Tippur, S. Krishnaswamy, and A. J. Rosakis. Optical mapping of crack tip deformations using the method of transmission and reflection coherent gradient sensing: a study of crack tip  $k$ -dominance. *International Journal of Fracture*, 52:91–117, 1991.
- [129] J. Tomblin, T. Lacy, S. Hooper, A. Vizzi, and S. Lee. *Review of Damage Tolerance for Composite Sandwich Airframe Structures*. U.S. Department of Transportation, Federal Aviation Administration NOTICE, Office of Aviation Research, Washington, D.C. 200591, 1999.
- [130] V. Tvergaard and J. W. Hutchinson. The influence of plasticity on mixed-mode interface toughness. *Journal of the Mechanics and Physics of Solids*, 41:1119–1135, 1993.
- [131] V. Tvergaard and J. W. Hutchinson. Effect of strain dependent cohesive zone model on predictions of crack growth resistance. *International Journal of Solids and Structures*, 33:3297–3308, 1996.
- [132] V. Tvergaard and J. W. Hutchinson. Effect of strain dependent cohesive zone model on predictions of interface crack growth. *Journal de Physique IV*, 6:165–172, 1996.
- [133] K. Willam. Simulation issues of distributed and localized failure computations. In J. Mazars and Z. P. Bazant, editors, *Cracking and Damage*, pages 363–378, New York, 1989. Elsevier Science.
- [134] M.L. Williams. The Stresses Around a Fault or Crack in Dissimilar Media. *Bulletin of the Seismological Society of America*, 49:199–204, 1959.
- [135] L. Xu and A.J. Rosakis. Real time experimental investigation of dynamic failure mode selection in sandwich structures. *Caltech Report*, 2000.
- [136] X. P. Xu and A. Needleman. Void nucleation by inclusion debonding in a crystal matrix. *Modelling and Simulation in Materials Science and Engineering*, 1:111–132, 1993.

- [137] X. P. Xu and A. Needleman. Numerical simulations of fast crack growth in brittle solids. *Journal of the Mechanics and Physics of Solids*, 42:1397–1434, 1994.
- [138] X. P. Xu and A. Needleman. Numerical simulations of dynamic interfacial crack growth allowing for crack growth away from the bond line. *International Journal of Fracture*, 74:253–275, 1995.
- [139] X. P. Xu and A. Needleman. Numerical simulations of dynamic crack growth along an interface. *International Journal of Fracture*, 74:289–324, 1996.
- [140] E. Yoffe. The Moving Griffith Crack. *Philosophical Magazine*, 42:739–750, 1951.
- [141] S.J. Zhou, P.S. Lomdahl, R. Thomson, and B.L. Holian. Dynamic Crack Processes via Molecular Dynamics. *Physical Review Letters*, 76(13):2318–2321, 1996.